COLLECTIVE QUANTUM BEHAVIOR OF ATOMIC ENSEMBLES IN HIGH-FINESSE OPTICAL CAVITIES

A DISSERTATION

SUBMITTED TO THE DEPARTMENT OF APPLIED PHYSICS

AND THE COMMITTEE ON GRADUATE STUDIES

OF STANFORD UNIVERSITY

IN PARTIAL FULFILLMENT OF THE REQUIREMENTS

FOR THE DEGREE OF

DOCTOR OF PHILOSOPHY

Geert Vrijsen

December 2011

This dissertation is online at: http://purl.stanford.edu/nb366rt7958

I certify that I have read this dissertation and that, in my opinion, it is fully adequate in scope and quality as a dissertation for the degree of Doctor of Philosophy.

Mark Kasevich, Primary Adviser

I certify that I have read this dissertation and that, in my opinion, it is fully adequate in scope and quality as a dissertation for the degree of Doctor of Philosophy.

Leo Hollberg

I certify that I have read this dissertation and that, in my opinion, it is fully adequate in scope and quality as a dissertation for the degree of Doctor of Philosophy.

Jelena Vuckovic

Approved for the Stanford University Committee on Graduate Studies.

Patricia J. Gumport, Vice Provost Graduate Education

This signature page was generated electronically upon submission of this dissertation in electronic format. An original signed hard copy of the signature page is on file in University Archives.

In memory of my grandparents, Eduard Aerts and Nathalie de Raeve

Abstract

Spin-squeezed states (SSS) are collective atomic states whose Heisenberg uncertainty properties have been altered, either by state transfer from squeezed light, or, as presented here, by a quantum non-demolition (QND) measurement of a light field after it has probed the atomic system. These states are of interest for their potentially large increases in measurement precision in atom-based experiments, and for the study of many-particle entanglement.

The body of work related to generating these novel states through measurement of a non-destructive probe (after interaction with the atomic system) can be split into two general groups: Those using atoms in free space, and those using optical cavities. This dissertation will focus on the approach using optical cavities, increasing the effective optical depth, and therefore the interaction strength between the atoms and the light.

The first experiment will describe a quantum nondemolition measurement to probe the collective pseudospin of an atomic ensemble in a high-finesse optical cavity. We analyze the backaction antisqueezing produced by the measurement process to show that our protocol could create conditional spin squeezing in the atomic ensemble. However, technical measurement noise and residual variations in atom-cavity coupling limit our ability to observe squeezing while preserving coherence.

In the second experiment we attempt to remove these main sources of noise by trapping the atoms in a far red-detuned optical lattice with twice the wavelength of the probe light. This wavelength configuration ensures that lattice antinodes, where the atoms are trapped, are always overlapped with probe antinodes, ensuring maximum coupling between the atoms and the probe field. The trapping also prevents atoms

from exploring the cavity mode, eliminating noise due to variations in atom-cavity coupling.

Finally, I will describe a third experiment (unrelated to spin squeezing) in which we experimentally realized a Raman laser in a high-finesse optical cavity. The large collective cooperativity of the atom-cavity system manifests in some interesting threshold behavior of the cavity output power, which we can describe using a simple model. Although not directly related to spin squeezing, a lasing system with the highly configurable gain medium presented here could have applications as a light source in precision measurement.

Acknowledgements

I have greatly enjoyed my graduate school experience, as I am sure is evidenced by my length of stay. Over the years I have made friends out of many a colleague, and have had the good fortune to learn a lot from them.

First and foremost, of course, is my advisor Mark Kasevich. Mark's never-ending enthusiasm and physical intuition had a serious impact on me as a junior graduate student in his group. Over the years I have come to respect the amount of time, effort, and thought he puts into taking care of his students. He takes almost as much pride in being an experimentalist as he does in not being a theorist, a feeling he instills into his students. His creativity and resourcefulness have saved me countless hours on many occasions, and his ability to rattle off noise figures for almost every piece of scientific equipment ever made still astounds me.

Over the years I have been lucky to learn from several post-docs on this experiment. In the first phases of the experiment Romain Long and Ari Tuchman oversaw my development as a junior grad student, and provided the necessary know-how for most of the initial assembly of the experiment. After their departure, Igor Teper safely helped me grow into my own as I took greater responsibilities in the lab. He was instrumental in the design and assembly of the second generation of the experiment, and his physical intuition is something I strive to equal. His encyclopedic knowledge of scientific and humorous publications has become the subject of lab folklore. Finally, Onur Hosten is the current post-doc on the experiment, and immediately made his presence felt by coming up with a simple model describing the Raman lasing experiment. I feel very comfortable leaving the experiment in his hands. All four of these post-docs, while very different in style, are incredibly gifted researchers who

made the learning curve manageable for me, and I am grateful to each of them.

There have also been a number of graduate students on this project. Julien Boudet, Aakash Sahai and Jiang Jiang were electrical engineering Master's students instrumental in creating the electronics which still control the experiment today. Julien in particular performed laboratory feats (which will remain unnamed) not replicated since his departure, and became one of the best friends I met in graduate school. Jongmin Lee was my partner in crime for the majority of grad school, after deciding to leave the dark side and switch from electrical engineering to join the applied physics department. He has had a hand in everything I did, and wish him the best in his future career. Nils Engelsen will take over the torch as senior grad student, and from the year I've worked with him I can safely say that he is more than equal to the task.

I owe a lot to the rest of the Kasevich group, past and present, for their help with any scientific obstacles presented to me over the years. This group includes (in no particular order, but feel free to assume it's a ranking) Jason Hogan, Seth Foreman, Alex Sugarbaker, Susannah Dickerson, Catherine Kealhofer, Gunnar Skulason, Hui-Chun Chien, Dave Johnson, Sheng-Wey Chow, Tim Kovachy, Peter Hommelhoff, Nick Cizek, Olaf Mandel, Xinan Wu, Ken Takase, Grant Biedermann, Mingchang Liu, Sean Roy, and Todd Gustavson. They will hopefully never again let a rabbit ski off the back of Squaw Valley.

It's the support staff who keep everything but the experiment running smoothly, and if helping grad students with paperwork were an Olympic discipline, Ping Feng would be the reigning champion. It's impossible for the Stanford bureaucracy to get the better of you with Ping on your side. She is helped on the applied physics department's end by Paula Perron and Claire Nicholas, who are both incredibly helpful and suitably tenacious in dealing with scientists, and are always willing to lend a helping hand.

There has also been an extensive group of friends who I have to thank for welcoming me to the USA as a wide-eyed foreign student during my senior of high school. Specifically, Stephen Kuchefski, Joni Marganski, Sam Berkes, Dustin Heiser, and Chris Herrmann took me under their wing and helped me adjust to American life. At

the University of Illinois I was lucky to have a great set of roommates and pseudo-roommates in Matt Rakher, Nick Farrey, Jason Komora, Steve Zoerb, Mark Murphey and Colin Winters, despite whom I still managed to graduate. Here at Stanford I was lucky enough to do endless problem sets or drink the occasional beer, simultaneously or not, with Praj Kulkarni, Chad Giacomozzi, Stephanie Majewski, Tommer Wizansky, Ann Erickson, Steve Sensarn, Matt Pyle, Ginel Hill, Matt Wheeler, Guillaume Chabot-Couture, Brian McFarland, Margie Teng, Hilary Schaffer, Emmalynne Hu, Mark Burkhardt, Eugene Motoyama, Jamie Mak, Jason Randel, Jen Trolio, and a number of others already mentioned. Kaushik Roy, my first and only roommate at Stanford, deserves a special mention as he and I were well on our way to a common-law marriage before he graduated, and I am very lucky to have had him as a friend from my earliest days here.

Of course, I would not be here without the constant support from my family. My parents, Marc and Reinhilde, have been an example to me in everything I did from pre-school through grad school. They kept their promise to pay for my schooling for much longer than they expected, a promise made to motivate a rebellious teenager who didn't feel like studying. I am incredibly grateful for the opportunities I've gotten thanks to them. I also need to thank my sister, Annelies, for being a good sport during childhood and a true friend as an adult. She, along with her husband Diedrik, is responsible for my goddaughter Nore and the incredible Mats. In addition to this, she constantly makes me look bad when it comes to remembering birthdays and anniversaries. My grandparents, Henri Vrijsen and Paula Clerix have always been supportive and I'm thankful that no matter how long I'm away, they are always excited to see me and find out what I've been up to.

Finally, during my stay at Stanford I was lucky enough to meet my main squeeze, Sara Gamble. She picks up the slack for me in most non-physics matters of life, and I am forever grateful for her patience, dedication, and acquisition of our lagomorphs Nacho Supreme and Con Queso. Thank you for everything, and especially for sharing your great family with me. I look forward to many fantastic years together!

Contents

List of Tables

List of Figures

Chapter 1

Introduction

Quantum metrology studies the possibility of harnessing quantum entanglement in order to increase measurement sensitivity beyond the shot-noise limit [1, 2]. The most precise atomic clocks are currently at the standard quantum limit (SQL), where the precision scales as $\sqrt{N}$, where N is the number of atoms making up the clock. The fundamental precision limit is, however, the Heisenberg limit which can offer a factor of $\sqrt{N}$ improvement over the SQL to a precision scaling with N.

It is possible to modify the collective state of an atomic ensemble by placing the atoms inside an optical cavity [3, 4]. While the use of an optical cavity is not necessary to modify the collective state of the atoms [5], placing the atoms inside a cavity accomplishes two things: (1) The optical depth of the sample is enhanced; and (2) The atoms scatter into the same cavity mode, destroying the "which way" information which would allow us to determine which atom scattered a given photon. A subsequent quantum non-demolition (QND) measurement of the light exiting the cavity can then provide information about the collective state of the atoms without revealing any information about a particular atom [6]. In particular, it is possible to measure the change in the cavity's resonance frequency due to the refractive index of near-resonant atoms to extract information about the clock states of an ensemble of atoms without knowing the state of any specific atom. This measurement has thus reduced ("squeezed") the uncertainty in the population difference between the clock states at the expense of an increased uncertainty in the relative phase between the

atoms. The reduced uncertainty of this squeezed state has the potential to provide a significant improvement in the precision of a clock measurement [2, 7].

Atomic spin-squeezed states have previously been produced by quantum-state transfer from squeezed light [8] or by entangling two-photon transitions [9, 10], and while there has been significant progress toward practical applications, including spectroscopy [11] and interferometry [12], substantial sensitivity improvements beyond proof-of-principle demonstrations can be achieved by borrowing techniques developed in cavity QED [3, 4, 6, 13]. Until recently, however, work in cavity QED has primarily focused on observing cavity effects at the single atom and single photon level [14, 15, 16], whereas quantum metrology requires large atomic ensembles. The application of these techniques to many-atom ensembles is a promising means toward the realization of novel experimental systems.

The application of QND measurements to generate interesting quantum states is not limited to atoms in cavities. A phase-shift measurement protocol has been used to entangle the collective spin states of two atomic ensembles [17], and a QND scheme has been used to measure the state of a superconducting charge qubit coupled to a microwave resonator and to characterize the resulting measurement back-action [18]. A QND measurement using Rydberg atoms to number-squeeze an intra-cavity photon state has also been demonstrated [19]. Recently, the heating effects of quantum-measurement back-action on an ultra-cold atomic gas have been studied [20].

The performance of many protocols in quantum information processing [21, 22, 23] that have been demonstrated in free-space atomic systems is limited by the optical depth of the atomic sample, which can be enhanced by placing atomic samples inside optical cavities, as in [24]. Furthermore, unlike proposals for cavity implementations of quantum computation [25, 26], metrology applications require relatively weak entanglement, and therefore are potentially less sensitive to decoherence effects [3]. Other applications which utilize the more robust collective effect of many atoms in the cavity mode include single photon generation [27] and generation of squeezed states of the optical field [28, 29].

On a slightly different note, ultrahigh-precision spectroscopy, metrology, and many quantum optics experiments stand to benefit substantially from the advance of gain

media that can be tuned for properties like gain bandwidth, index of refraction, or dispersion. Raman gain in atomic systems permits precise control over such properties through variations in the pumping mechanism. Recent experiments in heated atomic vapors, pumped by light at two optical frequencies, for instance, demonstrate anomalous dispersion [30]. Such a property could be integrated into a lasing system to increase sensitivity of lasing frequency to the laser cavity length, e.g., to enhance gravity wave detection sensitivity. As another example, Raman gain allows the tunability of the effective dipole moments of the gain medium atoms simply by tuning the pump power. This is an attractive property, which, for example, could be employed to simulate some of the novel aspects of the recently proposed (for their potential ultra-narrow linewidths) but technically challenging to realize high-finesse lasers that utilize transitions of alkaline-earth atoms with extremely small dipole moments [31]. Particular interest would be towards investigating the resulting phenomenon of steady-state superradiance [32].

The use of an atomic Raman gain medium for a laser was first demonstrated with a heated vapor cell [33], and has since been realized with cold atoms [34, 35]. These experiments show narrow gain bandwidth properties, but operate with low-finesse optical cavities, in a regime where the single-atom cooperativity parameter $C \ll 1$. This parameter is a measure of the effect atoms have on the cavity field, with $C > 1$ indicating a substantial influence even from single atoms.

In Chapter 2 I will lay out the basic experimental setup used for the experiments descibed in Chapters 3 and 4. Chapter 3 details use of atom-cavity interactions to generate normal-mode splitting of the dressed atom-cavity states. Chapter 4 discusses our characterization of the measurement back-action on the atomic states, manifested by an increase in the uncertainty of the population difference between the two clock states. After this experiment is became clear we needed a significant upgrade of our experimental setup, which is presented in detail in Chapter 5. That chapter contains a description of the assembly and characterization of the dual wavelength cavity. While in the progress of debugging the apparatus we became aware of low levels of light being emitted from our cavity, with only a continuously loading magneto-optical trap (MOT) present. Chapter 6 details the fortuitous discovery of our Raman laser

which temporarily sidetracked our quest for spin-squeezed atomic states. Chapter 7 contains a summary and description of future plans for this apparatus.

Chapter 2

Experimental Details

2.1   Overview

Experiments with cold atoms are comprised of a number of components, including a vacuum chamber with an atom source, lasers to cool and trap the atoms, a number of current carrying coils for generating magnetic fields, and a detection mechanism, most often an imaging system. The continued development of technology in cold-atom physics, especially since the first realization of optical molasses [36], has resulted in a number of approaches to these building blocks of an experiment. In this chapter I will discuss the different subsystems we employ in our experiment, and I will describe why we chose these particular implementations over other alternatives.

2.2   Magneto-optical Trap Laser System

The starting point for most atomic physics experiments is a frequency-stabilized laser system to cool and trap the atoms. The laser wavelength needs to match the resonance wavelength of the atomic species used in the experiment. In our case ^{87}Rb has a resonant wavelength $\lambda_0 = 780.241$ nm between the $5S_{1/2}$ ground state and the $5P_{3/2}$ excited state, also known as the D_2 transition.

Our laser system is very compact and robust, as shown in Fig. 2.1 which starts out with two 780 m, distributed feedback (DFB) laser diodes, one for generating
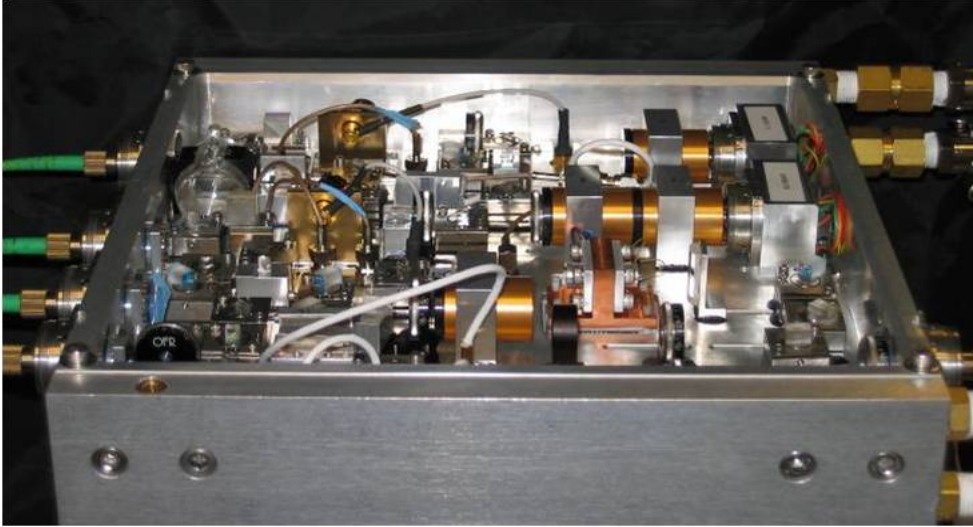
Figure 2.1: Picture of the frame which houses the cooling and repump lasers. Pictured are two laser diodes, each of which is locked to the appropriate ^{87}Rb crossover transition by means of a vapor cell. The stabilized light is frequency shifted by means of an acousto-optical modulator, and subsequently fiber-coupled. The cooling light is additionally amplified by a tapered amplifier.

the cooling light, and one for the repump light. Both of these diodes are frequency stabilized to a ^{87}Rb transition via a vapor cell. A small fraction of the diode output is picked off with a polarizing beam splitter (PBS), and sent through a vapor cell. We use frequency modulation (FM) spectroscopy [37] to stabilize the lasers, which was chosen for its low requirements of optical components, suitable for fitting the assembly into a small space to maintain a compact laser system.

While ^{87}Rb has a natural linewidth $\Gamma = 6.067$ MHz, the Doppler effect due to the atoms' thermal motion broadens this to ~ 500 MHz at room temperature, effectively blending the different spectral lines together. Many Doppler-free spectroscopic techniques have been developed which are able to resolve the narrow Doppler-free spectral lines in the broad Doppler profile. We employ one such technique, FM spectroscopy, to stabilize the laser frequency to better than the natural linewidth.

In FM spectroscopy the laser frequency is weakly modulated. A beam splitter divides the power between a strong pump and a weak probe, and are arranged to counterpropagate through a ^{87}Rb vapor cell, as shown in Fig. 2.2. The pump interacts

with atoms which have a velocity $v = (\omega - \omega_0)/k$ (where ω_0 is the atomic resonance frequency for stationary atoms), and excites many of them to the excited state. When the laser frequency is far from resonance, i.e. $|\omega - \omega_0| \gg \Gamma$, the pump and probe beams interact with atoms in a different velocity class, and the probe is unaffected by the pumps presence. However, when $\omega \simeq \omega_0$ the pump depletes the velocity class near $v \simeq 0$, which the probe is also sensitive to, resulting in an increase in transmitted probe intensity. As the pump beam only excites those velocity classes for which $|\omega - \omega_0| \lesssim \Gamma$, the resulting profile will show sub-Doppler features with frequency width comparable to the natural linewidth. The frequency modulation applied to the laser diode now causes the light to sweep a region with strong frequency dependent absorption of the probe beam, effectively turning frequency modulation into amplitude modulation. The detector records this amplitude modulation, which can be demodulated to result in an error signal. This error signal is appropriately amplified and filtered, and fed back to the laser diode to stabilize the frequency.

The cooling and repump beam are each appropriately frequency shifted by an acousto-optical modulator (AOM), and are subsequently fiber coupled. The results is a laser system which is approximately 30 cm $\times$ 30 cm $\times$ 5 cm and routinely stays stabilized to Rb for weeks. Drifts in fiber output powers are approximately 1% per month.

2.3 Vacuum Chamber and Magneto-optical Trap

The experiments described in this Dissertation make use of two vacuum chamber and cavity assemblies, the second being an upgraded version of the first, taking into account lessons learned during the first experiments. The chamber and cavity described in this section is the first generation hemispherical cavity used in Chapters 3 and 4. Due to the added complexity of the second generation dual wavelength confocal cavity, it is described in detail in Chapter 5.

Our vacuum chamber is constructed entirely of Zerodur, a glass with a very low coefficient of thermal expansion of $< 5 \times 10^{-8}$ K^{-1}. The low thermal expansion is to minimize thermal drifts of our optical cavity length. Zerodur is also a high quality
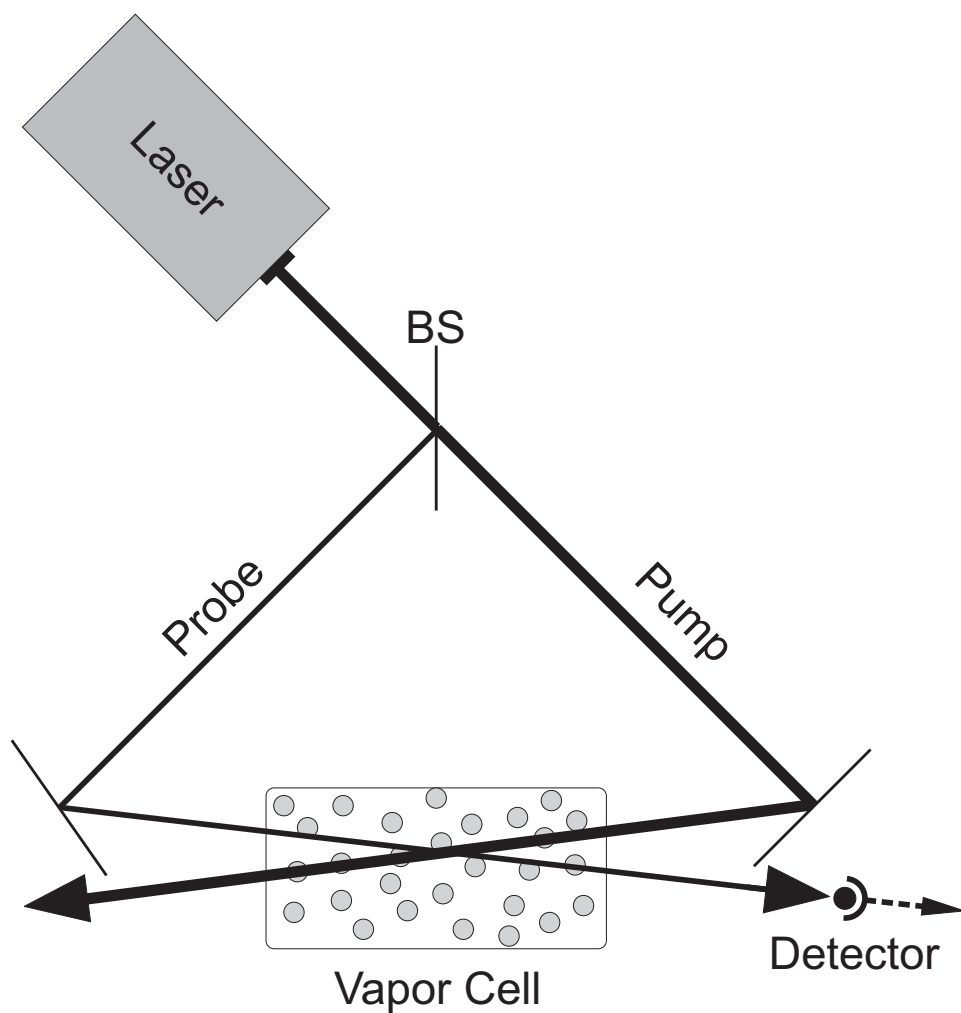
Figure 2.2: Schematic of a typical saturation absorption spectroscopy setup, with a beamsplitter (BS) divides the power between a strong pump and a weak probe which counterpropagate through a vapor cell. Although for clarity the beams are not perfectly counterpropagating in this schematic, they are in the actual experiment.
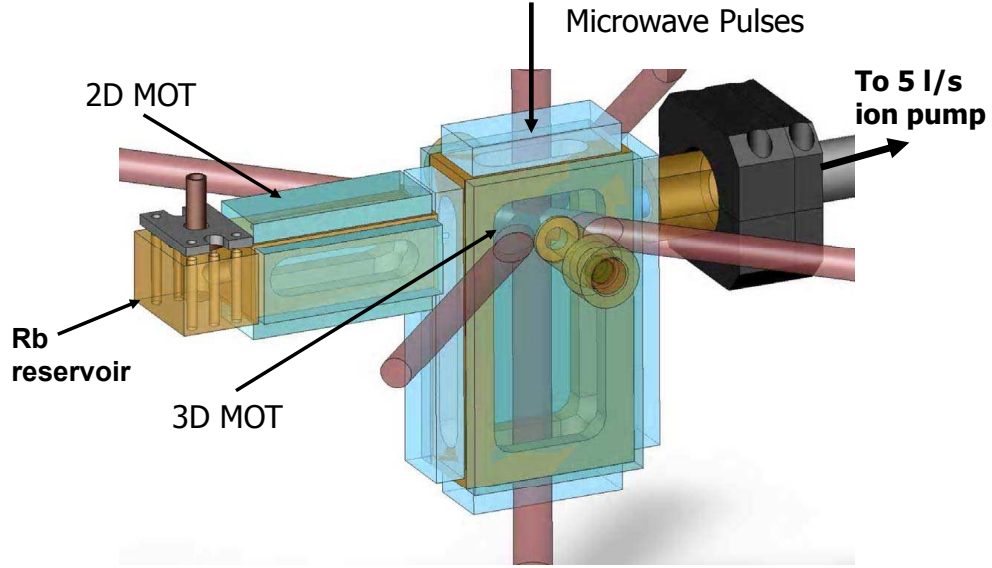
Figure 2.3: The Zerodur vacuum chamber consisting of the Rb reservoir, 2D MOT chamber, 3D MOT chamber with cavity tubes, and glass-to-metal indium seal leading to the ion pump. Red arrows are the 3D MOT beams intersecting at the center of the cavity. Microwaves can be sent to the atoms from above the chamber. Magnetic field coils are not shown, but are located at each surface of the 2D MOT, and wrap around the 3D MOT chamber, just above and below the cavity tubes.

glass which can be polished to a high quality surface, has excellent internal quality, $> 95\%/\text{cm}$ transmission for wavelengths between 700 nm and 1600 nm, and bonds well to most epoxies. A three-dimensional rendering of the vacuum chamber is shown in Fig. 2.3.

Two chambers make up our vacuum assembly, as shown in Fig. 2.4. The 4 cm by 4 cm by 8 cm two-dimensional magneto-optical trap (2D MOT) chamber is connected to the 4 cm by 12 cm by 8 cm three-dimensional magneto-optical trap (3D MOT) chamber by a 2 mm pinhole. We capture atoms in a cigar shaped cloud in the 2D MOT chamber, and the atoms' thermal motion along the chamber axis propels them through the pinhole into the 3D MOT chamber, where they are trapped and cooled by 0.75 cm beam waist 3D MOT beams. An indium seal clamps a stainless steel tube attached to a 5 L/s noble ion pump to a glass disk at the end of the 3D MOT chamber, as shown in Fig. 2.3. The ion pump, combined with a mean free path between atom

collisions of ~ 100 km in ultra-high vacuum (UHV) preventing atoms from efficiently passing through the pinhole, results in a factor 100 lower ^{87}Rb vapor pressure in the 3D MOT chamber compared to the 2D MOT chamber. This allows for fast loading of the 3D MOT by the 2D MOT, while maintaining long lifetimes in the 3D MOT chamber.

The cavity is assembled by attaching two Zerodur tubes on opposite sides of the 3D MOT chamber using Epotek 353ND epoxy. The planar mirror is first mounted on a piezo-electric transducer (PZT) which is in turn attached to a Zerodur end cap. A 10 cm radius of curvature mirror is attached directly to another end cap. Each of the end caps is inserted into a Zerodur tube using a kinematic mirror mount mounted on a three stage micrometer. The micrometers allow for adjustment of the cavity length and mirror location, while the kinematic mount allows for mirror angle adjustment. Once the mirrors are aligned, the end caps are epoxied to the Zerodur tubes using Epotek 302-3M epoxy. This epoxy puts very little strain on the tubes as it cures, preventing cracking of the Zerodur. A major disadvantage is the low (≈ 70 °C glass transition temperature, limiting the maximum bake temperature.

The vacuum chamber was baked at a temperature of 70 °C for 48 hours while pumped by a Pfeiffer turbo pump. The bake temperature was limited by the indium used in the glass-to-metal seals, and the low glass transition temperature epoxy used to attach the Zerodur end caps.

A thin-walled stainless steel tube containing a 0.5 g vial of ^{87}Rb, attached to the main chamber via a copper pinch-off tube is used to transfer the Rb to the main vacuum chamber after the bake. The copper tube is attached to a Zerodur reservoir at the end of the 2D MOT chamber with an indium seal. The vial was cracked while under vacuum by pinching the stainless steel tube, and heated to 50 °C while the reservoir was cooled in order to have the ^{87}Rb collect there. After the ^{87}Rb was completely transferred we pinched the copper tube shut to detach the stainless steel tube while maintaining UHV.

After the bake, the chamber is continuously pumped by the ion pump running at 2 kV, the path to the turbo pump is valved off, and the turbo pump is disconnected. The vacuum chamber is only pumped by the ion pump, and the resulting pressure is $<$
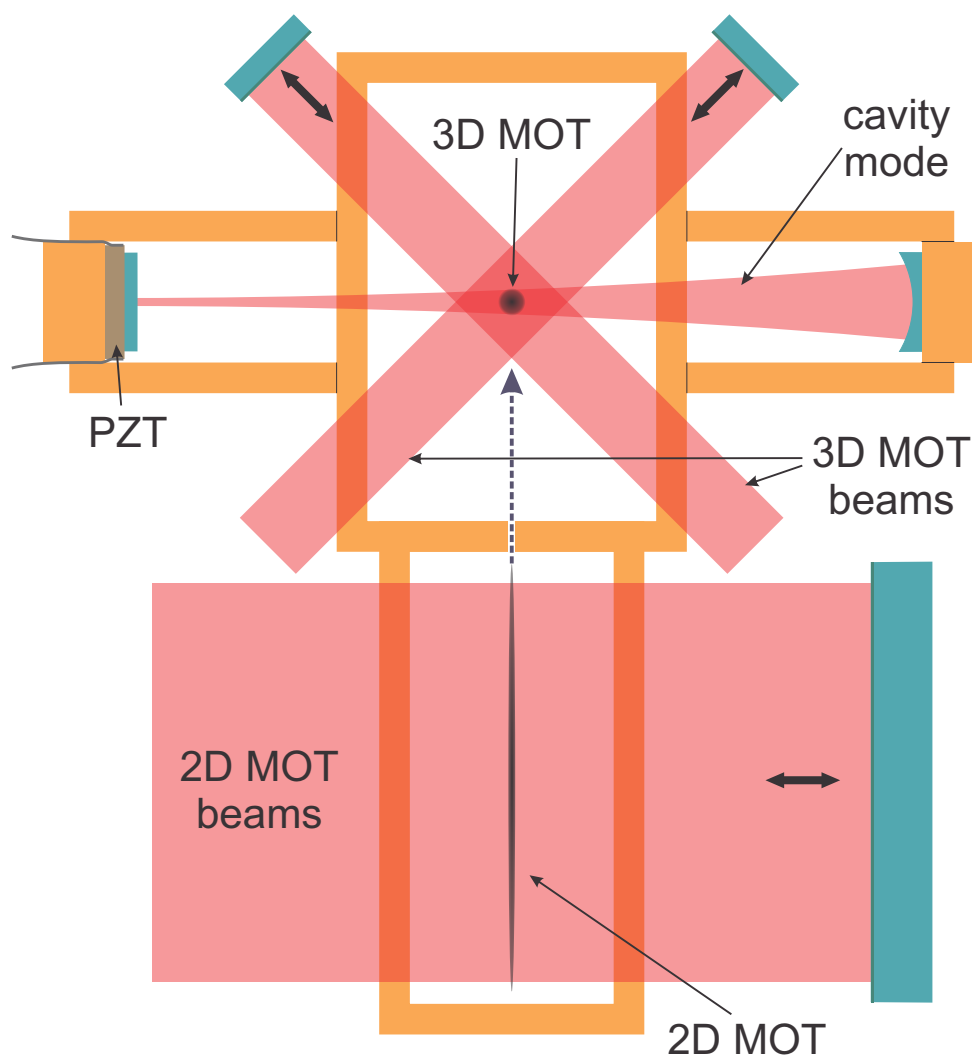
Figure 2.4: Top view schematic of the vacuum chamber. A 2D MOT launches atoms through a pinhole into the 3D MOT chamber (dotted arrow), where they are collected at the center of the cavity mode. All MOT beams are circularly polarized appropriately for the optical trap. Each retro-reflection mirror has a quarter-wave plate attached to its reflection surface to cause a double-pass 90° polarization rotation. A PZT allows for translation of the planar mirror. Double arrows indicate retro-reflection of the laser beams. Magnetic field coils are not shown.

10^{-8} mbar. The relatively high pressure is due to the very limited bake temperatures possible due to the indium seals and the low glass temperature epoxy.

Optical fibers from the stabilized laser system described in Section 2.2 transport laser light to an optomechanical assembly which houses the vacuum chamber, shown in Fig. 2.5. In conjunction with magnetic field coils, the light is used to trap the atoms and cool them to temperatures of a few tens of μK. The optomechanical assembly is about 0.03 m^3 in volume and could be packaged compactly together with the MOT laser source.

A diagram showing the ^{87}Rb energy levels and relevant light frequencies are shown in Fig. 2.6. Cooling light excites atoms from the $F = 2$ hyperfine ground state to the $F' = 3$ excited state, from which, due to the $\Delta F = \pm 1, 0$ selection rule, the atom can only decay back down to the $F = 2$ ground state. This forms a closed cycling transition. There is a small probability each cycle that the atom is excited to the $F' = 2$ excited level, from which the atom can decay down to $F = 1$. Without repump light, all the atoms would eventually end up in this state. The repump light resonantly excites the atoms from the $F = 2$ to $F' = 2$ state, from which they can decay back to $F = 2$ to resume the cycling transition. This repumping process takes on average only one or two photons, and therefore the atoms spend the majority of their time in the cycling transition.

The cooling and repump light is circularly polarized, spatially overlapped, and split into three beams. The three beams are aligned along three mutually perpendicular directions, intersecting at the center of the optical cavity. Each beam is retro-reflected by a mirror with a $\lambda/4$ wave plate, ensuring the same circular polarization of the reflected beam relative to its propagation direction. The required magnetic field are generated by 63-turn wound copper wire coils mounted just above and below the optical cavity tubes, on the outside of the vacuum chamber. The 6 A current runs through the coils in opposite directions, resulting in an anti-Helmholtz configuration with a magnetic field gradient of about 7 G/cm at the magnetic field zero. Atoms are trapped at the magnetic field zero, which is designed to be in the center of the optical cavity at the same place where the MOT beams intersect. The cooling light is slightly ($\sim 1.5\Gamma$) red detuned from the $F = 2 \rightarrow F' = 3$ transition.
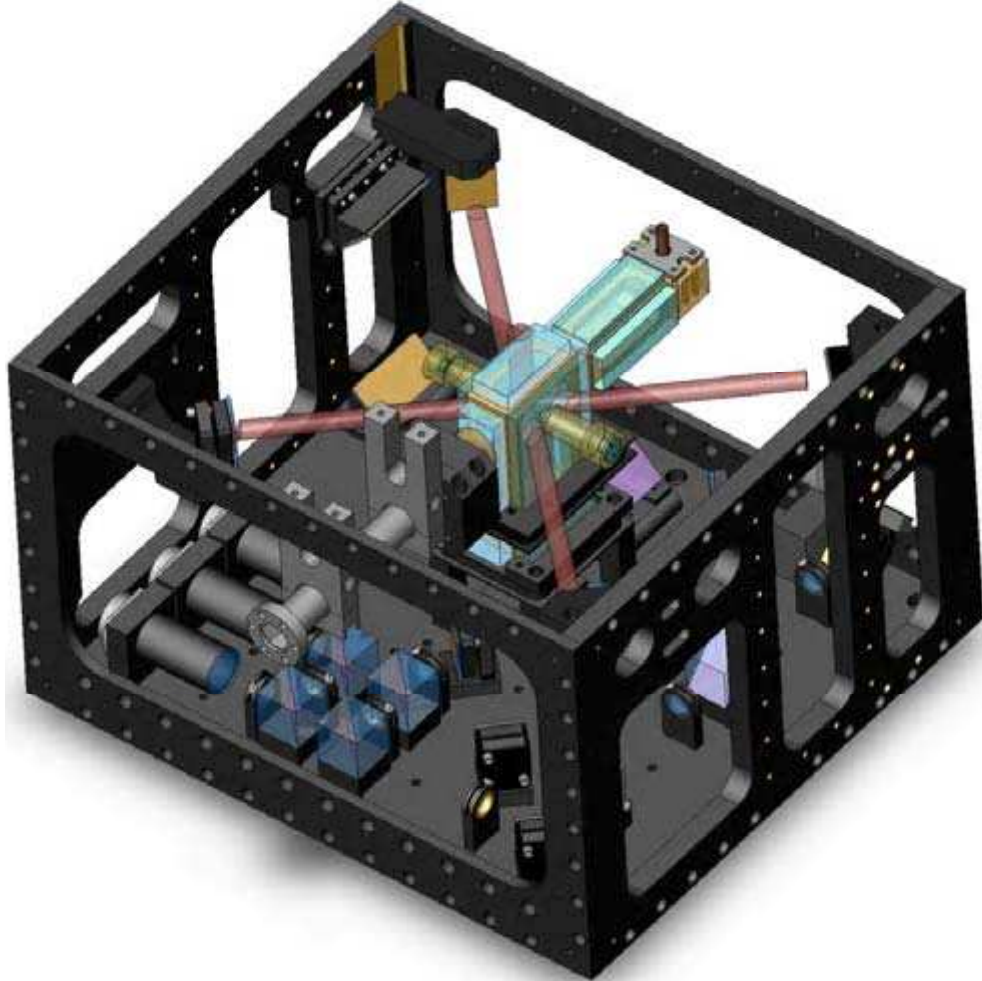
Figure 2.5: The optomechanical assembly with the Zerodur vacuum chamber mounted inside. A third set of MOT beams propagating vertically up and down the vacuum chamber are not shown. The top plate of the assembly is not shown, for clarity. This plate also contains a microwave horn which is used for state manipulation of the atoms. The approximate dimensions of the assembly are 40 cm by 40 cm by 30 cm.
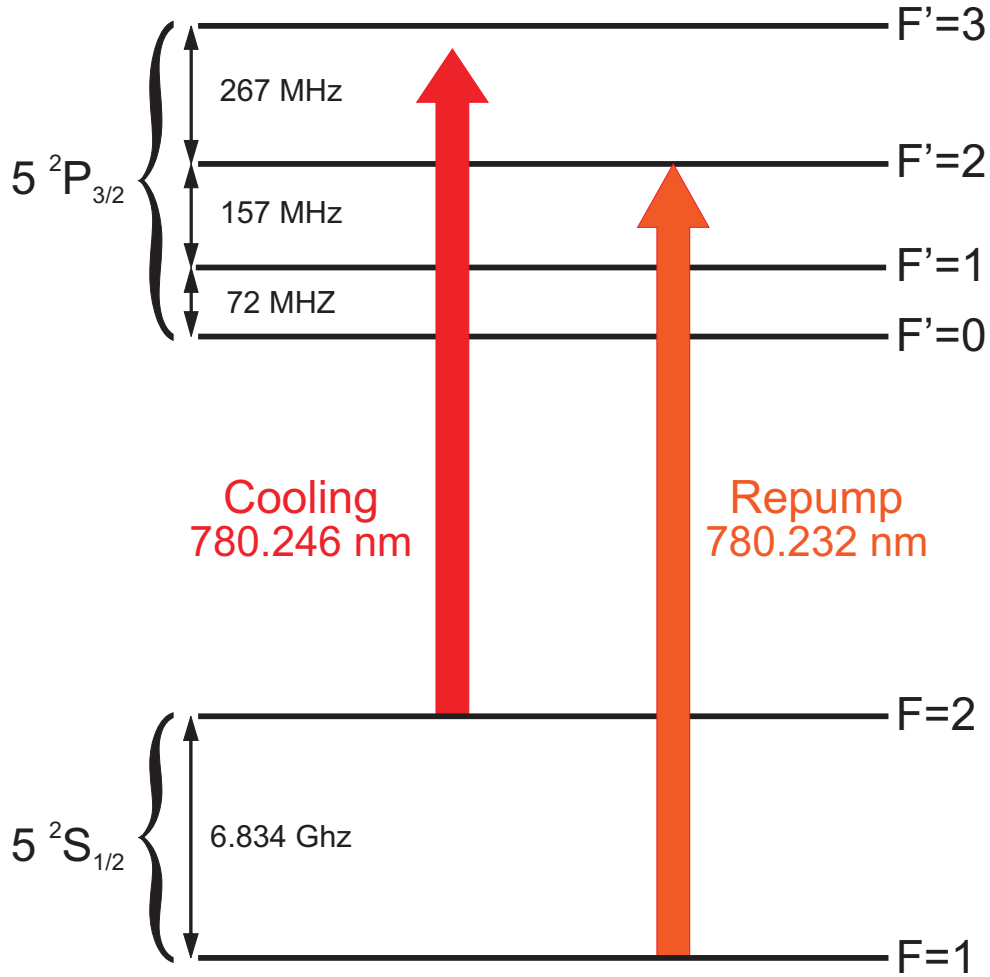
Figure 2.6: ^{87}Rb D$_2$ transition hyperfine structure, with the cooling and repump light shown in red and orange, resp. Note that the splitting of the ground state is significantly larger than the splitting between any of the excited states, making the schematic not to scale.

Using this method, we are able to cool the atoms to $\sim 15\mu$K.

2.4 Optical Cavities

Two cavities were used to carry out the experiments described in this dissertation, the second being an upgraded version of the first. This cavity upgrade was motivated by limitations uncovered while conducting the first experiments, described in Chapters 3 and 4. The main advantage of the second cavity over the first is a high cavity finesse at 1560 nm in addition to 780 nm, allowing for dipole trapping of the atoms using the far-detuned 1560 nm light. The high-reflectivity mirror coatings for both cavities are commercially available from Research Electro-Optics.

2.4.1 Explanation of Terminology

The quality of a mirror is often described in terms of its reflectivity R, which for a good coating can be within a few parts per million (ppm) of unity ($R = 1$ being a perfect reflector). When assembled into a cavity configuration with multiple mirrors, however, a more widely used parameter is the cavity finesse, defined as $F = \pi\sqrt{R}/\left(1 - R\right) \approx \pi/\left(1 - R\right)$ where the approximation is good for R close to 1. A photon entering the cavity will, on average, make F/π round-trips before leaving the cavity, which also means that the optical absorption depth of an atomic sample placed inside the cavity increases by a factor $2F/\pi$.

In cavity quantum electrodynamics (cavity QED) the most useful system parameters are expressed as frequencies, or ratios thereof. The most important ones are schematically represented in Fig. 2.7. Fabry-Pérot type cavities have resonances at regularly spaced intervals, as shown in Fig. 2.7(b). Physically these resonances occur when an integer number of half-wavelengths fit inside the cavity, ensuring that the electric field is zero at the mirrors, or $\lambda_{\mathrm{n}} = 2L/n$. From $c = \lambda f$ we can see that the resonance frequencies of a cavity are $\nu_{\mathrm{n}} = nc/2L$, and it is clear that the spacing between frequencies is constant. This frequency spacing is called the free spectral range $\nu_{\mathrm{fsr}} = c/2L$, and it corresponds to the inverse of the round-trip time of a photon in
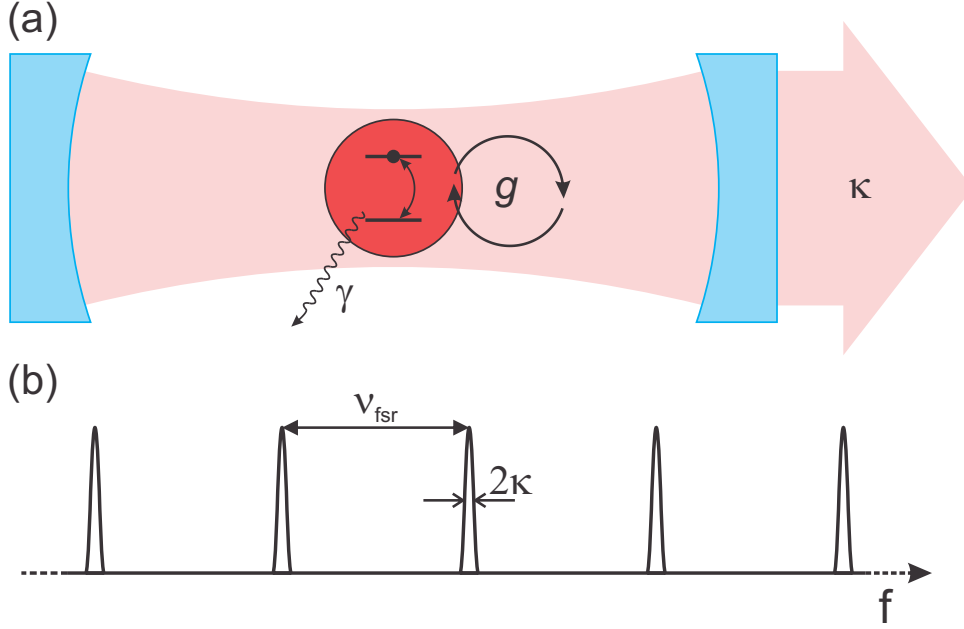
Figure 2.7: Schematic of important cavity quantum electrodynamics parameters. (a) A typical optical cavity configuration, with input beam intra-cavity atoms interacting with the light in the cavity mode with a Rabi frequency g, light leaking out of the cavity at a rate κ, and the atoms spontaneously emit at a rate γ. (b) Frequency spectrum of an optical cavity. The cavity allows a regularly spaced set of frequencies to resonate, each of which has a linewidth of 2κ. The resonances are separated by the free spectral range ν_{fsr} which is only proportional to the cavity length. The ratio of the two gives the Finesse, a measure of the number of round-trips a photon makes inside the cavity before exiting through the output mirror.

the cavity. Changing the optical frequency entering the cavity by one free spectral range is therefore equivalent to changing the number of half-wavelengths in the cavity by one.

It is often useful to talk about the cavity decay rate, or the rate at which photons leak out of the cavity. This is related to the finesse and the cavity length L. Photons decay at a rate of $2\left(1-R\right)$ per round trip, or $2\kappa = 2\left(1-R\right)c/2L = \pi c/FL$ where κ is the decay rate or, equivalently, the half-width at half-maximum (HWHM) cavity linewidth given in rad/s. The lifetime of a photon is then $\tau = 1/2\kappa$. Note that the cavity finesse can be expressed as the ratio of the free spectral range and the full cavity linewidth given in Hz $(2\kappa/2\pi)$.

The maximal coupling strength between atoms and a particular mode is given by the single-photon Rabi frequency g_0, given by

$$g_0 = \frac{\mu}{\hbar} \sqrt{\frac{\hbar \omega}{2 \epsilon_0 V_{\text{mode}}}} \tag{2.1}$$

where μ is the dipole matrix element of the intended transition, ω is the angular frequency of the electric field, ϵ_0 is the permittivity of free space. The cavity mode volume V_{mode} is defined as:

$$V_{\text{mode}} = \frac{\iiint \left| \vec{E}(\vec{r}) \right|^2 \, \mathrm{d}^3 \vec{r}}{\max \left(\left| \vec{E}(\vec{r}) \right|^2 \right)} \tag{2.2}$$

Note that g_0 is the maximal atom-cavity coupling, realized only if the atom is located in an antinode at the location of the narrowest electric field beam waist. For a hemispherical cavity, however, the narrowest beam waist is located at the planar mirror, and so the maximal atom-cavity coupling for atoms located equidistant from the two mirrors, as is the case for this apparatus, is reduced significantly. The advantage of this configuration is that the large beam waist at the atom position gives a more uniform electric field as the atoms move off-axis.

2.4.2   Single Wavelength Hemispherical Cavity

Our first generation optical cavity was constructed in a near-hemispherical configuration, with one planar mirror and one curved mirror with radius of curvature $R_{\text{C}} = 0.1 \, \text{m}$. The dielectric mirror coating has a reflectivity $R > 99.998\%$, and losses (scattering + absorption) < 5 ppm.

We chose a hemispherical cavity for its potential large beam waist at the center of the cavity, where the atoms are located. This large beam waist allows for a uniform atom-cavity coupling as atoms move off-axis. The $1/e$ electric field beam waist for a

hemispherical cavity TEM_{00} is given by:

$$w(z) = \sqrt{\frac{\lambda}{\pi} \frac{(R_\text{C} - L)\,L + z^2}{\sqrt{(R_\text{C} - L)\,L}}} \equiv w_0 \sqrt{1 + \left(z/z_\text{R}\right)^2} \qquad (2.3)$$

where $0 \leq z \leq L$ is the distance from the planar mirror, $w_0 = \sqrt{\frac{\lambda}{\pi}\sqrt{(R_\text{C} - L)\,L}}$ is the minimum beam waist, and $z_\text{R} = \sqrt{(R_\text{C} - L)\,L}$ is the Rayleigh range. Hemispherical cavities are only stable when the cavity length $L < R_\text{C}$ because $w(L) \to \infty$ as $L \to R_\text{C}$. As L is decreased below R_C, this beam waist decreases and the cavity becomes stable. While Eq. 2.3 suggests an arbitrarily large beam waist is possible, in reality this is limited by the curved mirror diameter and an increase in coating defects as a larger surface area of the curved mirror is covered by the cavity mode.

The free spectral range was measured to be $\nu_\text{fsr} = 1.505$ GHz, corresponding to a mirror separation of $L = c/2\nu_\text{fsr} = 9.957$ cm, $\sim 430\,\mu$m shorter than perfectly hemispherical. The cavity mode has a beam waist of $w_0 = w(0) = 40\,\mu$m at the planar mirror, corresponding to a beam waist of $w_c = w(L/2) = 315\,\mu$m at the center of the cavity, where the atoms are loaded. This leads to an atom-cavity coupling constant $g_c = 2\pi \times 53$ kHz for the $|F = 2, m_F = 2\rangle \to |F' = 3, m_{F'} = 3\rangle$ transition for atoms located on axis at a field antinode in the center of the cavity. The cavity ring down time $\tau = 21.7\,\mu$s was determined by using an AOM switch to shut off the driving beam, and measuring the $1/e$ decay time of the cavity output. This corresponds to a half-width-half-max cavity linewidth $\kappa = 2\pi \times 3.67$ kHz, or a finesse $F = 205,000$. Fig. 2.8 shows the measured cavity finesse and beam waist as functions of cavity length, and clearly shows the trade-off between the two.

The strong dependence of the beam waist on cavity length necessitated the use of "end-caps", small Zerodur cylinders which fit inside the cavity tubes in order to vary the cavity length. Once the desired length is obtained, the gap between the end-cap and the inner wall of the cavity tubes is filled with Epotek 302-3M epoxy, which puts very little stress on the glass as it cures. The downside of this epoxy is its low 60°C glass temperature, which greatly reduces the maximum bake-out temperature near the mirrors to ~ 50°C and limiting the resulting final pressure of the system to
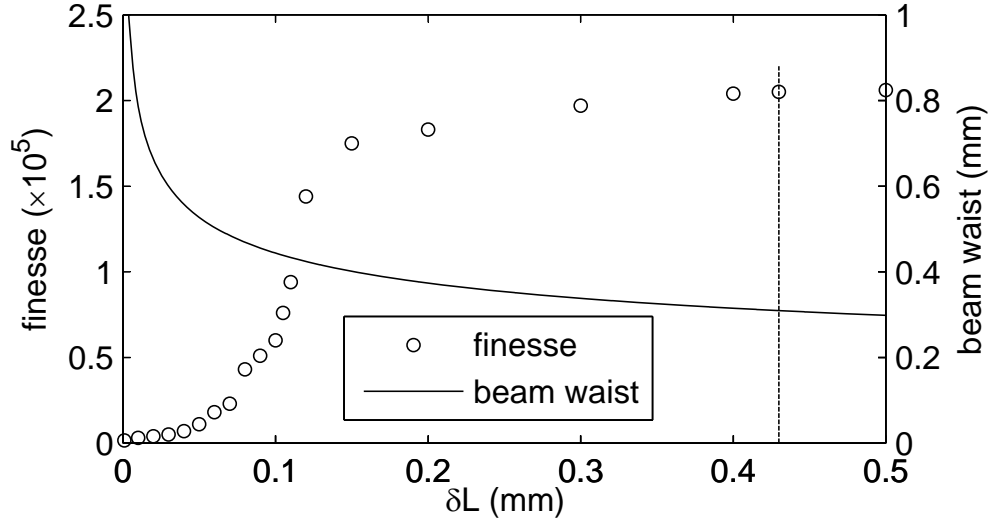
Figure 2.8: Finesse (circles) and beam waist (solid line, equidistant from the cavity mirrors) of the hemispherical cavity TEM$_{00}$ mode. $\delta L = R_{\mathrm{C}} - L$, with $\delta L = 0$ corresponding to the perfectly hemispherical configuration. Modes with large beam waists are more sensitive to imperfections in the mirror coatings and losses due to the finite mirror radius, which decrease the finesse. The vertical line signifies where we operate, with $\delta L = 430\ \mu$m, finesse $= 205,000$, and beam waist $= 310\ \mu$m. $R_{\mathrm{C}} = 100$ mm, the mirror radius is ~ 3.5 mm. The beam waist at the curved mirror is approximately double the plotted beam waist, and is significantly smaller than the mirror radius (630 mum $\ll 3.5$ mm) at our operating point.

parameter	symbol	value	units
wavelength	λ	780	nm
curved mirror radius	R_{c}	10	cm
length	L	9.957	cm
free spectral range	ν_{fsr}	1.505	GHz
beam waist at atoms	w_{c}	315	μm
atom-cavity coupling at atoms	$g_{\mathrm{c}}/2\pi$	53	kHz
ringdown time	τ	21.7	μs
decay rate (HWHM)	$\kappa/2\pi$	3.67	kHz
Finesse	F	205,000	
single-atom cooperativity at atoms	η	0.13	

Table 2.1: Hemispherical cavity parameters.

$\sim 10^{-8}$ mbar.

The single-atom cooperativity $\eta = g_{\mathrm{c}}^2/\kappa\Gamma = 0.13$, where $\Gamma = 2\pi \times 6.067$ MHz is the ^{87}Rb natural linewidth. Mirror losses (scatter + absorption) were characterized to be < 3 ppm by measuring single mirror transmission, and comparing to the reflectivity R inferred from the finesse $F = \pi/(1 - R)$. The most important cavity parameters are tabulated in Table 2.1.

2.5 Laser Stabilization

The narrow linewidth of the optical cavity requires a very well-stabilized laser system to be able to efficiently couple light into the cavity and probe the atoms. We stabilize the frequency of the laser to the cavity using a two-step stabilization scheme shown in Fig. 2.9. We start by stabilizing the output of a 780 nm New Focus Vortex extended cavity diode laser (ECDL) to a non-evacuated "scrubbing" cavity by using the error signal generated using a Pound-Drever-Hall [38, 39, 40, 41] technique.

The unstabilized Vortex ECDL output has a linewidth of ~ 300 kHz, while the scrubbing cavity linewidth is ~ 4 kHz at a cavity length of ~ 10.2 cm. This frequency disparity requires a high bandwidth servo in order to narrow the linewidth of the ECDL enough to allow a significant fraction of the incident beam to be resonant
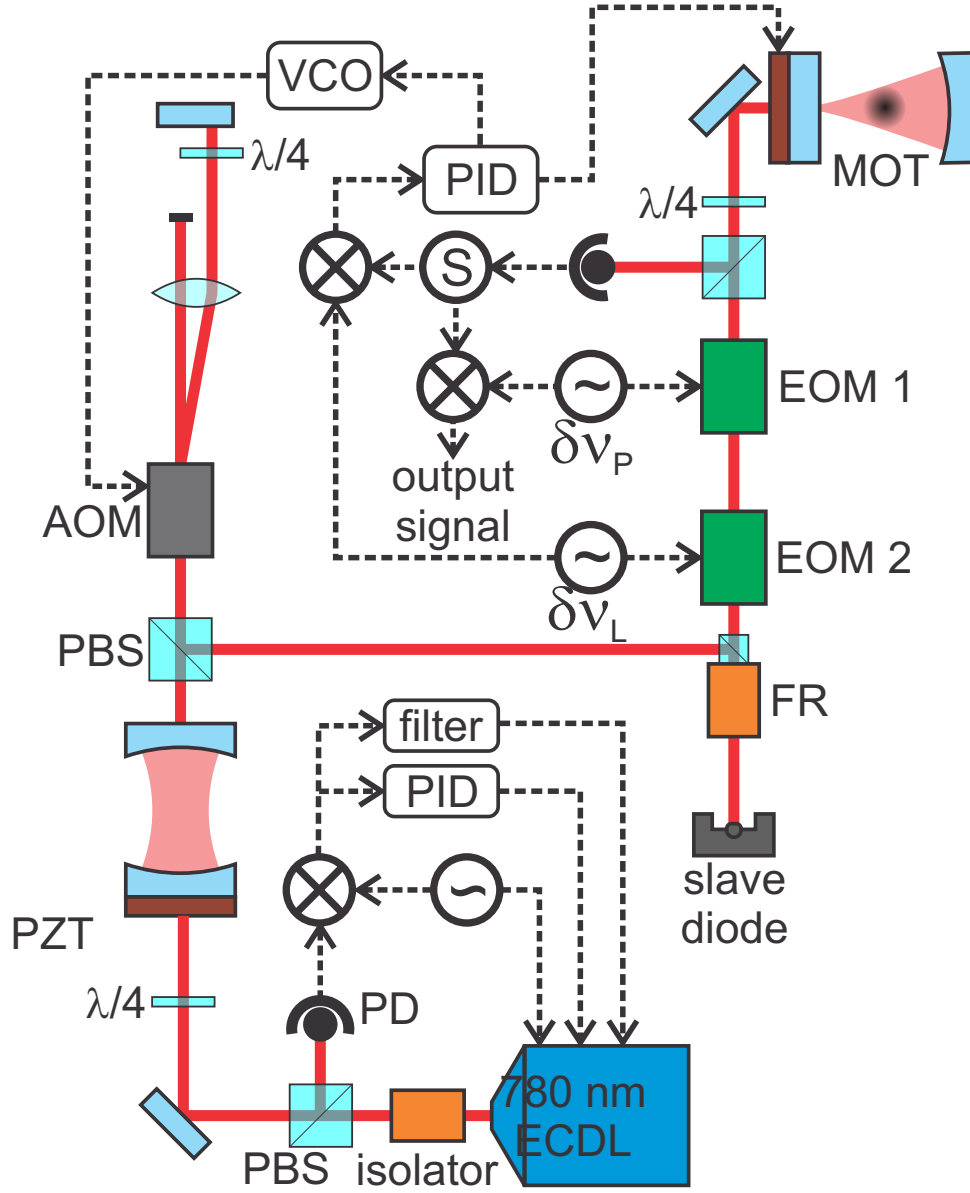
Figure 2.9: Optical and electronics path of the experiment. See text for explanation. $\delta\nu_L = 100$ MHz is the lock modulation frequency. $\delta\nu_P = 9.1$ GHz is the probe modulation frequency. ECDL = Extended Cavity Diode Laser, PBS = Polarizing Beam Splitter, AOM = Acousto-Optic Modulator, VCO = Voltage Controlled Oscillator, PID = Proportional-Integral-Differential gain controller, EOM = Electro-Optic Modulator, FR = Faraday Rotator, $\lambda/4$ = quarter-wave plate, $\lambda/2$ = half-wave plate, MOT = Magneto-Optical Trap.

with the cavity. The light transmitted through the scrubbing cavity is spectrally narrow, and we inject this light (via a double-passed AOM) into a slave laser diode to eliminate residual amplitude noise left after the scrubbing cavity, as the lock tends to convert frequency fluctuation at the cavity input into amplitude fluctuations at the output. The slave diode, running in saturation, will emit a constant output at the injected light's frequency, and be insensitive to these amplitude fluctuations.

The slave diode output is modulated by an EOM, generating a $\delta\nu_{\mathrm{L}} = 100$ MHz locking sideband and a $\delta\nu_{\mathrm{p}} = 9.1$ GHz probe sideband. The light reflected from the cavity is detected by a photodiode, and the resulting electronic signal is split into two paths, each of which is demodulated by either the locking or probe modulation frequencies. The path demodulated by the probe frequency is the dispersive output signal which is used to determine the changes in the cavity resonance frequency. The other path, after demodulation by the lock modulation frequency, is turned into an output signal-dependent frequency shift with a voltage controlled oscillator (VCO) and fed back to a double-passed AOM. The improvement in linewidth at different points in the optical path, as measured by a self-heterodyne beat note using a 3 km long optical fiber, is illustrated in Fig. 2.10.

The center of the dispersive output signal, resulting from demodulating the probe frequency, follows the cavity resonance frequency. This frequency shift $\delta\nu = Ng^2/\Delta$ where N is the atom number, g is the effective atom-cavity coupling frequency, and Δ is the detuning of the light from the atomic resonance. A plot showing the shift per atom $\delta\nu/N$ is shown in Fig. 2.11. The inset shows a typical location of the dispersive signal for a cavity both with and without atoms loaded.
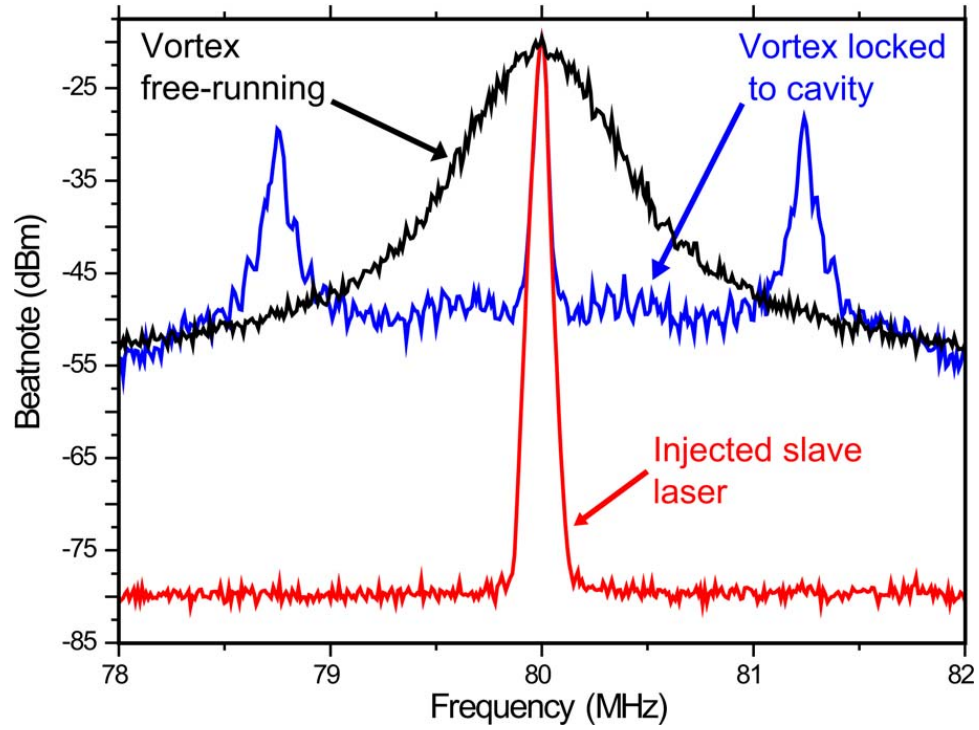
Figure 2.10: Spectral profile of the light used in the cavity lock chain, measured by a self-heterodyne beat note using a 3 km long optical fiber. Free-running Vortex ECDL output shown in black. Linewidth reduction from scrubbing cavity lock is shown in blue. Sideband suppression from to the slave diode injection is shown in red. The resolution bandwidth is 10 kHz. The linewidth measurements are limited by the length of the optical fiber.
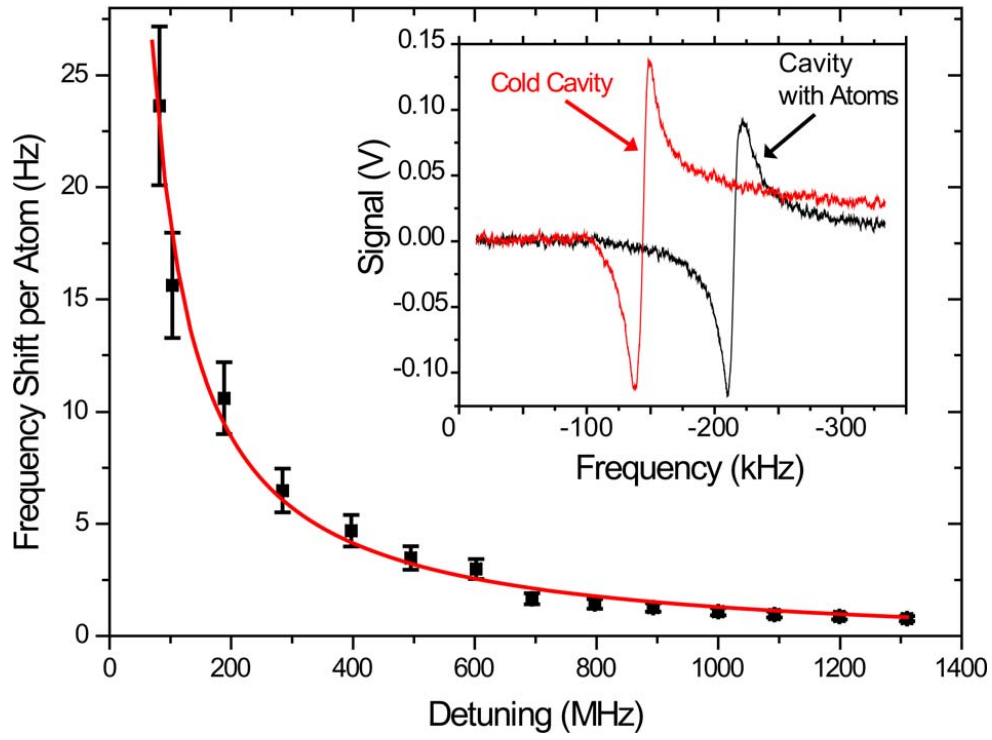
Figure 2.11: The shift of the cavity resonance frequency per atom vs the detuning Δ of the light from the atomic resonance. The red line is a shift of the form $\delta\nu/N = g^2/\Delta$ where g is the atom-cavity coupling parameter.

Chapter 3

Normal Mode Splitting with Large Collective Cooperativity

3.1 Overview

We observe normal-mode splitting of the atom-cavity dressed states in both the fluorescence and transmission spectra for large atom number and observe subnatural linewidths in this regime. We also implement a method of utilizing the normal-mode splitting to observe Rabi oscillations on the ^{87}Rb ground state hyperfine clock transition. We demonstrate a large collective cooperativity, $C = 1.2 \times 10^4$, which, in combination with large atom number, $N \sim 2 \times 10^5$, offers the potential to realize an absolute phase sensitivity better than that achieved by state-of-the-art atomic fountain clocks or inertial sensors operating near the quantum projection noise limit.

Spin-squeezed states (SSS) offer improvements to interferometric sensitivity over classical coherent states (CS) by a ratio related to the collective cooperativity C. This parameter, known as the squeezing parameter ξ is given by [42, 3, 4]:

$$\xi = \frac{\Delta\Phi_{\text{SSS}}}{\Delta\Phi_{\text{CS}}} = C^{-1/4} = \left(\frac{Ng^2}{\kappa\Gamma}\right)^{-1/4} \tag{3.1}$$

where N is the atom number in the cavity mode, κ is the half-width at half-maximum

(HWHM) cavity linewidth, Γ is the natural linewidth of ^{87}Rb, and g is the atom-cavity coupling parameter, also known as the single-photon Rabi frequency.

The theory for vacuum-Rabi splitting due to atom-cavity coupling can be understood both quantum mechanically, in terms of dressed states of an atom-cavity system, as well as classically, in the context of a modified index of refraction, for a single atom as well as for large N [43, 44]. It was initially observed in experiments with thermal atoms both in microwave and optical cavities [45, 46, 47, 48, 49]. In the limit of low excitation, the atom-cavity resonance is shifted from the bare atomic resonance ω_0, and in the limit of $\kappa \ll \Gamma, g$ the energy spectrum forms a doublet separated by

$$\Delta = 2\sqrt{Ng^2 - \frac{\Gamma^2}{4} + \frac{\delta^2}{4}} \tag{3.2}$$

where the detuning $\delta = \omega_0 - \omega_{\rm c}$, and $\omega_{\rm c}$ is the bare cavity resonance. By comparing Eqs. 3.1 and 3.2 we infer the effective ξ of our system for large N, with κ and Γ both known to high accuracy.

This level splitting, derived explicitly for a single excitation, also applies to systems with large photon number ($n \gg 1$) provided that $n \ll N$. For a dressed bosonic system with a large number of excitations, only higher order transitions with energy separations identical to the vacuum splitting have nonzero matrix elements [50]. Previous near-resonant level splitting experiments conducted in the small atom number regime ($N \leq 600$) therefore required $n \sim 1$ [14, 47, 48, 51]. For higher amplitude excitation the level splitting is reduced [51]. Due to the large N in this work, we are able to operate in much higher light intensity regimes. Recent work with large ensembles of atoms ($\sim 10^6$) has observed normal-mode splitting dispersively [52], which also allows for higher photon numbers because dissipation results only from the finite photon-storage time.

Our system, as well as other more recent cavity experiments [16, 52, 53], also deviates from early work through the use of laser cooled atoms in a cavity rather than a thermal atomic beam. Experiments with laser cooled atomic ensembles necessitate the language of atomic wave packets, rather than isolated individual atoms, where the time-averaged spatial extent of these packets spans several wavelengths in a standing
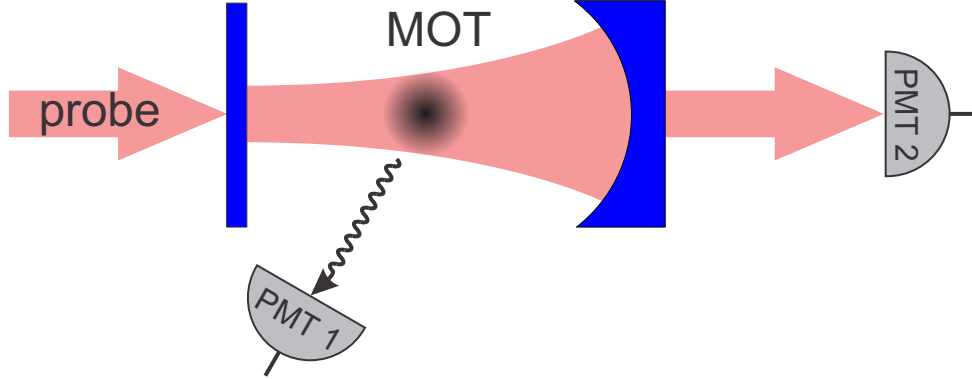
Figure 3.1: Schematic of the cavity, with the MOT loaded on axis at the center of the hemispherical cavity mode. Probe light is incident on the planar mirror, and spectra are measured by two photomultiplier tubes: One for cavity transmission and one for fluorescence.

wave cavity mode [54]. Therefore, if not confined, the atoms in the cavity interact with an inhomogeneous coupling parameter. As atoms traverse the cavity mode standing wave, they see a time average coupling, $g_{\text{eff}}^2 = g^2/2$ [55].

3.2 Experimental Setup

The cavity used in this experiment is the first generation hemispherical cavity described in Section 2.4.2. Atoms are loaded into a magneto-optical trap (MOT) which is overlapped with the center of the TEM_{00} hemispherical cavity mode. Measurements are performed by collecting light in two ways. The first is a fluorescence measurement, performed by collecting photons spontaneously emitted by the atoms on a photomultiplier tube (PMT) located off of the cavity axis. The second is a measurement of the photons transmitted through the cavity on a second PMT. A schematic of the setup is shown in Fig. 3.1.

3.3   Results

We observe the normal-mode splitting, both in the spectrum of light transmitted through the cavity as well as in the atomic fluorescence, by exciting the cavity mode with a weak resonant probe beam coupled into the cavity. We use two Hamamatsu R636–10 photomultiplier tubes, one along the axis of the cavity to detect transmitted light and the other off axis using collection lenses to collect a fraction of the atomic fluorescence (Fig. 3.1). We load the MOT before turning on the probe beam, varying the load time in order to control the atom number in the cavity mode. To minimize background vapor from thermal atoms in the cavity region and to obtain rapid cycle times, we use a collimated atom beam generated in a two-dimensional (2D) MOT chamber to load a 3D MOT situated near the center of a nearhemispherical cavity mode. The cooling light is then extinguished, but the repumping light remains on for an additional 300 μs to ensure the atomic population resides in the $|F = 2\rangle$ ground state. The cavity is tuned to be resonant with the $|F = 2\rangle$ to $|F' = 3\rangle$ atomic transition using a piezoelectric transducer (PZT). It remains stable, within the atom-cavity linewidth, for tens of seconds without the need for an active servo-lock. A New Focus Vortex probe laser is then scanned over 330 MHz in 4 ms from red to blue across the atomic resonance.

Figure 3.2 shows the normal-mode splitting in a fluorescence spectrum detected from the atoms in the cavity mode during a single sweep of the probe beam frequency. As in earlier cavity splitting experiments [47], we observe a subnatural atomic linewidth due to averaging of the cavity and atomic linewidths in our large N regime. We measure a (HWHM) linewidth = 1.74 ± 0.04 MHz with $N \sim 1.3 \times 10^5$. This is close to $\frac{\gamma}{2}/2\pi\hbar$ (for $\gamma \gg \kappa$) as expected in the absence of any background broadening mechanisms.

We plot the normal-mode splitting observed both in fluorescence (empty squares) and transmission (filled squares) in Fig. 3.3. We average over eight frequency sweeps and measure Δ for each N by fitting the data to a double Lorentzian to determine the peak separation. The number of atoms in the cavity mode is calibrated from the maximum observed level splitting using Eq. 3.2 and is consistent with fluorescence
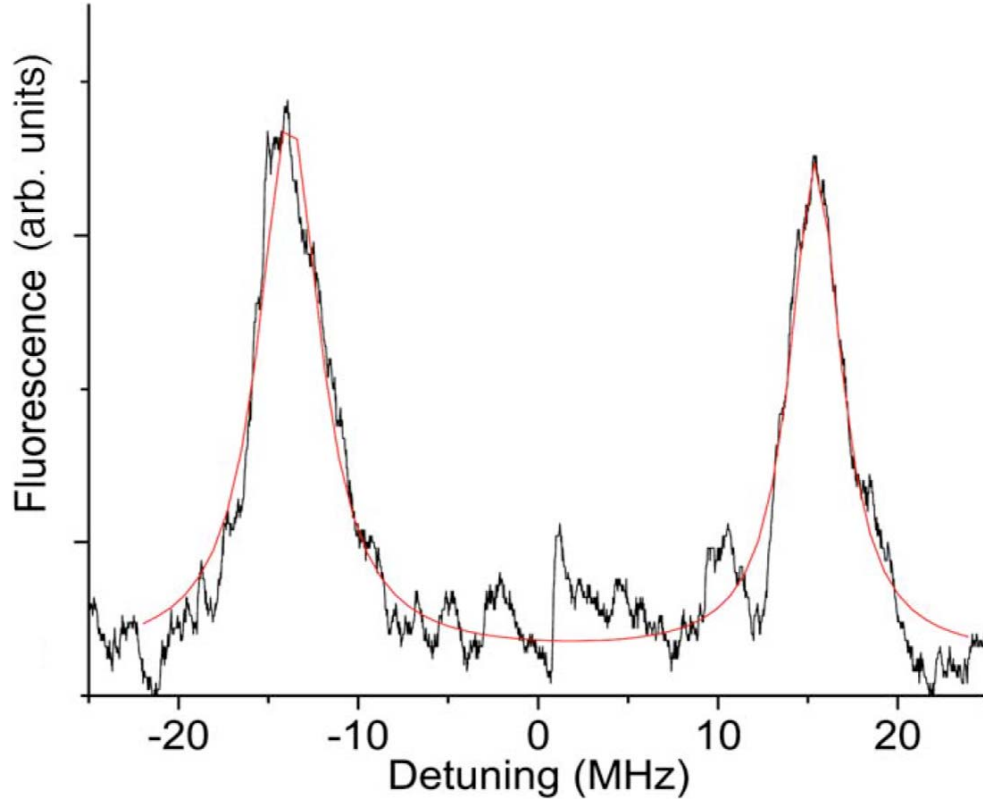
Figure 3.2: The fluorescence spectrum coupled atom-cavity system as a function of the probe light detuning from the uncoupled atomic transition frequency for $N \sim 1.3 \times 10^5$. The data is from a single frequency sweep of 330 MHz in 4 ms. The red curve is a double Lorentzian fit, with each peak having a FWHM width of 3.48 ± 0.08 MHz. The probe power is ~ 450 pW, resulting in peak intracavity photon numbers $n \approx 150$. The temperature of the atoms is 17 μK as measured by ballistic expansion of the atom cloud.

measurements of the MOT atom number and the spatial overlap of the MOT and the cavity mode. For shorter loading times, N is extrapolated from a $1/e$ MOT loading time of 250 ms.

We fit a power law to all of the data and find $\Delta = (2.11 \pm 0.34) \left(Ng^2 - \frac{\gamma^2}{4} \right)^{0.51 \pm 0.04}$, in agreement with Eq. 3.2. The horizontal error bars are determined from a 15% shot-to-shot atom number fluctuation. The fit to the data is best for a large atom number ($N > 1.7 \times 10^4$) where we are comfortably in the low intensity limit $n \ll N$. The transmitted optical power, a neasure of the intracavity photon number, drops suddenly from 450 to 23.5 pW between 1.1×10^4 and 1.6×10^4 atoms. This demonstrates that the atomic transition is partially saturated in this very low N regime, thereby reducing the mode splitting [43, 51] for small N visible in Fig. 3.2.

By optimizing our MOT loading sequence for total N in the cavity, we maximize the observed mode splitting at $\Delta = 32.1$ MHz ($N \sim 2 \times 10^5$) with corresponding $C = 1.2 \times 10^4$ and $1/\zeta \sim 12$. This ζ coupled with large N offers the potential for achieving absolute phase resolution ($\Delta\Phi_{\text{SSS}}$) with nearly twice the sensitivity of the best existing Cs fountain clocks, which operate at the projection noise limit for up to 10^7 atoms [56]. Since our apparatus is far from being in the number density limiting regime, we expect straightforward experimental upgrades to increase N in our cavity mode by at least another order of magnitude.

We next investigate the effect on Δ of varying the cavity detuning relative to the bare atomic transition. With a fixed atom number ($N \sim 1.3 \times 10^5$), we find excellent correlation with the expected splitting for the regime where the cavity is red detuned ($\delta > 0$) from the atomic resonance (Fig. 3.4). When the cavity is blue detuned we see smaller shifts than expected, possibly due to the destructive presence of blue-detuned light from the probe scattered into the MOT volume and causing heating.

Finally, we demonstrate that the cavity normal-mode splitting can be used as a technique for spectroscopic detection. We first load our MOT to saturation and then transfer atoms to the $|F = 1, m = 0\rangle$ from the $|F = 2, m = 0\rangle$ state with a 6.8 GHz microwave pulse. The duration of the microwave pulse, τ, determines the fraction of atoms that remain in the cavitycoupled $|F = 2\rangle$ state. This transfer stage is followed by a laser pulse, blue detuned from the $|F = 2\rangle$ to $|F' = 3\rangle$ transition, which clears
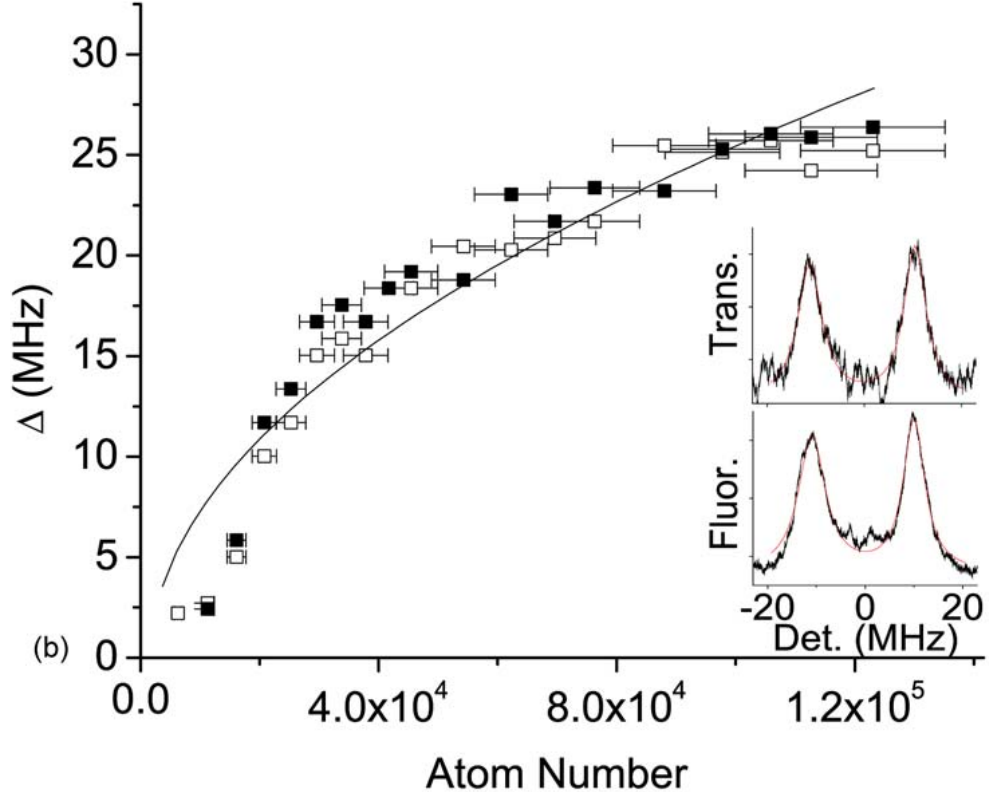
Figure 3.3: Normal mode splitting as a function of atom number. Data are shown for transmission detection (filled squares) and atom fluorescence (empty squares) and is acquired by averaging over eight probe frequency sweeps. Solid line is a power law fit to all data, with $\Delta = (2.11 \pm 0.34)(Ng^2 - \frac{\gamma^2}{4})^{0.51\pm0.04}$. Insets show the fluorescence and transmission spectra for $N \sim 7 \times 10^4$ atoms. The difference in baselines is likely due to the fluorescent emission of photons entering the cavity, causing a drop in the transmission profile.
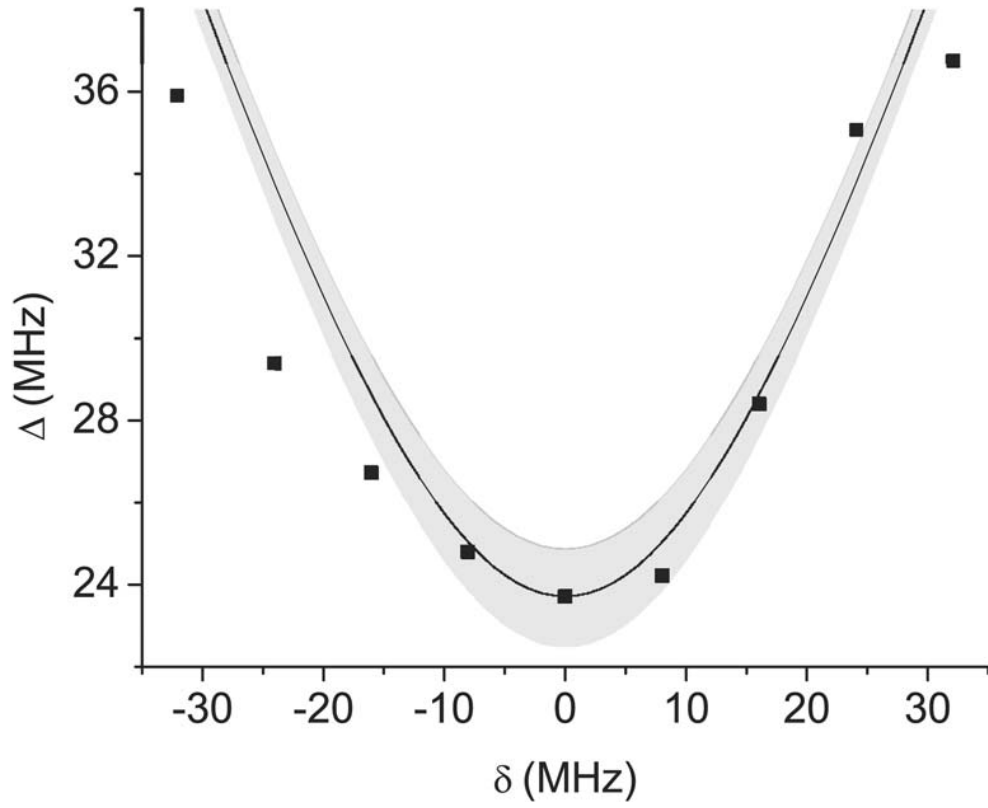
Figure 3.4: Normal mode splitting as a function of the detuning δ of the light from the bare cavity resonance. Solid line shows a plot of Eq. 3.2, where the shaded region denotes the uncertainty due to shot-shot atom number fluctuations.
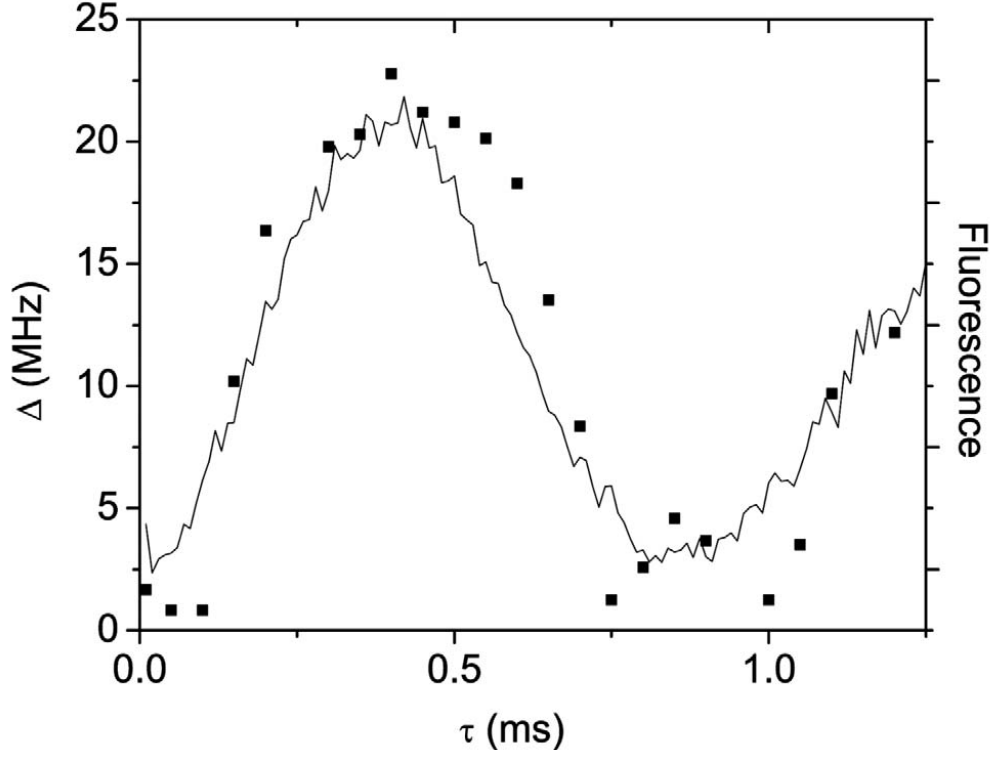
Figure 3.5: Rabi oscillation is plotted vs microwave pulse duration τ. Squares denote normal-mode splitting Δ. Solid line denotes fluorescence detection of atom number in the $F = 2$ hyperfine ground state over the course of the Rabi oscillation, with the fluorescence scale shown on the right-hand side.

away atoms from the MOT that have not been transferred by the microwave pulse. We then apply a repumping light pulse, returning the remaining atoms to the $|F = 2\rangle$ level. We detect this atom population as a function of τ by measuring the normal-mode splitting. We also detected the Rabi oscillations caused by the microwave pulse using conventional fluorescence detection. We see in Fig. 3.5 that the Rabi oscillation, conventionally observed, is reproduced in the oscillation of the normal-mode splitting.

We have demonstrated large collective cooperativity in a cavity system designed to contain large atom numbers in the cavity mode. These two properties show that it should be possible to generate significantly squeezed states using QND techniques to probe the atomic ensemble by way of the light exiting the cavity. Chapter 4 will

describe an experiment demonstrating anti-squeezing, i.e. the increase in the uncertainty of the relative phase of the atomic ensemble that must accompany squeezing.

Chapter 4

Back-action Noise Measurement

4.1 Overview

After demonstrating the large collective cooperativity possible with our cavity, we attempt to demonstrate a squeezed atomic state by using a quantum nondemolition (QND) measurement to probe the collective pseudospin of the atomic ensemble in the high-finesse optical cavity described in Section 2.4.2. We analyze the back-action antisqueezing produced by the measurement process to show that our protocol could create conditional spin squeezing in the atomic ensemble, but are prevented from measuring this squeezing due to technical noise and residual variations in atom-cavity coupling.

4.2 Laser Modulation

The frequency stabilization is similar to that described in Section 2.5, with some changes described here. The slave diode output is now modulated by a single EOM, generating a $\delta\nu_l = 8.99$ GHz locking sideband and a $\delta\nu_p = 9.07$ GHz probe sideband schematically represented as green and orange, resp., in Fig. 4.1(a). This frequency configuration allows the locking sideband to be twice as far detuned from the atomic resonance and reducing the scattering rate due to this ever-present beam.

The light reflected from the cavity is detected by a photodiode, and the resulting
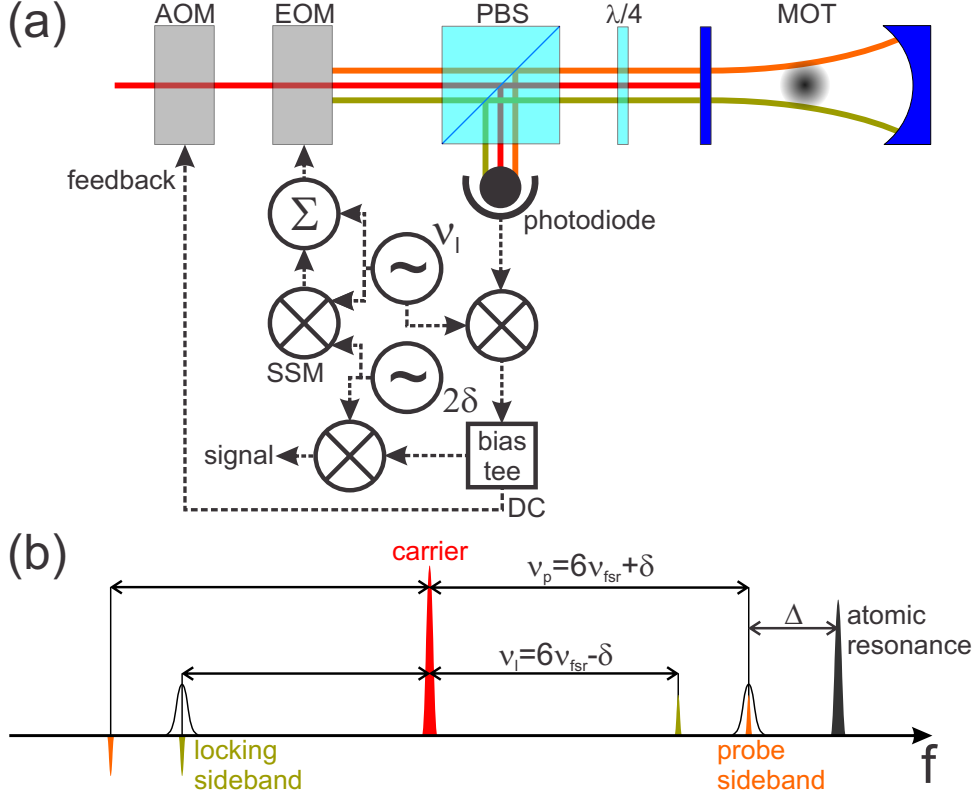
Figure 4.1: Schematic of experiment (a) and modulation method (b). Two sidebands resonant with the cavity are modulated onto a non-resonant laser by an electro-optical modulator (EOM). The locking sideband at a frequency ν_1 is combined with the output of a single sideband mixer (SSM) which generates a probe modulation frequency $\nu_p = \nu_1 + 2\delta$ slightly offset from the lock modulation frequency. A photodiode monitors the beat notes between the carrier and the sidebands reflected from the cavity. The demodulated beat note between the carrier and the locking sideband is used to drive a double-pass acousto-optical modulator (AOM) that keeps the locking sideband resonant with the cavity, while the beat note between the carrier and the probe sideband provides the experimental measurement of the probe phase shift. The open loop AOM frequency is tuned so that the carrier is offset from resonance with a cavity mode by a frequency δ. The probe is detuned from the $F = 2 \rightarrow^5 P_{3/2}$ transitions by an amount Δ on the order of 1-2 GHz, making the excited state hyperfine splitting unimportant.

electronic signal is mixed with a 8.99 GHz local oscillator. The result is two distinct signals: at DC is the component of the signal which is the beat note between the carrier and the locking sideband, and at 80 MHz (the difference frequency between the locking and probe modulation frequencies) is the component which is the beat note between the carrier and the probe sideband. The DC signal is used to feed back to the double-passed AOM, while the 80 MHz signal component can be mixed down to generate the DC probe dispersive signal. The frequency spectrum of the light is shown in Fig. 4.1(b).

4.3 Background

An ensemble of N two-level atoms coupled to a radiation field can be described, in analogy with a spin-1/2 system, by a collective pseudospin Bloch vector of length $J = N/2$, with J_z corresponding to the population difference between the two states [2]. An off-resonant probe laser passing through such an ensemble acquires a phase shift due to the atomic index of refraction, which depends on J_z, without affecting J_z, as long as spontaneous emission remains negligible. A subsequent observation of the probes phase projects J_z onto the value that corresponds to the observed phase shift. The fractional uncertainty in the probe phase is limited by photon shot noise, which thus sets the limit on the uncertainty in J_z, which can be far lower than the projection noise limit for an uncorrelated state. In a cavity, the squeezing factor, which measures the reduction in the projection variance, is enhanced by a factor proportional to the square root of the cavity finesse [3], allowing much stronger squeezing than possible in a free-space configuration.

Quantitatively, assuming identical coupling to the cavity for every atom and ignoring the spontaneous scattering of probe photons into free space and the loss of photons through the cavity mirrors, the Hamiltonian for the interaction of intra-cavity probe light with the atomic state is given by (see, e.g.,[6]):

$$H = \hbar n g_c^2 \left[\frac{N}{2} \left(\frac{1}{\Delta_2} + \frac{1}{\Delta_1} \right) + J_z \left(\frac{1}{\Delta_2} - \frac{1}{\Delta_1} \right) \right] \tag{4.1}$$

where g_c is the atom-cavity coupling constant, $n = a^\dagger a$ and $N = J_{11} + J_{22}$ are the photon and atom number operators, $J_z = 1/2\,(J_{22} - J11)$ is the collective spin projection operator, and $\Delta_{1,2}$ are the detunings of the probe sideband from the lower and upper clock states, respectively. Physically, the atoms experience an ac Stark shift due to the presence of intra-cavity light and the light field experiences a phase shift due to the atomic index of refraction. The term proportional to N only adds an overall phase shift to the light field, so only the term proportional to J_z is relevant for the clock performance analysis.

In our model, the initial state of the system corresponds to a coherent atomic state $|J, J_x >$ and a coherent light state for the intra-cavity probe field. The interaction of the probe sideband and the atoms described by Eq. 4.1 leads to the imprinting on the probe field of a phase shift $\Delta\phi = J_z \Omega t$ for $\Omega = g_c^2 \left(1/\Delta_2 - 1/\Delta_1\right)$, where t is the interaction time, while the collective atomic pseudospin vector precesses in the equatorial plane of the Bloch sphere at a rate proportional to n. Since the probe beam's state is a superposition of number eigenstates (Fock states), each of which causes the atomic pseudospin vector to precess at a different rate, the uncertainty in the atomic pseudospin vector's in-plane component (J_y in the frame that rotates with the atomic state, so it remains polarized along x) grows as it precesses. This growth in ΔJ_y corresponds to the quantum back-action of the measurement of its conjugate variable J_z.

Since the Hamiltonian entangles the collective atomic pseudospin J_z with the phase of the probe field, a measurement of the probe's phase projects the atomic state onto a stochastically determined state of J_z. For $n\Omega^2 t^2 \ll 1$, the resulting uncertainty in J_z, conditioned on the outcome of the phase measurement, is given by $(\Delta J_z)^2 = \left(N/4\right)\left(1 + Nn\Omega^2 t^2/2\right)^{-1}$, compared to the usual projection noise of $(\Delta Jz)^2 = N/4$. A slightly more detailed derivation of these equations is presented in Appendix A.

For interaction times greater than the cavity photon lifetime, the above picture is modified by the leakage of photons out of the cavity. We treat this in a simplified way, by breaking up the interaction time into intervals corresponding to the photon life-time tau_{cav}, where, after each interval, the probe state is measured, and the resulting

atomic state then interacts with a new coherent photon state. The repeated projection out of the intracavity photon state destroys the atom-light coherence between interaction intervals, causing the pseudospin variances to evolve linearly in time. The squeezing for short times, until the antisqueezed uncertainty begins to wrap around the Bloch sphere, is then given by

$$(\Delta J_z)^2 = \left(\frac{N}{4}\right)\left(1 + \frac{N\bar{n}\Omega^2 t\tau_{\text{cav}}}{\sqrt{2}}\right)^{-1}.$$

Here $\bar{n}$ now denotes the time-averaged intracavity photon number, which depends not only on the input power, but also on t and τ_{cav} (in contrast to [57], where all the time dependence is included explicitly), and the corresponding antisqueezing is

$$(\Delta J_y)^2 = \left(\frac{N}{4}\right)\left(1 + \frac{N\bar{n}\Omega^2 t\tau_{\text{cav}}}{\sqrt{2}}\right).$$

Atomic spontaneous emission into free space reduces the correlation between the measured probe phase (to which the atoms that have undergone spontaneous emission contribute) and the collective pseudospin of the atoms used for the clock (to which they do not contribute). If the spontaneous emission rate is known, the average phase shift due to the atoms that have scattered can be subtracted out, but the stochastic fluctuations in that phase shift, given by the shot noise on the number of spontaneous emissions, cannot be accounted for and will degrade the conditional squeezing [58].

4.4   Results

The collective atomic pseudospin is measured via the phase shift produced by the atomic index of refraction on the near-detuned resonant probe sideband. The probe is tuned 1.5 GHz to the red of the $5^2S_{1/2}$, $F = 2 \rightarrow 5^2P_{3/2}$, $F' = 3$ atomic transition with a cavity input power of 1.2-2.5 nW, while the locking beam, 18.06 GHz farther to the red, has an input power of 2.5 nW. The circulating intra-cavity power is amplified by a factor $F/\pi \approx 65,000$.

The correlated atomic state is generated and measured in a three-pulse sequence illustrated in Fig. 4.2. The probe light is turned on for a time τ_{sq}, then turned off for a time τ_{off} required for the probe light to leak out form the cavity, after which a microwave π-pulse that lasts for a time τ_π is used to prepare the spin echo. The probe light is turned on for τ_{sq}, which rephases the atomic spins, then once again extinguished for τ_{off}, and after a possible final microwave rotation, which takes a time τ_{r}, the probe light is turned on permanently and the atomic state is measured for a time τ_{meas}. During the two preparation pulses, spontaneous emission for all data presented here, measured by observing atom depumping over time, is $\leqslant 6\%$; for the final, destructive detection pulse, spontaneous emission is 20%–40%. We use shot-to-shot fluctuations in the difference in the cavity shift between the second squeezing pulse and the final measurement to quantify the conditional projection noise for our protocol.

To properly calculate the expected projection noise, we must account for spatially varying atom-cavity coupling. For a Gaussian atom cloud with radius r_a and a TEM_{00} standing wave cavity mode with beam waist r_c, the mean atom-cavity coupling $\overline{\Omega}$ is less than the maximal on-axis, antinode value Ω_{max} by a factor of $2[(r_a/r_c)^2 + 1]$, calculated from the overlap integral between two Gaussians, and assuming a standing wave along the cavity axis. The variable that the probe phase measurement couples to is then not ΩJ_z, but $\overline{\Omega}J_z$, with an uncorrelated projection noise variance given by the sum of the individual atom variances. Since the inhomogeneous transverse coupling of different atoms does not average out on the time scale of our measurement, this modified collective variance scales not as the square of the mean coupling, but rather as the mean of the squared coupling:

$$\left(\Delta\overline{\Omega}J_z\right)^2 \;=\; \sum_{i=1}^{N}\left(\Delta\Omega_i j_{z,i}\right)^2 \tag{4.2}$$

$$=\; \left(\frac{N}{16}\right)\frac{\Omega_{\mathrm{max}}^2}{2[(\frac{r_a}{r_c})^2 + 1]} \tag{4.3}$$

where i is an index over individual atoms [the unmodified value is $(\Delta Jz)^2 = (N/4)\Omega_{\mathrm{max}}^2$].
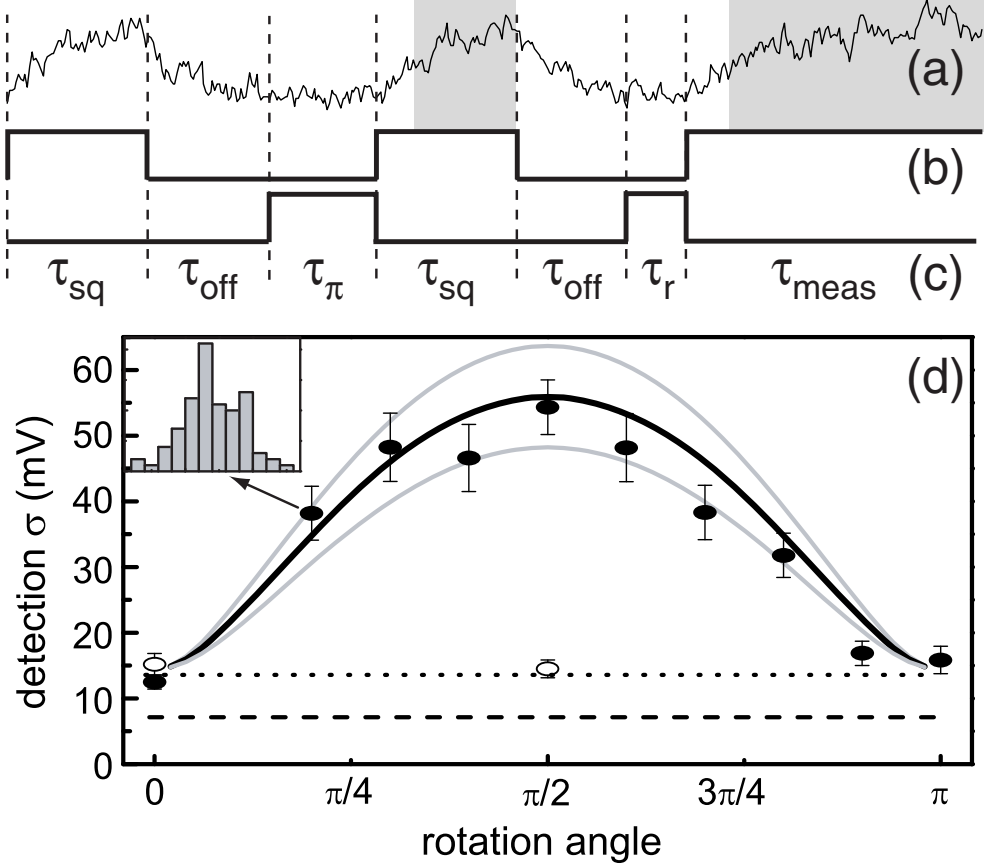
Figure 4.2: Measurement protocol and results. The traces show a typical probe signal (a), along with the control sequences for the probe laser (b), and the microwave state rotation (c). The results obtained for the fluctuations in the difference between the means of the two shaded regions in (a), chosen to exclude the initial cavity buildup, as we vary the duration τ_r of the final microwave pulse are shown as solid circles in (d), with each data point corresponding to 58-174 shots, with statistical error bars. The inset in (d) shows a histogram of the difference of means for 87 shots at a final rotation of 0.63 rad, the standard deviation of which corresponds to the y-axis value of the indicated data point. The solid curve is a theory calculation using our model; the gray curves account for uncertainties in the experimental parameters, dominated by uncertainty in intra-cavity probe power; the dashed line is the expected projection noise; and the dotted line is the measured noise floor in the absence of atoms (detector dark noise is negligible). The open circles indicate the results obtained for inhomogeneous broadening in the absence of spin echo (see text). The parameters for this measurement are $\tau_{sq} = \tau_{off} = 60~\mu s$, $\tau_\pi = 50~\mu s$, $N \approx 57000$, Δ is 1 GHz, probe power ≈ 2.5 nW, and locking power ≈ 2.5 nW. The microwaves are resonant with the $m_F = 0 \, rightarrow \, m'_F = 0$ transition.

To take advantage of the squeezing produced by our protocol, subsequent measurements also need to couple to $\overline{\Omega}J_z$, which suggests that interferometer readout should be performed using the cavity shift [59].

By applying a microwave pulse before the final detection pulse, it is possible to rotate the uncertainty ellipse around its center and use the atomic shift to measure its width in an arbitrary direction. A $\pi/2$ pulse rotates the antisqueezed J_y component of the collective atomic spin onto a population difference J_z, which results in maximal noise on the shift, while a smaller rotation produces a correspondingly smaller effect. The results of such a series of measurements are shown in Fig. 4.2(d).

To characterize the coherence of our atomic states, we vary the phase of the final microwave pulse while keeping its duration fixed at $t_{\pi/2}$ by applying a phase offset to the microwave oscillator that generated the pulse. We thus scan the collective pseudospin rotation axis in the equatorial plane of the Bloch sphere, which produces an oscillation in the atomic populations, which we read out via the mean values of the final probe measurement. For the final state produced by our measurement, the contrast in this oscillation is about 73% of the full contrast obtained under the same circumstances in the absence of probe squeezing pulses, which means that the length of the collective spin vector on the Bloch sphere is reduced to 73% of its initial length due to the relative dephasing of the individual spins by the squeezing pulses and the projection noise is reduced by the same amount. We have also confirmed that the lock light has no effect on atomic coherence by comparing the contrast measured after the spin echo sequence without squeezing pulses to the initial contrast measured immediately after the first $\pi/2$ pulse creates the clock-state superposition.

It is important to distinguish between inhomogeneous broadening due to the spatially varying probe light intensity, which leads to dephasing between the pseudospin states of different atoms, and the dephasing of the collective pseudospin – i.e., antisqueezing. To study the two effects independently, we use the fact that spin echo counteracts the majority of the inhomogeneous dephasing, making it possible to produce, without spin echo, the same amount of inhomogeneous dephasing contrast reduction with a much shorter probe pulse (and, consequently, much less antisqueezing). We
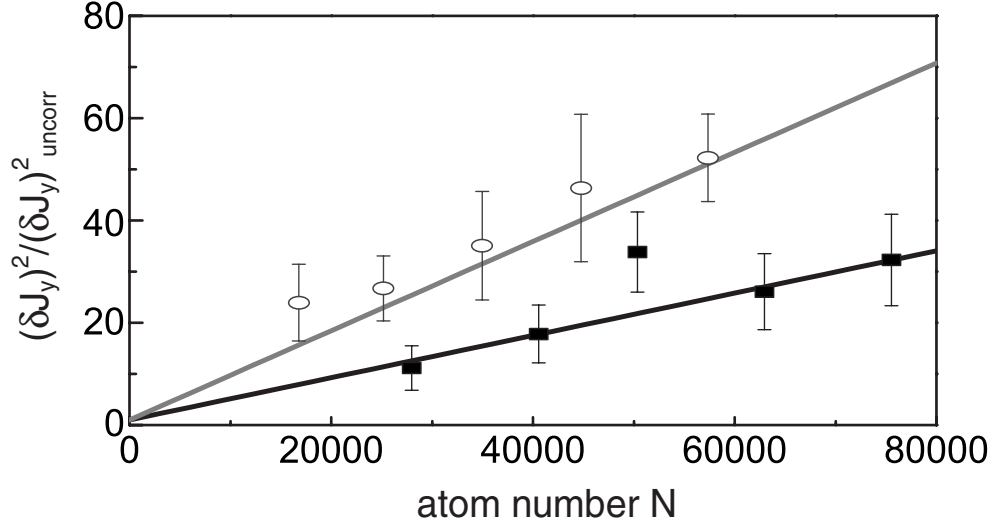
Figure 4.3: Increase in antisqueezing of the variance of the in-plane component of the atomic pseudospin (conjugate of J_z) relative to the coherent state value as a function of atom number and probe intensity, obtained by rotating the spin state after the two squeezing pulses (see Fig. 4.2) by $\pi/2$ and measuring the probe phase shift. The black squares and white circles correspond to probe input powers of ≈ 1.2 nW and ≈ 2.5 nW, respectively, with statistical error bars. The lines correspond to theory calculations using our model; there is an overall scaling uncertainty of $\pm 30\%$ from probe power measurements. Fitting the slopes for the two data sets as free parameters gives $9.7(4) \times 10^{-4}$ and $4.5(5) \times 10^{-4}$ /atom, with a ratio of 2.2(3), in good agreement with the ratio of the input powers (2.1).

find that a 20 μs probe pulse without spin echo produces the same amount of inhomogeneous dephasing (as measured by microwave oscillation contrast) as two sequential 60- s probe pulses with spin echo. However, the 20 μs pulse does not produce a measurable increase in noise [see open circles in Fig. 4.2(d)].

We measured the antisqueezing as a function of atom number for two different probe intensities. The results, along with theoretical calculations are shown in Fig. 4.3. The observed linear scaling with atom number N and with probe intensity, and therefore average photon number $\bar{n}$, confirms the validity of our measurement protocol. Variance due to classical intracavity intensity fluctuations would scale quadratically with $\bar{n}$ (we independently measure these fluctuations to be below 0.08% between the two squeezing pulses).

While we are not able to observe squeezing for 60 μs squeezing pulses, using the same protocol with longer pulses, which destroy Rabi oscillation coherence, allows us to resolve J_z to 3.8 dB in the variance below the projection noise for an uncorrelated state with spontaneous emission loss of $\leq 30\%$. Technical measurement noise and residual variations in atom-cavity coupling limit our ability to observe squeezing while preserving coherence. If the probe could be measured at the photon shot-noise limit for the second squeezing pulse and taking into account the atomic loss dictated only by the spontaneous emission and not by inhomogeneous broadening, the anti-squeezing shown in Fig. 4.3 would, for a minimum-uncertainty state, correspond to spin squeezing of up to 10 dB in the variance.

Significantly better performance could be achieved by increasing the atom number (a typical ^{87}Rb MOT with 10^8 atoms should give us measurement samples of 10^7 atoms, a hundredfold increase) and by improving the spatial overlap between the cavity mode and the atom cloud, by either confining or cooling the atoms. The addition of a far-detuned (1560 nm) trapping beam can provide the necessary confinement, as well as suppress the residual variations in the atom-cavity coupling due to atomic motion through the standing wave probe electric field. Additionally, by stabilizing the laser system at 1560 nm we will effectively remove the ever-present locking sideband which is a continual source of scattering. The next chapter describes and characterizes the dual-wavelength cavity.

Chapter 5

Dual-Wavelength Confocal Cavity

5.1 Motivation

The goal of our improved cavity design is to provide a method for confining the atoms, in order to prevent movement across the probe beam's standing wave profile. This motion causes a strongly time-varying coupling strength of the atoms to the probe beam, which is a limiting source of noise in the hemispherical cavity used in Chapters 3 and 4. In addition, the confinement must preserve coherence in order to ensure that the atomic sample will be useful for interferometry, squeezing, etc.

5.2 Differences compared to previous generation

To meet this goal, we construct a cavity which has a high finesse at two wavelengths. It retains the high finesse at 780 nm from the previous generation for probing the atoms, but now it also has a high finesse at 1560 nm, double the probe wavelength. The ability to couple 1560 nm light into a high finesse cavity allows for the use of a high intensity, far off-resonant standing wave dipole trap. The atoms are attracted to the antinodes of the dipole trap's electric field which, due to the trap wavelength being almost exactly double the probe wavelength, line up well with antinodes of the 780 nm light at the MOT position equidistant between the two cavity mirrors. Atoms trapped at the antinodes experience an essentially time-invariant maximal coupling

of the light to the atoms.

The ^{87}Rb source is now a current driven vapor source manufactured by Alvatec, replacing the time-consuming Rb transfer procedure necessary in the previous generation. The source was spot welded to feedthrough leads through which the current is driven. The metal flange with the feedthrough is connected to the Zerodur vacuum chamber on the 2D-MOT side by an indalloy seal. Indalloy is an Indium alloy with properties similar to indium, but which has a higher melting point (~ 120 °C), permitting a bake-out at higher temperatures than an indium seal would allow. The ^{87}Rb source was activated after 24 hours of baking by briefly driving it with a 4 A current, melting the internal Indium seal and exposing the internal Rb compound to the chamber. The current was then lowered to 2 A, and allowed to bake for another 24 hours. The indium in the other glass-to-metal seal, connecting the ion pump to the Zerodur vacuum chamber, was also replaced with indalloy.

The cavity is no longer in a hemispherical configuration, but is now near-confocal. Confocal cavities have a narrow beam waist, located at the point equidistant from the cavity mirrors and coinciding with the atoms' location. Because the atoms will be trapped in the antinodes of the lattice beam, uniform coupling should be guaranteed without the necessity of a large beam waist, and the narrow beam waist allows for increased atom-cavity coupling. Furthermore, because the beam waist at the center of the confocal cavity mode depends only weakly on the cavity length L, we are insensitive to the specific cavity length used. This means we are able to replace the Zerodur end-caps from the first generation cavity with Zerodur disks which do not go into the cavity tubes, allowing us to use the same high glass temperature Epotek 353ND epoxy used to attach the cavity tubes to the vacuum chamber. The elimination of the indium seals and the low glass temperature epoxy from our system allows us to bake at much higher temperatures, and the resulting final pressure of this system is a few 10^{-10} mbar.

5.3 Cavity construction

The "science" cavity was constructed in a near-confocal configuration, with two $R_C = 10$ cm radius of curvature mirrors. The mirror coating is now highly reflective at 780 nm and 1560 nm, with manufacturer (Research Electro-Optics) specified reflection coefficients of $R_p > 0.99994$ and $R_l > 0.99992$. Here the "p" and "l" subscripts refer to the probe at 780 nm and lattice at 1560 nm, resp. This notation will be used henceforth.

The free spectral range was measured to be $\nu_{\mathrm{fsr}} = 1.396$ GHz, corresponding to a mirrors separation of $L = c/2\nu_{\mathrm{fsr}} = 10.73$ cm, ~ 730 μm longer than perfectly confocal. The cavity mode has a beam waist of $w_0 = w(L/2) = 111$ μm at the center of the cavity, where the atoms are loaded. This leads to an atom-cavity coupling constant $g_0 = 2\pi \times 53$ kHz for the $|F = 2, m_F = 2\rangle \rightarrow |F' = 3, m_{F'} = 3\rangle$ transition for atoms located on axis at a probe field antinode in the center of the cavity. The cavity ring down times $\tau_p = 19.9$ μs and $\tau_l = 13.3$ μs were determined by using an AOM switch to shut off the driving beams, and measuring the $1/e$ decay time of the cavity output. The resulting traces are shown in Fig. 5.1. This corresponds to half-width-half-max cavity linewidths $\kappa_p = 2\pi \times 3.99$ kHz and $\kappa_l = 2\pi \times 5.98$ kHz, or finesses $F_p = 175{,}000$ and $F_l = 117{,}000$. The single-atom cooperativity $\eta = g_0^2/\kappa\Gamma = 0.83$, where $\Gamma = 2\pi \times 6.067$ MHz is the ^{87}Rb natural linewidth. Table 5.1 summarizes the important cavity parameters.

The optical path for most of the experiments is summarized in Fig. 5.2. Light from a 1560 nm New Focus Vortex laser is stabilized to a 1560 nm "scrubbing" cavity. This cavity has a linewidth ~ 6.5 kHz, and is used to reduce the laser linewidth from ~ 300 kHz to below 1 kHz. The transmitted light is frequency shifted by an acousto-optical modulator (AOM) and injected into a slave diode. The diode output is amplified by an IPG EAR-2K fiber amplifier to a maximum output power of 2 W. The fiber amplifier output is split into two paths.

One path goes to the science cavity after being modulated by an electro-optical modulator (EOM), and generates the Pound-Drever-Hall [38, 39] error signal used to stabilize the light. The error signal controls a voltage-controlled oscillator driving the
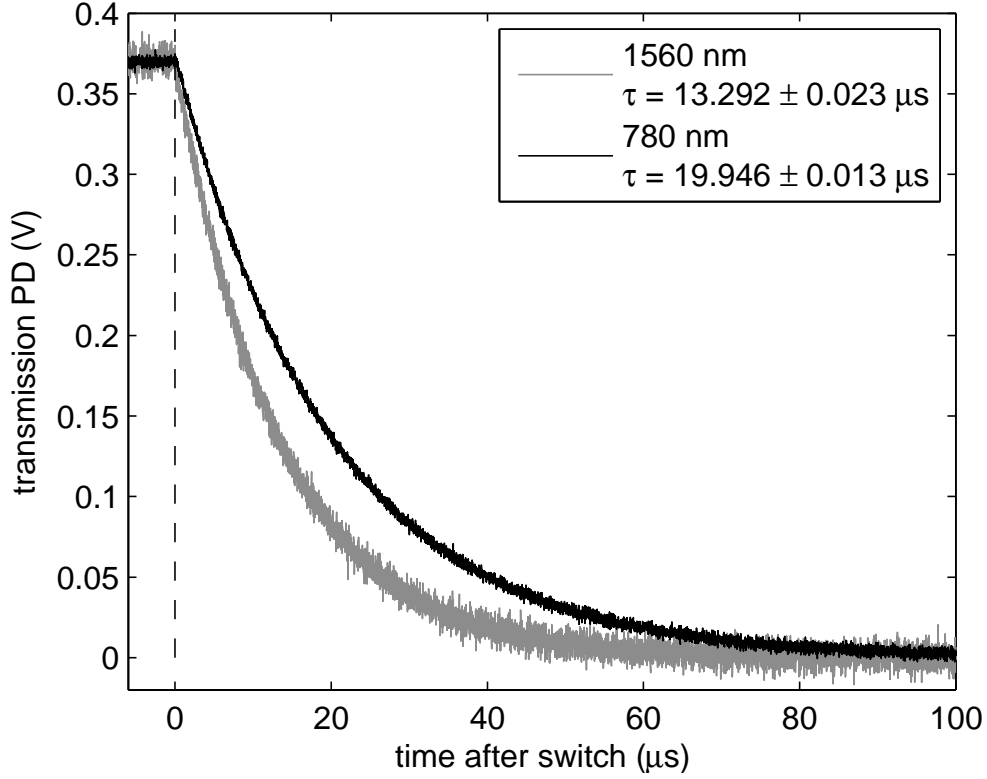
Figure 5.1: Ringdown traces for the 780 nm probe (black) and 1560 nm lattice (grey) wavelength. The specified τ is the time constant of an exponential decay fit. The dashed vertical line at $t = 0$ denotes the time the input light is switched off.

parameter	symbol	Values		units
wavelength	λ	780	1560	nm
curved mirror radius	R_c	9.9		cm
length	L	10.73		cm
free spectral range	ν_{fsr}	1.396		GHz
beam waist at atoms	w_0	111	157	μm
atom-cavity coupling at atoms	$g_0/2\pi$	142		kHz
ringdown time	τ	19.9	13.3	μs
decay rate (HWHM)	$\kappa/2\pi$	3.99	5.98	kHz
Finesse	F	175,000	117,000	
single-atom cooperativity at atoms	η	0.83		

Table 5.1: Summary of important cavity parameters at both the probe (780 nm) and lattice (1560 nm) wavelengths.

AOM which allows for feedback on the optical frequency of the light. We stabilize the light such that one of the EOM modulation sidebands is resonant with the science cavity. By controlling the magnitude of the modulation voltage to the EOM we can control the amount of light in the sideband, and therefore we have direct control over the trap intensity.

The second path goes to a periodically poled lithium niobate (PPLN) waveguide, which frequency doubles the light to the 780 nm used for the probe laser. The 1560 nm light is reflected by a dichroic beam splitter (DBS) and goes to an optical spectrum analyzer a a diagnostic for coarse frequency tuning. The 780 nm light from the PPLN passes the DBS and is injected into a slave diode, the output of which is phase modulated by a electro-optic fiber modulator to generate sidebands used in the detection. The heterodyne detection scheme uses the 780 nm carrier as a stable phase reference, while the resonant sideband experiences an optical path length-dependent phase shift. Atoms in the cavity will change the optical path length (and hence the phase) by an amount $\propto \Delta^{-1}$, the atom-light detuning. This atom-dependent phase difference between the carrier and sideband can be readily turned into a dispersive voltage signal and recorded. Alternatively, we can measure the transmitted 780 nm probe light with a fiber-coupled Perkin-Elmer single photon counting module (SPCM).

The resulting frequencies (both at 1560 nm and 780 nm) are shown in Fig. 5.3 together with the cavity resonance frequencies separated by ν_{fsr}. An advantage of this configuration is that the 780 nm carrier is far detuned from any cavity resonance, heavily suppressing its transmission through the cavity. The carrier is approximately a million times more intense than the probe sidebands, and good carrier suppression is required when using the SPCM to measure the transmission of the probe sideband.

5.4   Thermal shifts and demonstrated trapping

Typical operating conditions require us to couple up to 1 mW of 1560 nm trapping light into the cavity. Inside the cavity the intensity builds up to a circulating power of ~ 40 W. The high circulating power creates a high heat load on the cavity mirrors, which causes them to thermally expand slightly. As our measurement procedure is
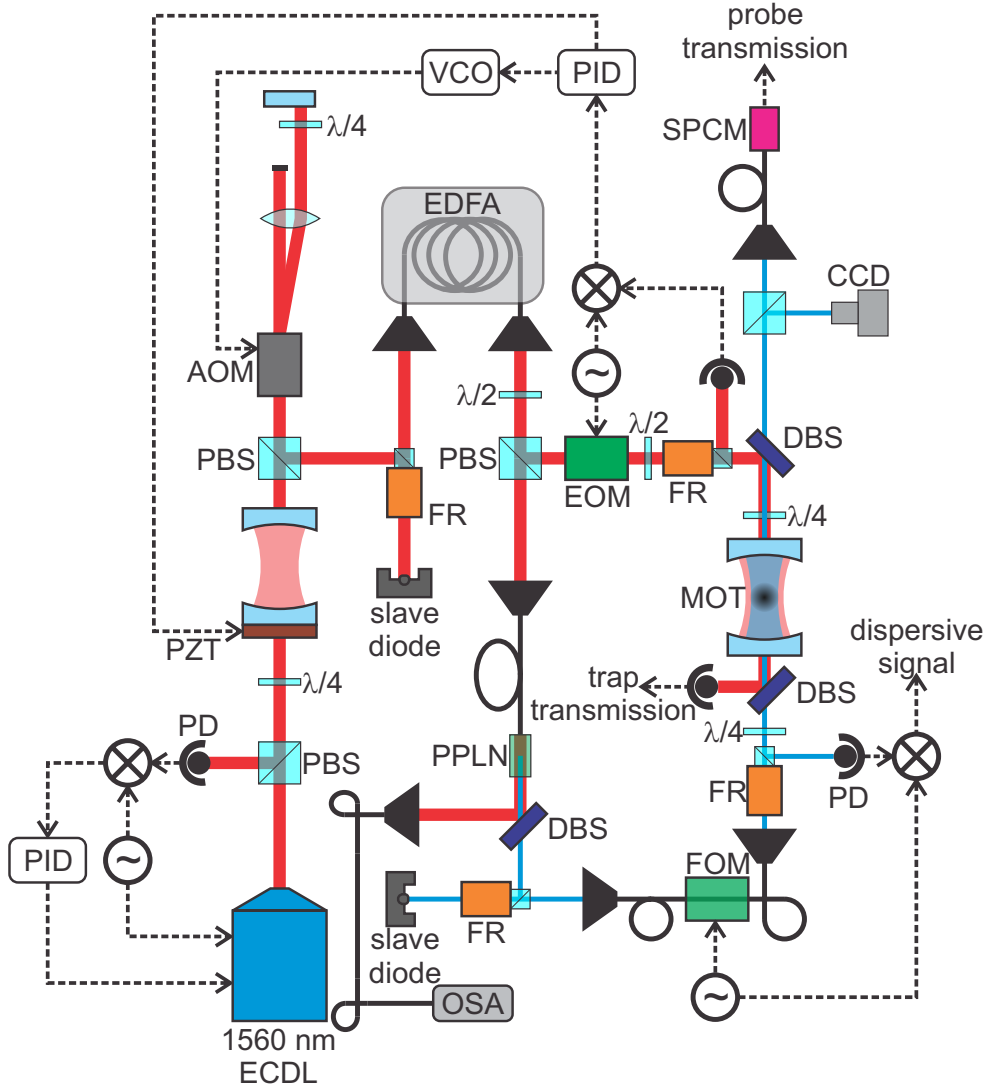
Figure 5.2: Detailed schematic of the optical and electronic paths. Red lines are 1560 nm light, blue lines are 780 nm light, solid black lines are optical fibers, dashed black lines are electrical signals. ECDL = Extended Cavity Diode Laser, PBS = Polarizing Beam Splitter, $\lambda/2$ = half-wave plate, $\lambda/4$ = quarter-wave plate, PD = Photodiode, PZT = Piezoelectric Transducer, PID = Proportional-Integral-Differential gain controller, VCO = Voltage Controlled Oscillator, AOM = Acousto-Optical Modulator, EOM = Electro-Optical Modulator, FR = Faraday Rotator, EDFA = Erbium-Doped Fiber Amplifier, PPLN = Periodically Poled Lithium Niobate frequency doubling crystal, DBS = Dichroic Beam Splitter, SPCM = Single Photon Counting Module, OSA = Optical Spectrum Analyzer.

Figure 5.3: The optical frequencies of the light shown together with the cavity res-
onances. The resonant sideband at 1560 nm generates the dipole potential which
confines the atoms. The carrier at 1560 nm gets frequency doubled to generate the
carrier at 780 nm. Sidebands are generated at 44 MHz by an electro-optic modulator
(for the 1560 nm beam) and at 6.01 GHz by a fiber modulator (780 nm).
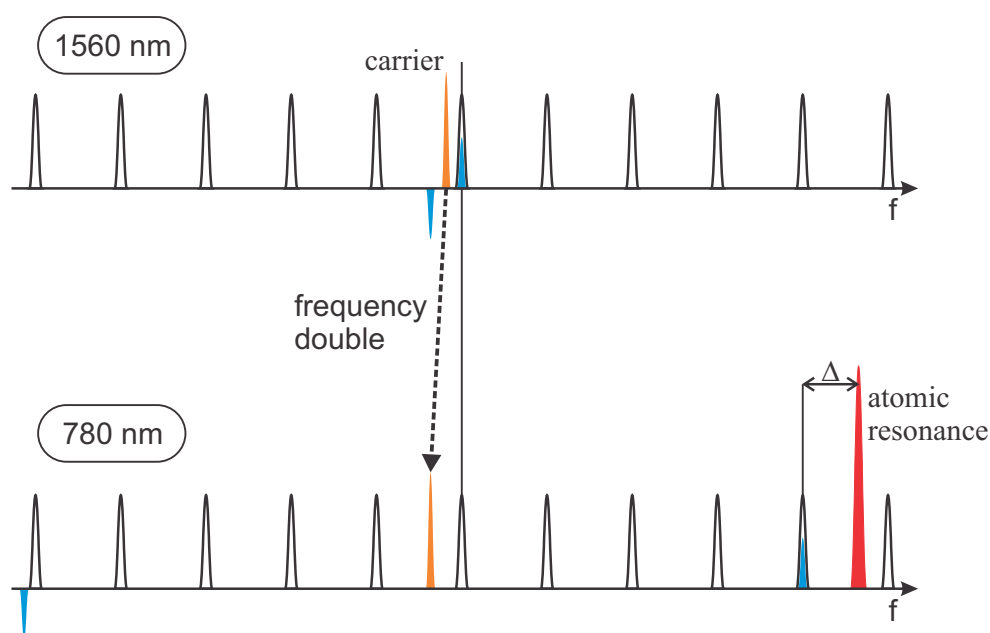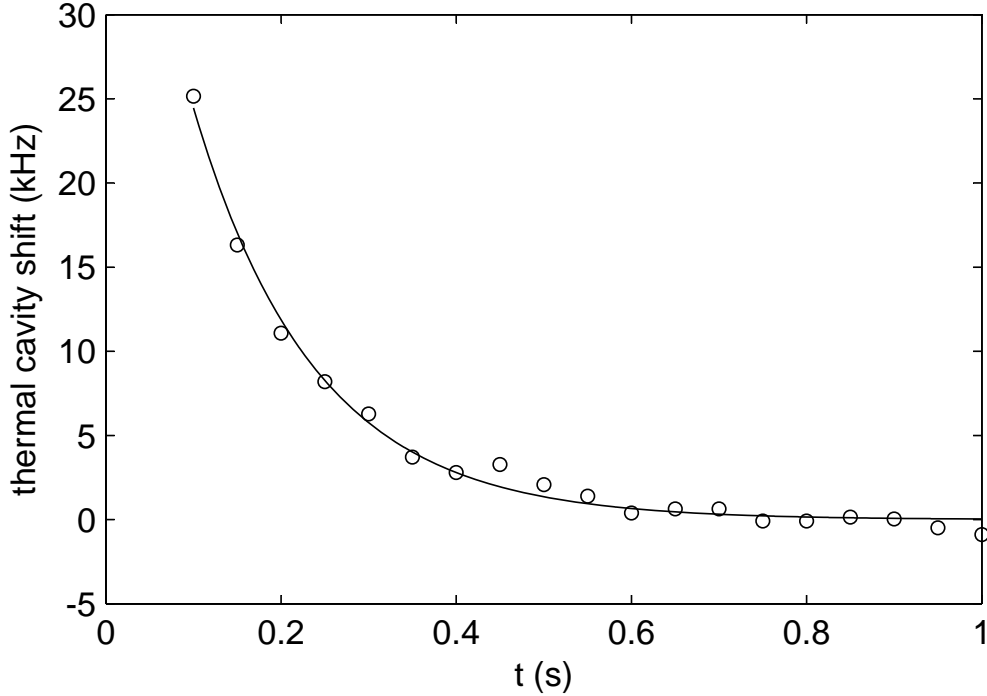
Figure 5.4: The cavity resonance shifts (in kHz) due to thermally induced expansion of the mirrors by the intra-cavity light from a 0.5 mW incident trap beam. The shift is for an empty cavity (no atoms), and the time is given after the intense probe is turned on. The frequency shift of the 780 nm probe at $t = 0$ is approximately 2.5 kHz per W of circulating intra-cavity 1560 nm light. Circles are data and the solid line is an exponential fit with a decay time of 138 ± 7 ms.

very sensitive to cavity length changes this shows up as a time-dependent drift in the measured resonance frequency of the cavity, starting when the cavity intensity is turned up (after the MOT is loaded), and exponentially decaying with a time constant of 138 ± 7 ms, as shown in Fig. 5.4.

It should be noted that this thermal effect can only be visible if the cavity length change at 1560 nm and 780 nm is different. Any length change that is common to both frequencies is canceled out by virtue of the frequency doubling crystal. A consequence of this is that the cavity has a different length at 1560 nm and 780 nm. This will be further investigated in Section 5.6.

We demonstrate our system's capability of trapping atoms by measuring the change in the cavity resonance frequency as a function of time and subtracting out
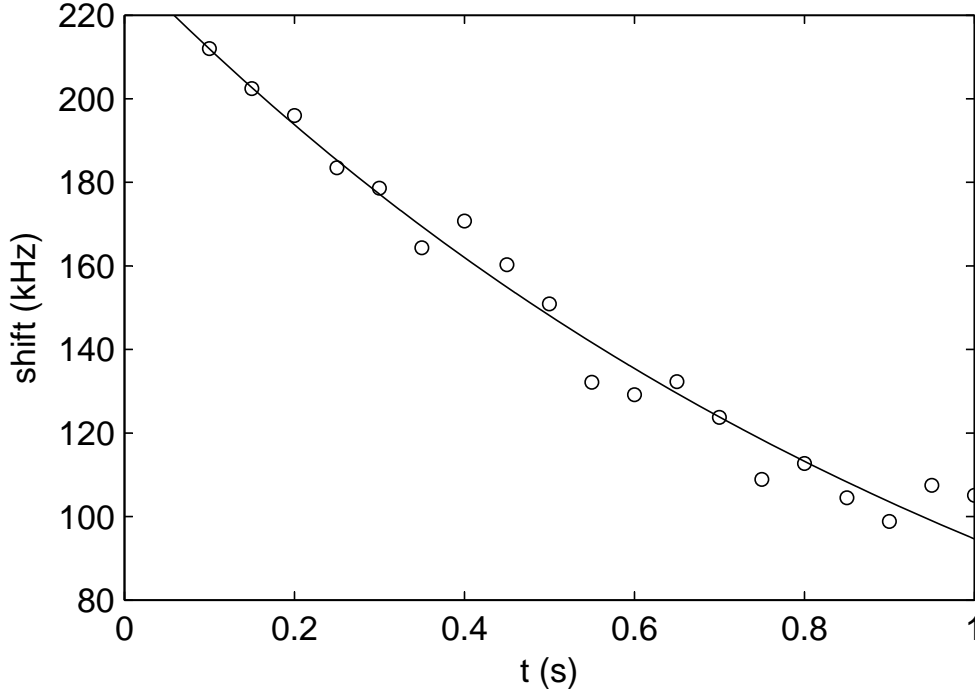
Figure 5.5: The shift (in kHz) of the cavity resonance at 780 nm due to atoms loaded into the dipole trap as a function of time after the MOT beams have been turned off. The circles are data and the solid line is a fit with a decay time of 1.12 ± 0.05 s. Data shown is for 0.68 mW of trap light resonant with the cavity.

the thermal shift from Fig. 5.4. As is shown in Fig. 5.5, we are able to trap atoms for times upward of a second, making it possible for us to trap atoms, hold them while the thermal shift dies out after ~ 0.5 s, and perform our experimental protocol afterwards, thus minimizing the impact of any thermal effects on the cavity mirrors due to the intense trapping beam.

By measuring the cavity shift of a fixed number of atoms for a varying detuning we find that the measured curve asymptotes to a non-zero detuning, as shown in Fig. 5.6. As the detuning increases the shift per atom will drop off as $(\Delta - \nu_{\mathrm{AC}})^{-1}$ where Δ is the detuning from the unshifted $F = 2 \rightarrow F' = 3$ transition, and ν_{AC} is the AC Stark shift due to the trapping beam. A fit indicates $\nu_{\mathrm{AC}} = 523 \pm 65$ MHz.

This effect is due to the higher lying states of ^{87}Rb, specifically the 5D and 6S levels which are 1529 nm and 1366 nm above the $5P_{3/2}$ state, as shown in Fig. 5.7.
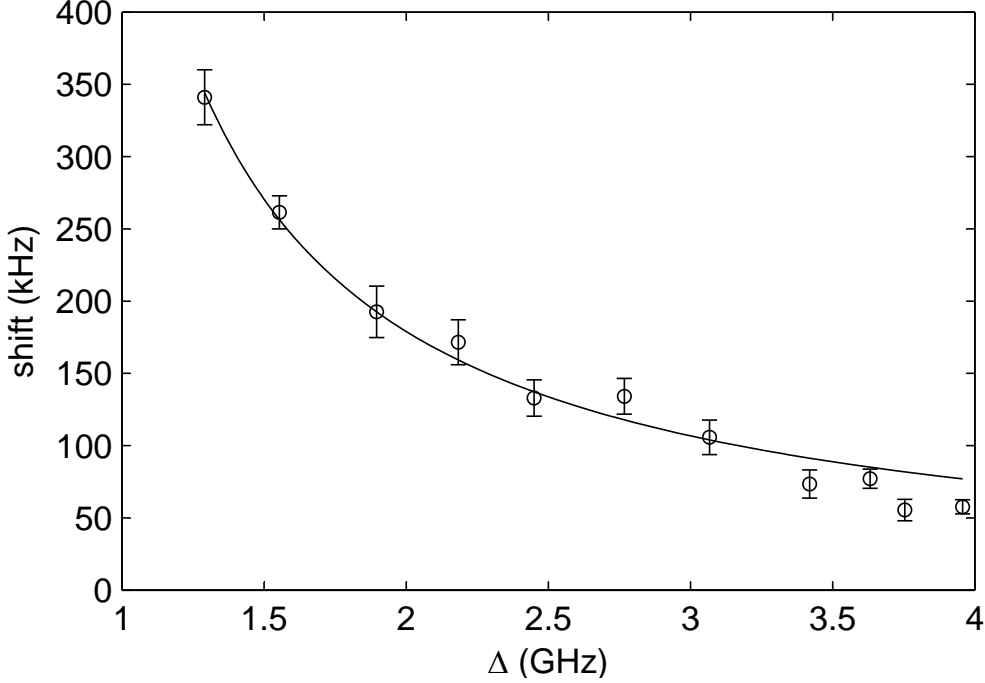
Figure 5.6: Resonance frequency shift of the cavity at 780 nm as the probe frequency detuning from the unshifted $F = 2 \rightarrow F' = 3$ transition (Δ) is changed. The solid line is a fit with shift $= A/(\Delta - \nu_{AC})$ where $\nu_{AC} = 523 \pm 65$ MHz.

The $5P_{3/2}$ excited state is Stark shifted due to the strong 1560 nm trapping beam addressing the 1529 nm ($5P_{3/2} \rightarrow 4D$) transition. This results in a net AC Stark shift which is a factor 41.6 larger (and in the same direction) than the Stark shift of the 5S ground states due to the trapping beam [60]. In the absence of higher lying states, the $5P_{3/2}$ shift would be equal in magnitude and opposite in direction compared to the 5S ground state.

An intense 1560 nm trapping beam creates a strong spatially dependent Stark shift which interferes with MOT loading due the MOT lasers not being properly detuned everywhere in space. To counter this effect we can lower the modulation drive power to reduce the Stark shift to the point where it has a negligible effect on the MOT loading. When the MOT is fully loaded we can ramp up the trap depth and simultaneously turn off the MOT beams to release the atoms, capturing them in the dipole trap.
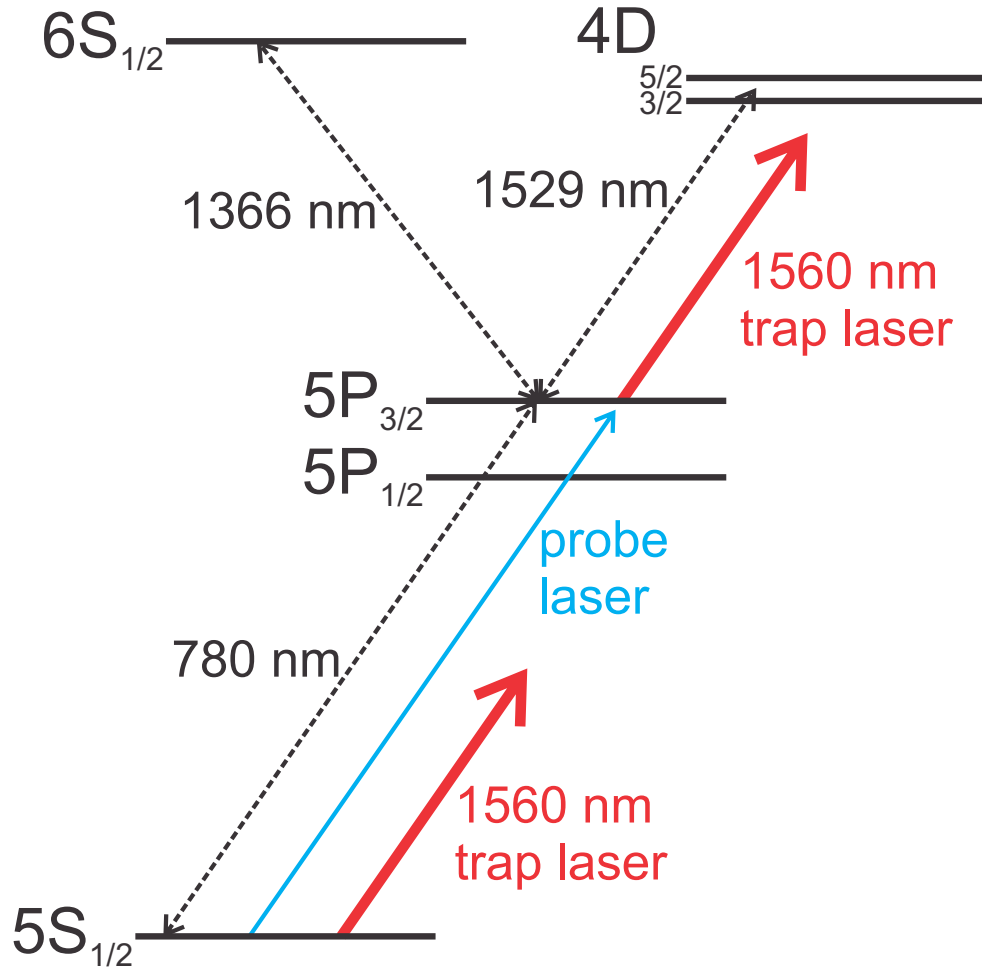
Figure 5.7: The 5S ground state of ^{87}Rb along with the three lowest energy excited states. The dashed black arrows indicate the wavelength of relevant transitions, while the blue and red arrows denote the probe and trapping laser wavelengths, resp. The $5P_{3/2}$ level, which is involved in the probe beam transition, is Stark shifted by the presence of the higher lying ($5P_{3/2} \rightarrow 4D$) 1529 nm transition being addressed by the strong 1560 nm trapping beam.

5.5   Coherence in the trap

Successful atomic physics experiments rely on coherence times long enough to complete the desired experimental protocols. One of the most common manipulations of the alkalis is to drive the microwave transition between the two hyperfine ground states to see Rabi oscillations or Ramsey fringes. In order to see Rabi oscillations we drive the atoms to the $|F = 1\rangle$ ground state by briefly pulsing on a beam resonant with the $|F = 1\rangle \rightarrow |F' = 2\rangle$ transition to get all the atoms in the $|F = 2\rangle$ ground state. The we apply a microwave pulse of a variable duration and measure the shift of the cavity resonance. The result is shown in Fig. 5.8(a).

Our Ramsey fringe protocol starts by pumping all the atoms to $|F = 2\rangle$, as in the Rabi oscillation measurement, followed by a $\frac{\pi}{2}$-Δt hold-π-Δt hold-$\frac{\pi}{2}$ pulse sequence. The first $\frac{\pi}{2}$ pulses put the atoms in a coherent superposition of the two hyperfine ground states, the middle π-pulse reverses the overall phase of the atomic state to compensate for any broadening due to inhomogeneities in the Stark shift, and the second $\frac{\pi}{2}$-pulse is phase shifted from the first by a variable amount. In the absence of decoherence, as the phase is varied the final phase shift will oscillate between the extremes of total population transfer (no phase difference between the pulses) to zero population transfer (2π phase difference). Decoherence will decrease this amplitude as a function of the hold time $2\Delta t$, as shown in Fig. 5.8(b).

This demonstrated ability to trap and coherently hold atoms for about 212 ms is enough for the planned spin squeezing experiments using this apparatus. The experimental protocol from Chapter 4 takes less than 5 ms, a time during which the measured coherence in our system is essentially unchanged. Additionally, at maximum microwave power our system has the potential to go through 500 Rabi oscillations in the measured decay time, a property which could make this apparatus useful in quantum information processing.
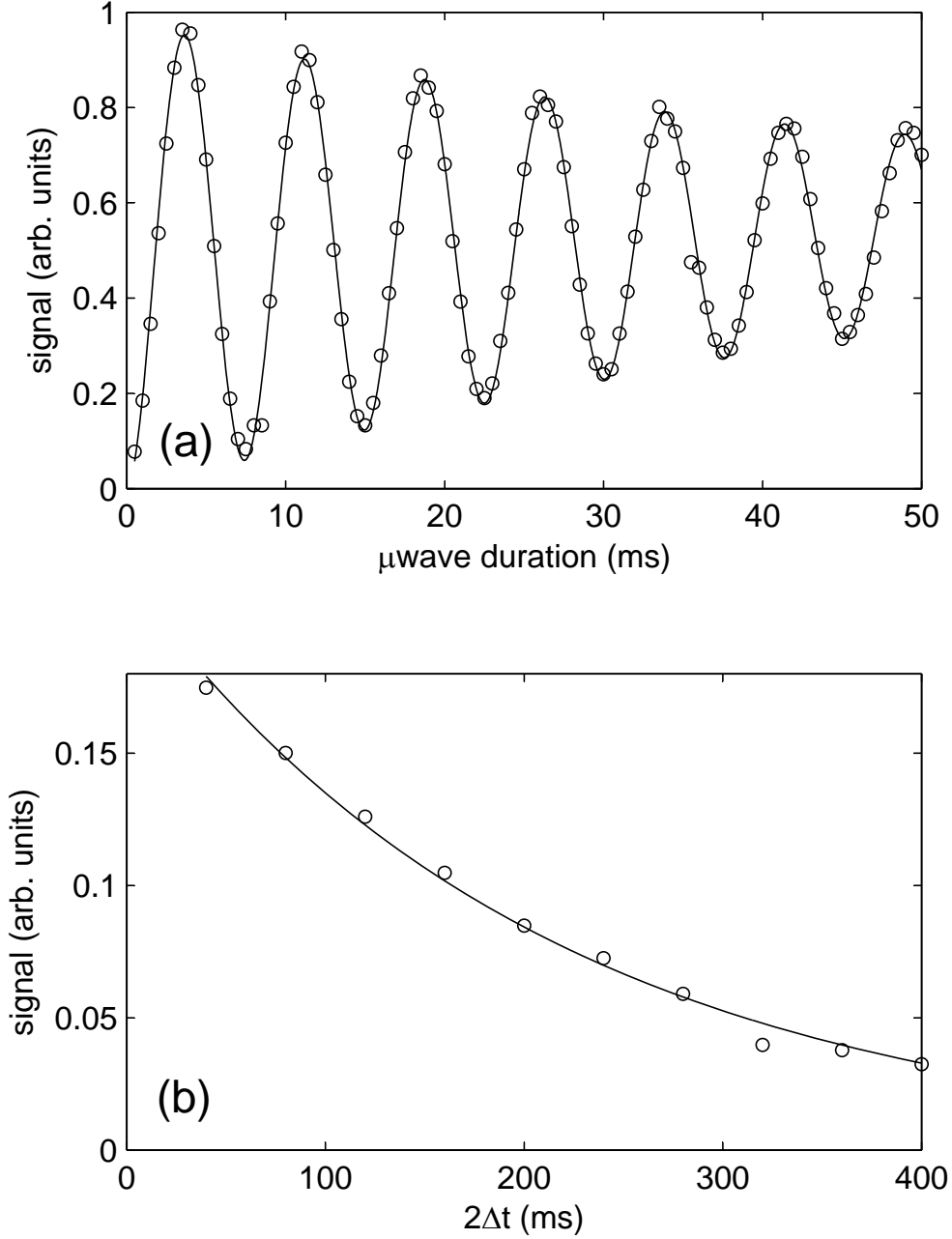
Figure 5.8: (a) Normalized shift of the cavity resonance as a function of the microwave pulse duration. The shift Rabi oscillates with a frequency proportional to the intensity of the microwave radiation. The microwave intensity is reduced significantly from the potential maximum in order to obtain only a few Rabi cycles during the coherence time. Our current fastest Rabi oscillations have a pi-pulse time $\sim 50\,\mu$s, enabling ~ 500 Rabi oscillations during the decay time of the Rabi oscillations. The solid line is a decaying sinusoidal fit with decay time 55 ± 2 ms. (b) Amplitude of Ramsey fringes with a hold time of Δt. The decay constant of the fit (solid curve) is 212 ± 16 ms.

5.6   Unequal trap and probe cavity lengths

We measure the difference in cavity FSR at the trap and probe frequency. If we assume equal FSRs, we observe reflection of the probe sideband when it is tuned with a modulation frequency expected to make it resonant with the cavity. The actual cavity resonance is shifted by an amount $\delta\nu_{\text{offset}} \approx 186\,\text{MHz}$, as shown in Fig. 5.9. This means that this particular cavity resonance has shifted by an amount $\delta\nu = n\nu_{\text{fsr}} + \nu_{\text{offset}}$.

This effect is explained by realizing that the cavity lengths are not equal at the two frequencies. If the effective optical path length were the same at both the trap and probe frequencies, the FSRs at these frequencies would be identical, and frequency doubled resonant 1560 nm light to 780 nm will still be resonant. We require a change in the probe frequency of 186 MHz from the equal FSR case to be in resonance, however, indicating that the cavity length difference between these two is then $\delta L = L_{\text{t}} - L_{\text{p}} = 52\,\text{nm}$ modulo an integer number of half wavelengths ($\sim 390\,\text{nm}$). This length discrepancy is probably due to construction of the quarter-wave stacks used in the fabrication of the mirror coatings not being collocated. The longer effective length for the trap frequencies implies that the trap has to pass through the quarter-wave stacks for the probe beam, which can also explain why a strong trapping beam inside the cavity can cause the strong thermal shift seen in Fig. 5.4.

If we consider briefly the spatial overlap between the probe and trap cavity modes, it becomes clear that the at the center of the cavity (where the atoms are located), the axial profile of the probe and trap modes can take on two possible configurations, shown in Fig. 5.10(a). Every time the probe frequency is changes by 1 FSR, the configuration switches between the two displayed cases. If the FSR were the same at both wavelengths, then the first (second) configuration in Fig. 5.10(a) applies for an even (odd) number of FSR difference between the probe frequency and double the trap frequency. The atoms are always trapped at the maxima of the trap standing wave intensity profile, and the location of the probe maxima can either be poorly overlapped (out of phase registration) or optimally overlapped (in phase registration) with the location of the atoms. While the diagrams in Fig. 5.10(a) are drawn for the
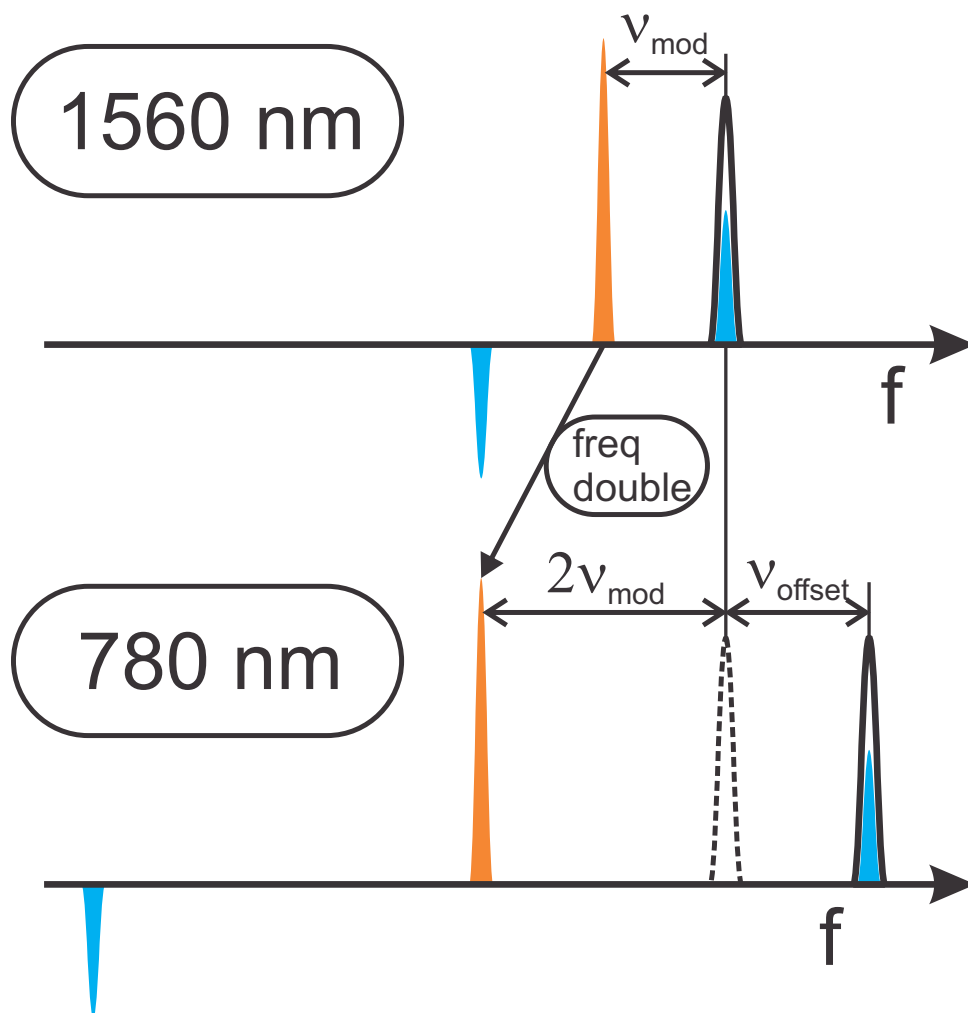
Figure 5.9: Schematic illustrating the effect of unequal cavity lengths at the trap and probe frequencies. A sideband created by modulating the 1560 nm carrier at a frequency ν_{mod} is locked to the cavity, and the carrier is frequency doubled. The new carrier is $2\nu_{\mathrm{mod}}$ from the expected location of the resonance (dashed line), assuming equal cavity lengths. The actual cavity resonance is ν_{offset} further away.
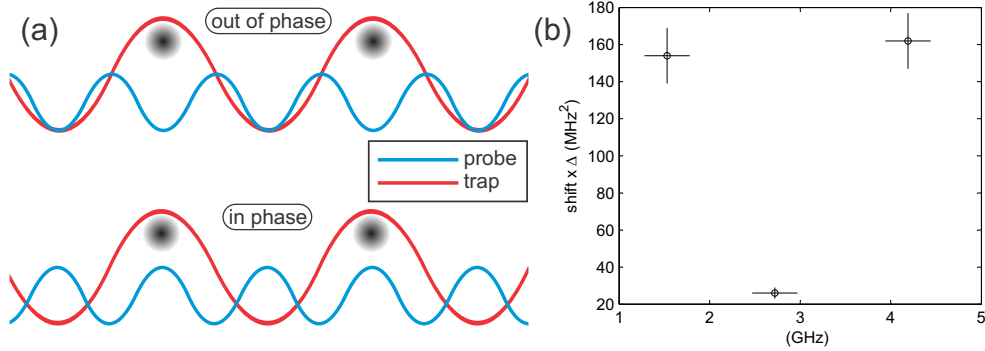
Figure 5.10: (a) The two possible configurations at the center of the cavity. Atoms are trapped at the maxima of the trap beams's intensity profile. The probe beam can either be out of phase (intensity minima at the atom locations) and couple poorly to the atoms, or it can be in phase (intensity maxima at the atom location) and couple optimally to the atoms. It is possible to switch between these configurations by changing the probe frequency by one FSR. (b) Experimental measurement of the cavity shift normalized by the detuning from the atomic resonance. It is clear that for odd FSR the coupling is much stronger than for an even FSR, implying that

case of identical optical path lengths at the trap and probe frequencies, the fact that this is not the case should not affect the overlap if the length difference is due to the difference in mirror coating locations, as this change would be symmetric about the center of the cavity, where the atoms are located.

The data in Fig. 5.10(b) shows the cavity shift for three adjacent cavity resonances. The shift is normalized by detuning Δ from the atomic resonance to account for the Δ^{-1} dependence of the shift. For atoms which are not localized this coupling should be the same. It is important to note that the coupling is stronger for an odd number of FSR frequency displacement, implying that the cavity length difference is in fact $\delta L = 51 + n * \frac{780}{2}$ nm, where n is an odd integer.

Chapter 6

Raman Lasing

6.1 Overview

While assembling and debugging the system described in Chapter 5, we noticed that
sometimes light was emitted from the cavity, even when there was no probe light.
This emitted light was due to the continuously loading MOT, and the emitted spatial
mode was strongly dependent on the cavity length. After some initial head scratching,
we realized we had the beginnings of a very tunable Raman laser system on our hands,
and we took a scientific detour to try and understand this system and stabilize its
operations by adding a Raman pump beam.

We were able to demonstrate a Raman laser using cold ^{87}Rb atoms as the gain
medium in a high finesse optical cavity. We observed robust continuous wave lasing
in the atypical regime where single atoms can considerably affect the cavity field.
Consequently, we discover unusual lasing threshold behavior in the system causing
jumps in lasing power, and propose a model to explain the effect. We also measure
the linewidth between two transverse cavity modes lasing simultaneously (intermode
laser linewidth), and observe values as low as 80 Hz. The tunable gain properties of
this laser suggest multiple directions for future research.
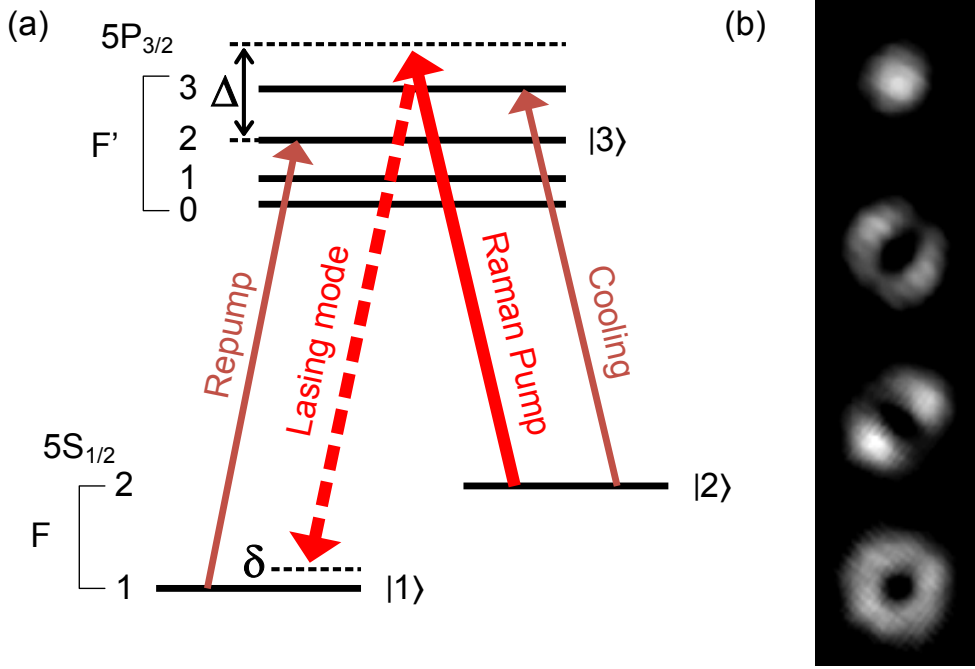
Figure 6.1: (a) Energy level diagram of ^{87}Rb including relevant laser frequencies for the Raman process, as well as the cooling and repump light frequencies associated with the magneto-optical trap. (b) Sample CCD images showing relevant spatial modes of the laser. Top to bottom: TEM$_{00}$, TEM$_{01}$, TEM$_{10}$, TEM$_{01}$+TEM$_{10}$, resp.

6.2   Experimental Setup

Atoms loaded into a MOT at the center of the dual-wavelength optical cavity (described in Chapter 5) undergo a two-photon Raman transition driven by a frequency tunable pump laser which excites the atoms from the $|F = 2\rangle$ hyperfine ground state to an intermediate virtual state detuned from the $|F = 2\rangle \rightarrow |F' = 2\rangle$ transition by the single photon detuning Δ. An allowed cavity resonance from this intermediate state down to the $|F = 1\rangle$ hyperfine ground state allows completion of the two-photon process. The atoms are driven back to $|F = 2\rangle$ by the repump light (resonant with the $|F = 1\rangle \rightarrow |F' = 2\rangle$ transition) associated with the MOT, allowing continuous laser output. This is effectively a three level system where we refer to the $|F = 1\rangle$, $|F = 2\rangle$ and $|F' = 2\rangle$ states as $|1\rangle$, $|2\rangle$ and $|3\rangle$, resp. The relevant atomic energy levels and laser frequencies are shown in Fig. 6.1(a).

The cavity parameters are summarized in Table 5.1. For the single-photon de-tunings Δ used in this experiment the resulting atom-induced cavity resonance shifts are $\delta\nu = g^2/\Delta \sim$ 10-20 Hz/atom. The spacing between nearest sets of transverse modes is $\Delta\nu_{\mathrm{tms}} = 75$ MHz for our parameters, much greater than the gain bandwidth of ~ 3MHz (γ_{21} below). This allows only one set of transverse modes (those whose transverse mode indices add to the same total) to be resonant at a time. In other words, $\mathrm{TEM}_{1,0}$, $\mathrm{TEM}_{0,1}$ can resonate simultaneously, but TEM modes whose mode indices do not add up to one can not, as shown in Fig. 6.1(b). We can excite different spatial modes of the cavity by tuning the frequency of the Raman pump to select the cavity mode whose frequency satisfies the overall two-photon resonance condition.

A schematic of the experimental setup is shown in Fig. 6.2. The input laser light at 1560 nm is split by a polarizing beam splitter, with one path used to stabilize the frequency of the light to the cavity using a Pound-Drever-Hall (PDH) method [38], to better than a kilohertz. The majority of the light follows the other path, where it is frequency doubled in a periodically poled lithium niobate (PPLN) waveguide crystal to generate the 780 nm light used for the Raman pump laser and the local oscillator beam. This way of generating the 780 nm light ensures that the Raman transition is insensitive to cavity length drifts. A double-passed acousto-optical modulator allows for tuning of the pump beam frequency, enabling fast switching between spatial modes. We note that the linewidth of the Raman pump does not need to be narrow, as we observe lasing equally well with a MHz linewidth pump.

By tuning the pump frequency and cavity lengths appropriately, we can force arbitrary spatial modes to lase, up to a certain beam size limited by the physical extent of the cavity mirrors. One example, shown in Fig. 6.3, is a $\mathrm{TEM}_{17,32}$ mode, but even higher order modes are possible.

Light emitted from one cavity mirror is split by a polarizing beam splitter. One path steers the beam incident on a CCD camera to image the spatial mode intensity profile, where we can image the lasing modes. The other path is incident on a single mode fiber connected to a Perkin-Elmer ARQH-13 avalanche photodiode single photon counting module (SPCM). Short pulses from the SPCM, corresponding to a photon detection, are integrated, and a time trace is measured on an oscilloscope.
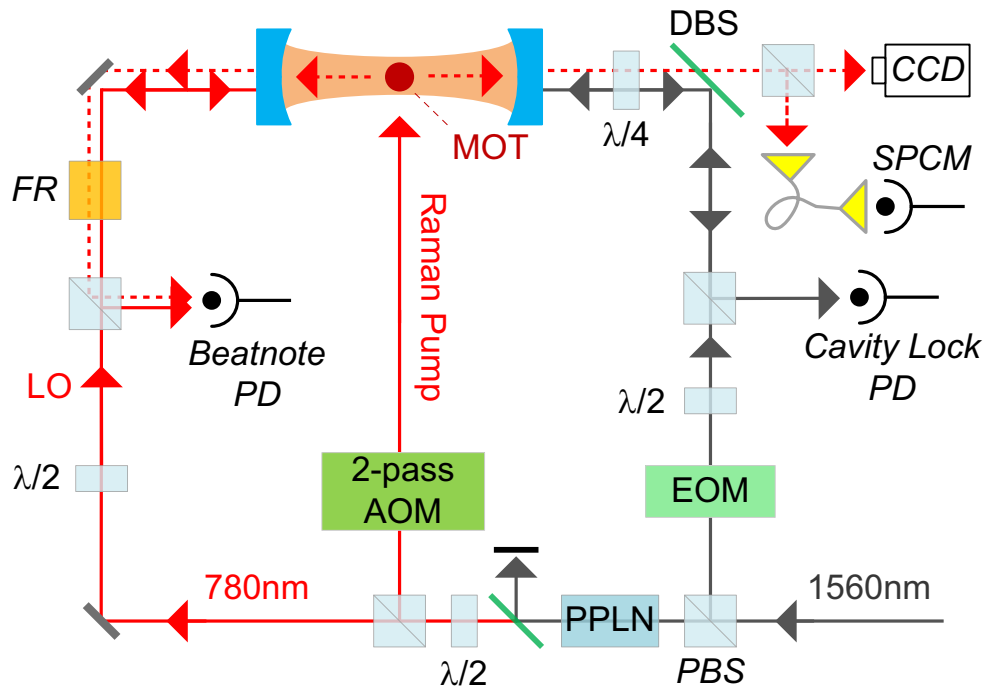
Figure 6.2: Schematic of the experiment. LO = local oscillator, AOM = acousto-optical modulator, EOM = electro-optical modulator, FR = Faraday Rotator, PBS = Polarizing Beam Splitter, DBS = dichroic beam splitter, $\lambda/2$ = half- wave plate, $\lambda/4$ = quarter-wave plate.
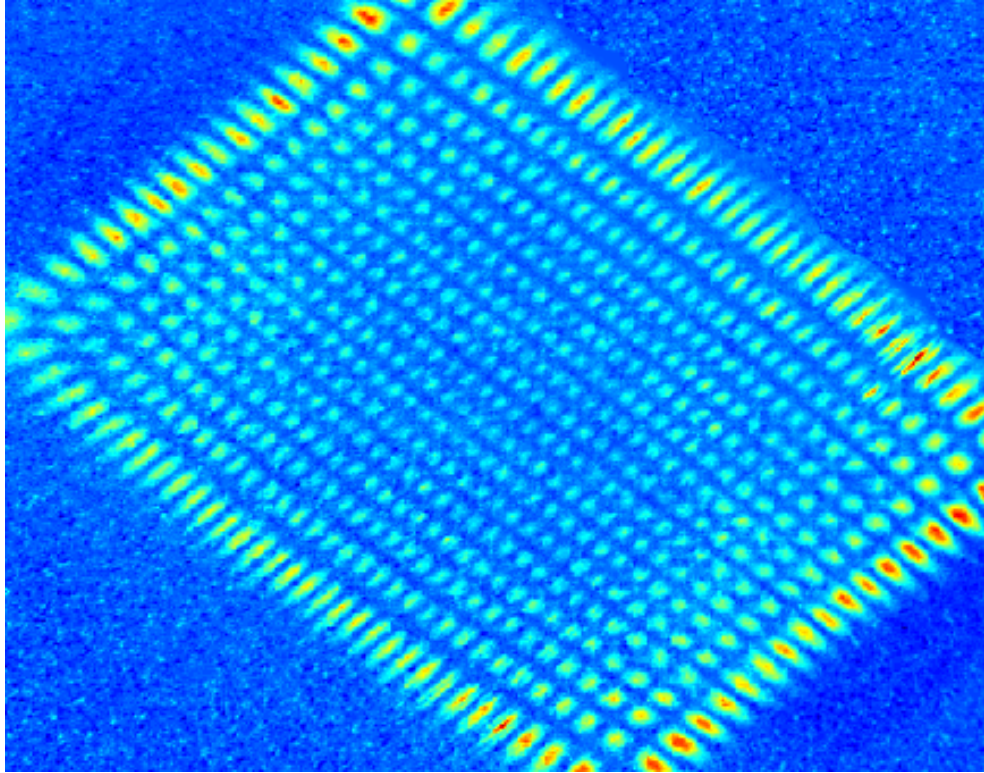
Figure 6.3: CCD image of a typical accessible high-order ($TEM_{17,32}$) transverse lasing mode. Even higher order modes are accessible, but the exact number of nodes begins to get more difficult to quantify with the current imaging setup due to the large spatial extent of the mode extending beyond the edges of the CCD sensor.

Light emitted from the other cavity mirror is combined with a local oscillator beam and incident on a fast photodiode. The resulting beat note gives us the laser's optical frequency relative to the known local oscillator frequency.

6.3   Results

The cavity gain can be expected to be proportional to both the effective atom number N_{eff} and the pump intensity I_{p}. We demonstrate a lasing threshold by varying the gain, either by changing the effective atom number in the cavity mode, or by changing the intensity in the pump beam. Allowing the MOT to load while keeping the pump intensity constant results in a visible threshold after which lasing occurs. The effective atom number N_{eff} in the cavity mode is related to the actual atom number by a geometrical overlap factor between the MOT cloud and the cavity mode. Fig. 6.4(a) shows a parametric plot of the measured $N_{\text{eff}}$ and lasing power for the TEM_{00} mode. Equivalently, by increasing the pump beam intensity I_{p} while keeping the atom number constant results in a visible threshold in the pump intensity, as seen in Fig. 6.4(b).

We extract the laser's intermode linewidth, which is insensitive to cavity length fluctuations, from the beat note between two lasing modes. Specifically, by tuning the pump frequency we make the TEM_{01} and TEM_{10} modes lase simultaneously [resulting in the "donut mode" seen in Fig. 6.2(b)], and partially couple these modes into a single-mode fiber leading to the SPCM. These two modes are non-degenerate (due to geometrical imperfections in the cavity mirrors) by approximately 515 kHz, a value well within the gain bandwidth. A frequency spectrum extracted from a particularly stable 4 ms window of the recorded time-domain signal is shown in the inset of Fig. 6.5. A Lorentzian fit indicates a HWHM of 160 Hz, corresponding to an instantaneous intermode linewidth of 80 Hz for the convolution of two identical Lorentzian lineshapes. Similarly, a minimum average instantaneous intermode HWHM linewidth of 224 Hz is obtained by averaging centered spectra derived from consecutive 2 ms windows (Fig. 6.5). Note that the purpose of the centering procedure is to eliminate broadening due to central lasing frequency drift. The fact that a good Lorentzian
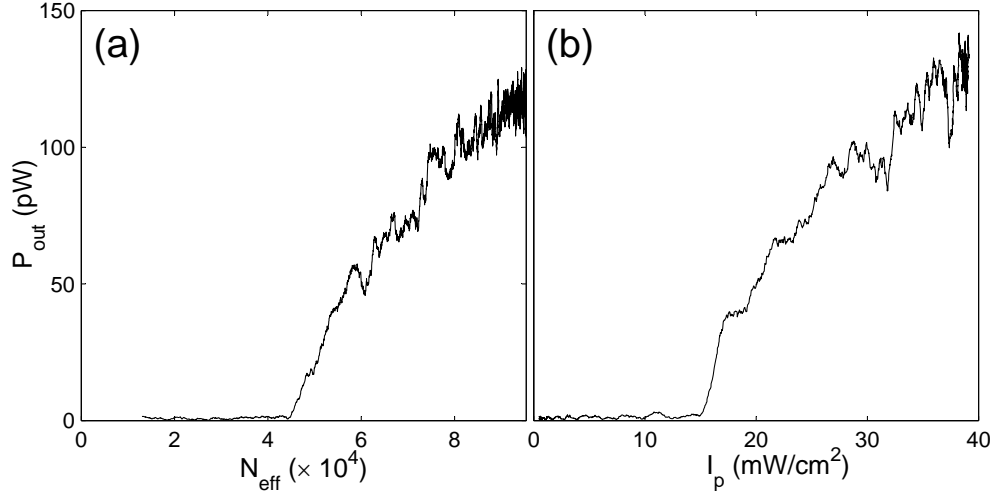
Figure 6.4: (a) Cavity output power as a function of N_{eff}. (b) Cavity output power as a function of pump intensity I_{p}. In both cases, threshold behavior is clearly visible, indicating the point at which losses at the cavity mirrors are overcome by the gain medium.

fit to the peak overshoots the tails is an indication of excess low frequency noise on the instantaneous frequency. It is known that the quantum limited linewidth could in principle be inferred from the Lorentzian tails of a lineshape at high frequencies [61]. In our case, although small side lobes and a high baseline partly obscure the tails of the distribution, a Lorentzian fit to these tails still represent an upper bound on the quantum limited linewidth of the laser. This procedure yields an 86 Hz HWHM linewidth, and is insensitive to the window size used. Note that this fit necessarily overshoots the peak. Comparison with theory is subtle, but as a reference the Schawlow-Townes linewidth limit (without taking into account amplitude-phase noise coupling, or incomplete population inversion) is 0.25 Hz.

The 1560 nm lattice is too weak to confine the atoms, and due to the atomic thermal motion inside of the MOT, the atoms in the lasing modes are expected to get completely replenished within ~ 1 ms. Thus, the difference in the atom numbers seen by the TEM_{01} and TEM_{10} modes could in principle fluctuate significantly in the course of the spectral measurements. As a reference, the shot noise level of the effective atom number in each mode is ~ 150 atoms. Using the measured generic atom
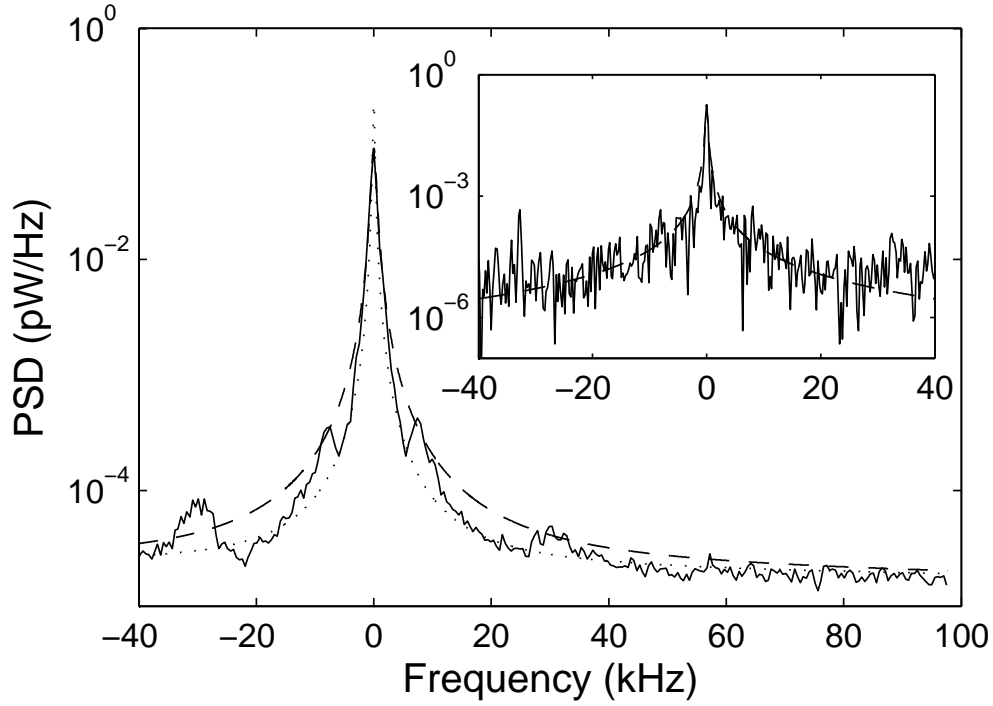
Figure 6.5: Measured beat note power spectral density between the TEM_{01} and TEM_{10} modes at 25 mW/cm² pump intensity with $N_{eff} = 9 \times 10^4$, showing an average of 100 spectra (2 ms windows) that are centered before averaging. Dashed line: Lorentzian fit with HWHM of 448 Hz, Dotted line: Lorentzian fit to the tails with HWHM of 172 Hz. Inset: A single realization of the spectrum for a particularly stable 4 ms window; dashed line: Lorentzian fit with HWHM of 160 Hz.
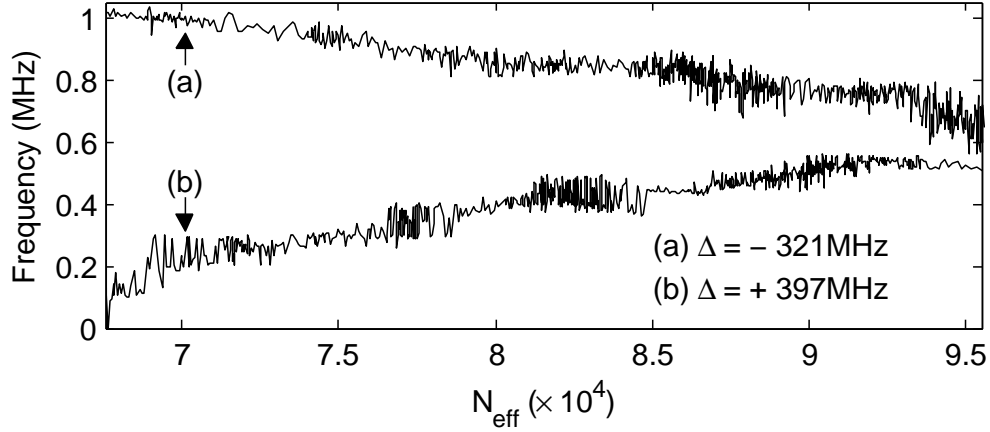
Figure 6.6: TEM$_{00}$ lasing mode frequency shift as a function of N_{eff} for (a) red and (b) blue detuned light. Opposite slopes are due to the positive and negative susceptibilities associated with the red and blue detuned configurations respectively. Relative positioning of the two curves is arbitrary.

number dependence of the absolute lasing frequency [Fig. 6.6], it can be inferred that only about 20 atoms (well below shot noise level $\sim \sqrt{N_{\text{eff}}}$) of a fluctuation could account for the observed 224 Hz intermode linewidth. Similarly, about 7 atoms of fluctuation accounts for the observed instantaneous intermode linewidth of 80 Hz.

The threshold behavior and linewidth narrowing with respect to the cavity HWHM linewidth at 780 nm κ_{p} shown in Figs. 6.4 and 6.5 constitute the generic signatures of a laser. However, the rather large cooperativity parameter in combination with the relatively narrow Raman gain bandwidth leads to further interesting nonlinear phenomena in lasing behavior. For certain parameters, as the gain is increased, the onset of lasing occurs with an abrupt jump in lasing power, defying traditional threshold behavior. Fig. 6.7(a) shows lasing power as a function of Raman pump intensity for slightly differing pump frequencies, all with positive single-photon detuning Δ. The different pump frequencies correspond to different two-photon detunings δ shown in Fig. 6.2(a). The jumping behavior in lasing power is observed for positive δ. As the pump intensity is cycled up and down, the onset and extinction of lasing take place at different pump intensities. When δ is negative, this behavior disappears. A simple mechanism based on the AC Stark shift experienced by the F=1 state qualitatively captures this effect. For positive Δ, the onset of any lasing will shift the F=1 state up,

in turn decreasing δ if it was positive initially, hence increasing the gain which further increases the lasing and the Stark shift until equilibrium is reached. For negative δ the Stark shift will decrease the gain, resisting the increase in lasing.

The proposed mechanism can be modeled with a three level system [levels $|1\rangle$, $|2\rangle$, $|3\rangle$ in Fig. 6.2(a)], disregarding the details pertaining to the repump and cooling beams, and taking their effects into account phenomenologically by adding a population transfer rate Γ_{12} from $|1\rangle$ to $|2\rangle$ and additional decoherence rates. The gain associated with an ensemble of atoms can be calculated by solving for the steady state values of the density matrix elements in a standard fashion [62]. The quantity of interest is the density matrix element ρ_{31} giving the atomic polarization at the lasing transition frequency ω_l, which can be expressed as a sum of one-photon and two-photon terms:

$$
\begin{aligned}
\rho_{31}^{(1\mathrm{ph})} &= \frac{1}{2\left(\Delta + i\gamma_{31}\right)}\left(\rho_{33} - \rho_{11}\right) \\
\rho_{31}^{(2\mathrm{ph})} &= \frac{\left|\Omega_p\right|^2}{4\Delta^2} \frac{1}{2\left(-\delta' + i\gamma_{21}\right)}\left(\rho_{22} - \rho_{11}\right) \\
\rho_{31} &= \left[\rho_{31}^{(1\mathrm{ph})} + \rho_{31}^{(2\mathrm{ph})}\right]\Omega_c e^{i\omega_l t}
\end{aligned}
\tag{6.1}
$$

Here $\left(\rho_{33} - \rho_{11}\right)$ and $\left(\rho_{22} - \rho_{11}\right)$ are population differences, γ_{31} and γ_{21} are coherence decay rates, Ω_p and Ω_c are the Rabi frequencies associated with the pump and cavity lasing transitions, $\delta' = \delta - \left(\delta_{ac1} - \delta_{ac2}\right)$ is the effective two-photon detuning with $\delta_{ac1} = \frac{\left|\Omega_c\right|^2}{4\Delta}$, $\delta_{ac2} = \frac{\left|\Omega_p\right|^2}{4\Delta}$ being the AC Stark shifts, and $\left(\rho_{22} - \rho_{11}\right) = 1/\left(1 + s\right)$ with $s = \frac{\gamma_{21}}{\Gamma_{12}}\frac{|\Omega|^2}{\delta'^2 + \gamma_{21}^2}$ given in terms of the two-photon Rabi frequency $\Omega = -\frac{\Omega_p^*\Omega_c}{2\Delta}$. In solving the density matrix equations we utilize simplifying assumptions based on $\Delta \gg \gamma_{ij}, \Gamma_{ij}, \delta$. The imaginary part of the expression in square brackets is proportional to the gain/loss, the real part to the phase shift imparted [62].

At this stage, a self-consistent solution to the lasing intensity can be found by equating the single pass gain to the mirror transmission. For the relevant parameter space, $\rho_{31}^{(2\mathrm{ph})}$ brings gain while $\rho_{31}^{(1\mathrm{ph})}$ brings absorption but can be ignored. The resulting equation has the form $AI_p^{\mathrm{norm}} = \left(1 + \delta'^2/\gamma_{21}^2\right)\left(1 + s\right)$, with δ' and s expressed in terms of the normalized pump and intra-cavity intensity parameters
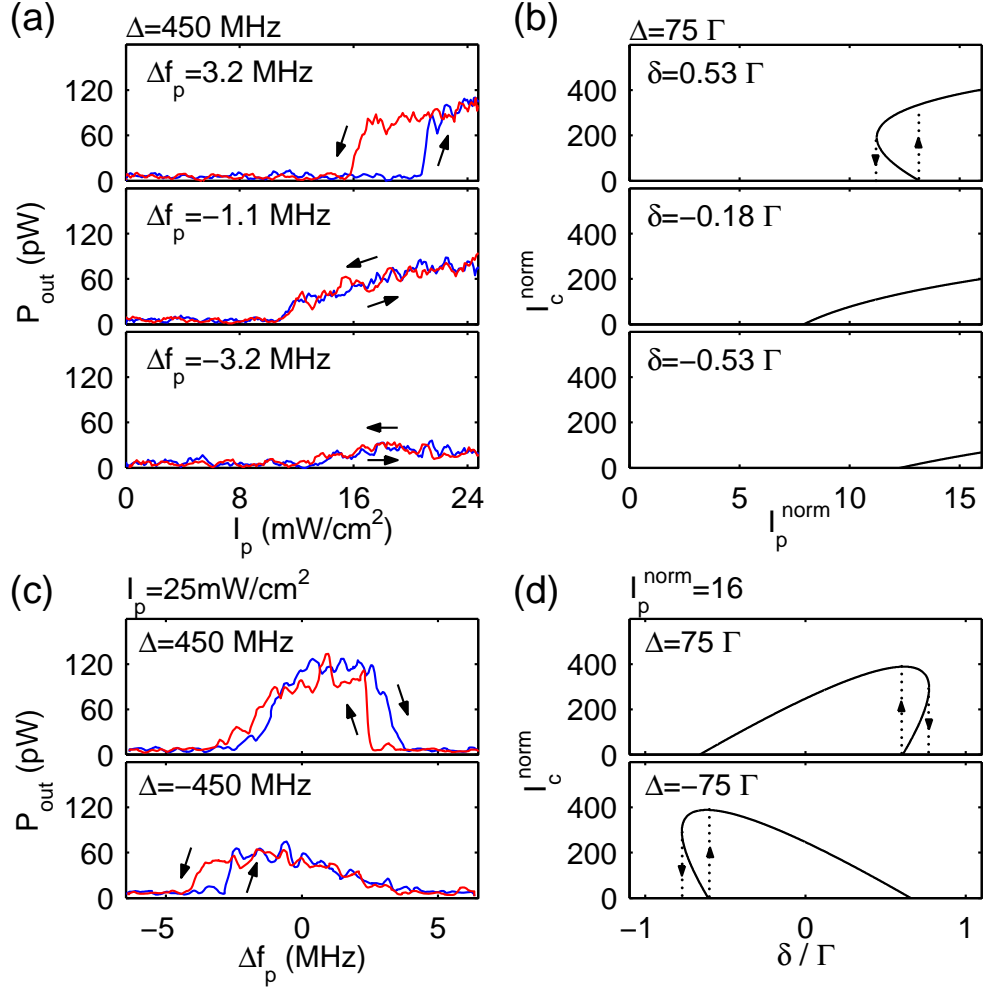
Figure 6.7: (a) Cavity output power as a function of pump intensity for different values of the relative pump frequency Δf_p. $\Delta f_p = 0$ is chosen to correspond to the experimentally inferred $\delta = 0$ condition. (b) The corresponding calculated steady-state intra-cavity intensity. The arrows indicate the expected jumps in the lasing intensity depending on the sweep direction. (c) Cavity output power as a function of Δf_p for opposite single photon detunings $\pm\Delta$. (d) Calculated steady-state intra-cavity intensity. Parameters for the calculated curves are $A = 0.135$, $\gamma_{21} = 0.625\Gamma$, $\Gamma_{12} = 0.1\Gamma$.

$I_p^{\mathrm{norm}} = 2 \left|\Omega_p\right|^2 / \Gamma^2$ and $I_c^{\mathrm{norm}} = 2 \left|\Omega_c\right|^2 / \Gamma^2$. Here $A \propto N_{\mathrm{eff}} C / \Delta^2$ is a constant depending on various system parameters, and $\Gamma = \Gamma_{31} + \Gamma_{32}$. The results, for parameters chosen to represent the experiment, are shown in Fig. 6.7(b)&(d), indicating a bi-stable behavior for certain parameters, closely mimicking the experimental results. Shown in Fig. 6.7(c) are experimental results of the lasing profile as a function of pump frequency, conforming to the theoretical model. Additional measurements analogous to the ones in Fig. 6.7(a), but with $\Delta = -450$ MHz indicate that, in this case the roles of positive and negative δ are swapped, as expected.

Chapter 7

Conclusion and Future Work

7.1 Conclusion

The work described in this Dissertation investigates some of the important capabilities of experiments using optical cavities and QND measurements to create novel collective states of atomic ensembles. Putting many atoms in high-finesse cavities is not trivial, and we had to learn as we went, discovering problems we had never anticipated when we started. We have eliminated many of the limiting factors along the way.

The common theme throughout this Dissertation is the continual quest for noise reduction and detection sensitivity. The demonstration of a large collective cooperativity system with the potential to produce significantly squeezed states using QND techniques [63] set the stage for attempting to generate squeezed states of the atomic pseudo-spin. By coupling large degrees of squeezing with large atom numbers, the potential is there for improved absolute performance for existing cold atom clocks and interferometers. We were able to demonstrate significant anti-squeezing, but determining any squeezing was out of reach due to residual motion of the atoms in the cavity mode [64].

Our solution to this problem, the 1560 nm dipole trap, has several key features. It confines the atoms at the antinodes of the electric field, preventing any axial atomic motion. Also, because the trap wavelength is twice the wavelength of the probe beam,

all the confined atoms see the same probe beam intensity, and therefore the atom-light coupling is the same for all the atoms. This property of our system will reduce the ambiguity of what it means to truly be a squeezed state that is inherent in most experiments that seek to demonstrate squeezing.

Our Raman laser experiment is a great example of two principles: (1) If you have a good tool, it will have uses you never expected; and (2) A good tool will do its job wether you want it to or not. We first discovered that our cavity was emitting light when we first installed the single photon counter to measure the transmission, and found that we had light even when there was no probe beam. After some initial head scratching we decided that we were going to pursue this, and our initial thoughts on why we were seeing this light proved correct, and we demonstrated a high-finesse cavity Raman laser using cold atoms as the gain medium. We observed an emerging nonlinear lasing threshold behavior, the features of which we were able to explain with a simple model [65]. Our Raman laser has intermode linewidths as low as 80 Hz between two simultaneously lasing modes, which is of importance for applications like potential ring laser gyroscopes [66] utilizing exotic gain media [67] for rotation sensing.

7.2   Future Work

The main obstacle preventing the demonstration of significant squeezing in this experiment is cavity vibrations on time scales over which the experiment is performed. The current experimental protocol is unable to distinguish between effective optical path length fluctuations due to changes in the atomic populations, and those due to fluctuations in the cavity length due to mechanical vibrations of the cavity tubes.

We are currently implementing an additional modulation frequency on the probe beam in the detection scheme [68] which will allow us to distinguish between the two sources of fluctuations and eliminate the cavity length fluctuations, as shown in Fig. 7.1. The current probe beam sideband will remain and detect fluctuations from both sources, while a second sideband, also resonant with the cavity but far detuned from the atomic resonance, will be sensitive to the same cavity length fluctuations
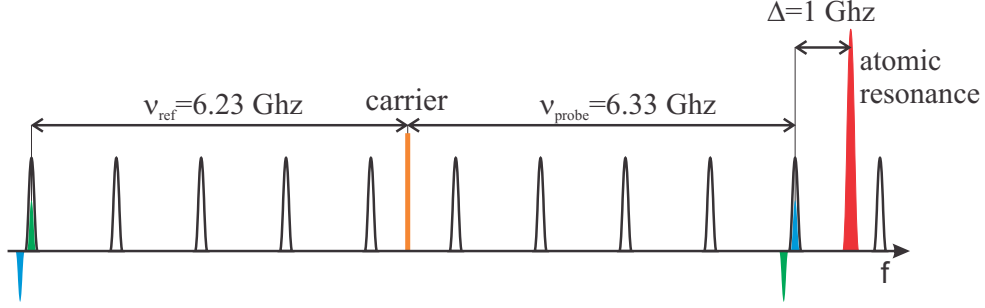
Figure 7.1: Schematic of the probe and reference frequencies in the proposed two-frequency modulation scheme. The probe beam (blue) is resonant with the cavity at a relatively small detuning Δ from the atomic resonance. The reference beam (green) is resonant with the cavity at a much larger detuning, making it essentially insensitive to the atoms. By taking the difference in output signals generated by these two beams we can make the output sensitive only to the atomic state.

but insensitive to the collective atomic state.

With this new detection mechanism in place we should be able to demonstrate a significantly (≥ 10 dB of uncertainty reduction in the variance) squeezed state. A proof-of-principle atom interferometry experiment can also be done, considering the vacuum chamber is designed to accommodate drop times of approximately 100 ms. The demonstrated trap and coherence decay times in the dipole trap are also long enough to make this an extremely flexible system when looking to the future.

For the Raman laser we can identify a few possible future directions. The effects of normal and anomalous dispersion [30] can be investigated for reduced and enhanced, respectively, sensitivity of lasing frequency to disturbances. The proposals for steady-state superradiance [32] can be investigated by tuning the relative strengths of the two-photon Rabi frequency and the repumping rate. Measurements of intra-cavity atom numbers can be pursued by looking at atom number-intensity correlations. The sharp transitions observed when lasing starts can be investigated from a possible sensor application perspective, e.g., for measuring disturbances causing atomic level shifts, with the example of superconducting transition edge sensors [69] in mind. Finally, the nonlinearities in Raman lasing can be further studied for possible quantum noise reduction of the intensity fluctuations to below shot noise [70].

Appendix A

Modeling the anti-squeezing

For a Hamiltonian of the form

$$H = \hbar \Omega a^\dagger a J_z, \tag{A.1}$$

where $a^\dagger$ and a are the photon creation and annihilation operators, resp., and J_z is the atomic number difference operator. We can model the response of the coupled atom-cavity system assuming the photons are initially in a coherent state $|\alpha\rangle$, and the atoms are initially pointed along $\hat{J}_x$. The combined atom-light state can then be written as:

$$
\begin{aligned}
|\Psi(0)\rangle &= |J_x = J; \alpha\rangle \\
&= \sum_{k=0}^{2J} 2^{-J} \binom{2J}{k}^{\frac{1}{2}} |J_z = k - J; \alpha\rangle
\end{aligned}
\tag{A.2}
$$

Unless stated otherwise the notation $|A; B\rangle$ will be used to denote the tensor product $|J_z = A\rangle \otimes |B\rangle$, where the first term is the atomic part of the wave function written as a J_z eigenstate, and the second term is the coherent photon state $|B\rangle$.

Time evolving Eq. A.2 gives:

$$
\begin{aligned}
|\Psi(t)\rangle &= e^{-i\frac{H}{\hbar}t} |\Psi(0)\rangle \\
&= \sum_{k=0}^{2J} 2^{-J} \binom{2J}{k}^{\frac{1}{2}} |k - J; \alpha e^{-i(k-J)\Omega t}\rangle
\end{aligned}
\tag{A.3}
$$

77

where the atom and photon parts of the wave function are now no longer separable. From Eq. A.3 it is clear that $|\Psi(t)\rangle$ has an atomic state dependent phase shift on the state of the light. However, if we were to calculate the expectation value $\langle \Delta J_z^2 \rangle$ we would see that it is unchanged, indicating that this atom-photon interaction by itself is not sufficient to generate a squeezed state. On the other hand, if we were to measure the phase of the light field, and project this out, we would obtain the atomic state

$$
\begin{aligned}
|\Psi_{\text{at}}(t)\rangle &= C^{-1} \langle \alpha e^{i\theta} | \Psi(t) \rangle \\
&= C^{-1} \sum_{k=0}^{2J} 2^{-J} \binom{2J}{k}^{\frac{1}{2}} \exp\left[-|\alpha|^2 \left(1 - e^{-i(k-J)\Omega t + \theta} \right) \right] |k - J\rangle. \quad \text{(A.4)}
\end{aligned}
$$

The renormalization constant C can be found by requiring that $\langle \Psi_{\text{at}}(t) | \Psi_{\text{at}}(t) \rangle = 1$ and is given by

$$
\begin{aligned}
|C|^2 &= \sum_{k=0}^{2J} 2^{-2J} \binom{2J}{k} e^{-4|\alpha|^2 \sin^2\left[\frac{\Omega t}{2}(k-J)+\frac{\theta}{2}\right]} \\
&\approx \int_{-\infty}^{\infty} \frac{1}{\sqrt{\pi J}} e^{-\frac{(k-J)^2}{J}} e^{-|\alpha|^2 \Omega^2 t^2 \left[k-\left(J+\frac{\theta}{\Omega t}\right)\right]^2} \\
&= \left(1 + |\alpha|^2 J \Omega^2 t^2 \right)^{-\frac{1}{2}} e^{-\frac{|\alpha|^2 \theta^2}{1+|\alpha|^2 J \Omega^2 t^2}} \quad \text{(A.5)}
\end{aligned}
$$

where the approximation holds as long as $J \gg 1$.

By the same method we can then calculate $\langle J_z \rangle$ and $\langle J_z^2 \rangle$ to be:

$$
\langle J_z \rangle = -\theta \frac{J |\alpha|^2 \Omega t}{1 + J |\alpha|^2 \Omega^2 t^2} \quad \text{(A.6)}
$$

$$
\langle J_z^2 \rangle = \langle J_z \rangle^2 + \frac{J}{2} \left(1 + J |\alpha|^2 \Omega^2 t^2 \right)^{-1}
$$

$$
\langle \Delta J_z^2 \rangle = \langle J_z^2 \rangle - \langle J_z \rangle^2 = \frac{J}{2} \left(1 + J |\alpha|^2 \Omega^2 t^2 \right)^{-1} \quad \text{(A.7)}
$$

Note that expectation value in Eq. A.6 is offset from zero by an amount proportional to the measured phase of the coherent light field. Without this conditional offset $\langle J_z \rangle$ would be zero. The uncertainty in J_z given by Eq. A.7 is independent from

the measured phase. In other words, no matter what the measurement result is, the state will have the same deterministic uncertainty properties. Only the value of $\langle J_z \rangle$ is dependent on the measurement outcome. As expected, at $t = 0$ the uncertainty starts out with the normal coherent atomic state value of $J/2$. It deterministically decreases from there, indicating number squeezing.

According to the Heisenberg uncertainty principle $\sqrt{\langle \Delta J_y^2 \rangle \langle \Delta J_z^2 \rangle} \geqslant \frac{1}{2} \left| \langle J_y \rangle \right| = J/2$, or:

$$\langle \Delta J_y^2 \rangle \geqslant \frac{J}{2} \left(1 + J|\alpha|^2 \Omega^2 t^2 \right) \tag{A.8}$$

which is a measure of the anti-squeezing. It is a fairly simple procedure to rotate the Bloch vector around any axis, i.e. using microwave pulses, and so the generated number-squeezing can be turned into squeezing of the desired quadrature of the pseudo-spin.

The equations presented here are only valid for short times, i.e. times short compared to the photon lifetime inside the cavity. For longer times we break the evolution up into many shorter intervals of duration τ, during which the system is allowed to evolve in an unperturbed manner. The repeated projections incoherently add, causing the variances to evolve linearly, as opposed to quadratically, in time. These effects combine to result in:

$$\langle \Delta J_z^2 \rangle = \frac{J}{2} \left[1 + J \left(\int_0^\tau |\alpha(t')|^2 \kappa \, \mathrm{d}t' \right) \Omega^2 \frac{\tau t}{\sqrt{2}} \right]^{-1} \tag{A.9}$$

where κ is the cavity lifetime. This result is in good agreement with the more general and comprehensive theory presented in [57].

Appendix B

The linearly swept dispersive signal

B.1 Motivation

The dispersive signals which we detect in many of the sections in this paper are obtained by linearly sweeping the modulation frequency across the cavity resonance, and recording the resulting dispersive curve. If the sweep rate R is slow enough, meaning that the optical frequency changes by less than a cavity linewidth per cavity response time –or $R \ll \kappa/\tau = \kappa^2$– the measured transmission (dispersion) curve is the real (imaginary) part of the complex Lorentzian lineshape $L(\omega)$ defined as

$$L(\omega - \omega_c) = \frac{1}{1 + i\frac{\omega - \omega_c}{\kappa}} \tag{B.1}$$

where $L(\omega)$ is normalized so that $\mathrm{Re}\left[L(\omega)\right] = 1$ when $\omega = \omega_c$. However, for $R \gtrsim \kappa^2$, light that enters the cavity does not exit until the driving field has changed significantly in frequency. The interference between the different frequency components of the reflected light can have a strong effect on the detected dispersive signal. Our experiment relies heavily on accurately detecting the location of the dispersive signal zero, and we therefore benefit from an accurate and computationally fast fit function. There exists an easily computable solution for the special case where the frequency sweep is linear in time.

B.2   Procedure

Start by assuming $E(t) = E_0 e^{i\phi(t)}$, where E_0 and ϕ are the amplitude and phase of the electric field, respectively. The optical frequency is being changed by applying a linear sweep at a rate R, leading to a laser frequency $\omega_L(t) = \omega_0 + Rt$, where ω_0 is the unperturbed frequency of the laser. The phase then becomes $\phi(t) = \int \omega_L(t)\, dt = \omega_0 t + \frac{R}{2} t^2$. We need to compute the spectral profile of this electric field, and so we take the Fourier transform:

$$
\begin{aligned}
\tilde{E}(w) &= \int_{-\infty}^{\infty} E(t) e^{-iwt}\, dt \\
&= \sqrt{\frac{2\pi i}{R}} E_0 e^{-i\frac{(\omega - \omega_0)^2}{2R}}
\end{aligned}
\tag{B.2}
$$

The cavity has a transmission lineshape given by Eq. B.1, which multiplies the incident field given by Eq. B.2 to get the transmitted frequency-domain signal. The time-domain signal of the transmitted light is then given by the inverse Fourier transform of this quantity:

$$
\begin{aligned}
E_T(t) &= \int_{-\infty}^{\infty} \tilde{E}(\omega) L(\omega - \omega_c) e^{i\omega t}\, dt \\
&= E(t) \sqrt{\frac{\pi i}{2R}} \kappa w\left[-\sqrt{\frac{iR}{2}}\left(t - \frac{\omega_c - \omega_0 + i\kappa}{R} \right) \right]
\end{aligned}
\tag{B.3}
$$

Here, w is the complex error function, also known as the Faddeeva function, given by $w(x) = e^{-x^2}\left[1 - \mathrm{erf}(-ix) \right]$.

From Eq. B.3 we see that the time-dependent cavity transfer function is given by:

$$
T(t) = \frac{E_T(t)}{E(t)} = \sqrt{\frac{\pi i}{2R}} \kappa w\left[-\sqrt{\frac{iR}{2}}\left(t - \frac{\omega_c - \omega_0 + i\kappa}{R} \right) \right]
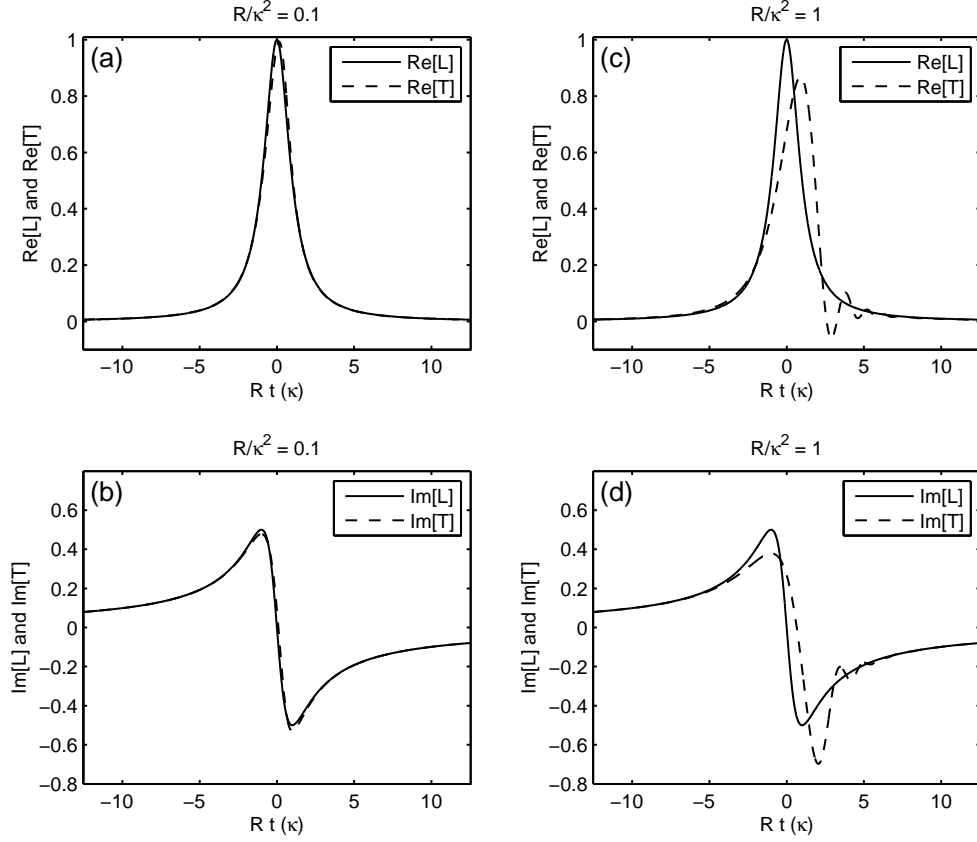\tag{B.4}
$$

.

Figure B.1: (a) and (b): The real and imaginary parts of the cavity lineshape L and cavity transfer function T when $R \ll \kappa^2$. (c) and (d): The real and imaginary parts of the cavity lineshape L and cavity transfer function T when $R = \kappa^2$. It is assumed that $\omega_c = \omega_0$ for all plots.

B.3 Correspondence with Experiment

The real (imaginary) part of Eq. B.4 corresponds to the transmission (dispersion) lineshape, as is shown in Fig. B.1. In the case when $R \ll \kappa^2$ the real and imaginary parts of $T(t)$ look very similar to the those of $L(\omega/R)$, as expected. However, when $R \gtrsim \kappa^2$, T starts to change shape compared to L because the fast sweep rate causes the light exiting the cavity to differ substantially in frequency from the incident light.

The measured signal must of course be real, but Eq. B.3 is a complex function. The actual measured signal is the output of a double-balanced mixer with the photodiode signal and the modulation signal as inputs to the RF and LO ports, resp. The shape
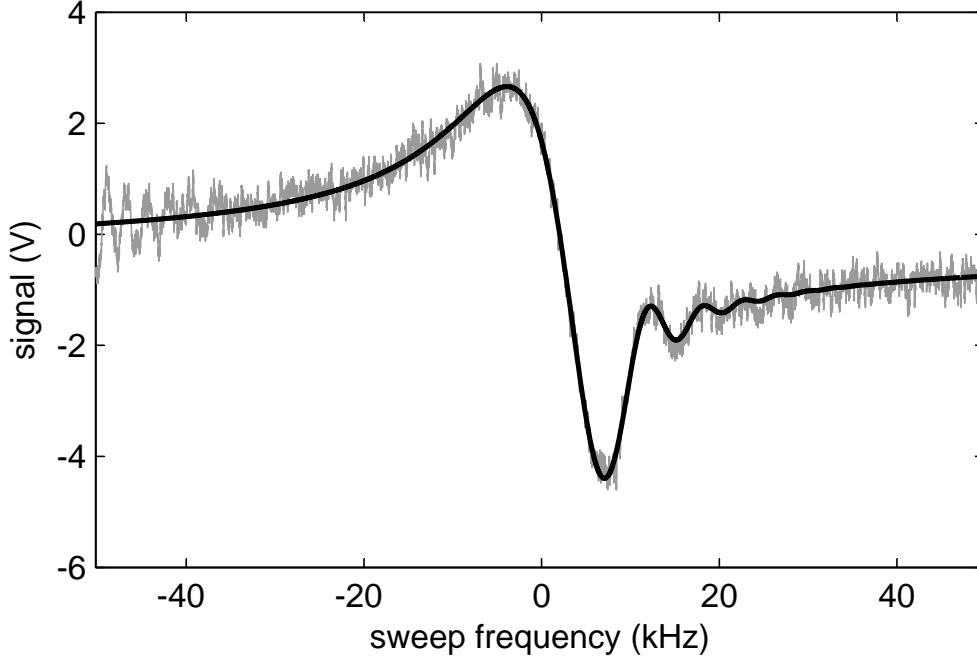
Figure B.2: Experimental dispersive trace (grey) for a laser frequency swept at a rate of 100 kHz/ms across the cavity resonance with a HWHM linewidth $\kappa = 4$ kHz. The black line is a fit using Eq. B.5. The oscillating behavior at the beginning of the sweep is a transient due to the sudden (step-function) turn-on of the probe light.

of this signal depends on the phase difference θ between these two inputs, and has the general form

$$S(t) = \Re\left[T(t)\right]\sin(\theta) + \Im\left[T(t)\right]\cos(\theta) \tag{B.5}$$

where $T(t)$ is defined in Eq. B.4. This model can fit the location of the zero-crossing of the data shown in Fig. B.2 with an statistical error bar of 12 Hz. The total optical power in the sideband is ~ 3.5 nW, which results in a total of $n_{\text{tot}} \approx 10^6$ photons entering the cavity during the sweep. The center of the cavity resonance, which has a linewidth of $2\kappa = 8$ kHz can then be expected to be found with an error of $\sim 2\kappa/\sqrt{n_{\text{tot}}} \approx 8$ Hz, close to the 12 Hz which we measured. This is true if the measurement is shot noise limited.

The actual experiment, however, requires a measurement of several lineshape centers with an accuracy that allows for sub-shot noise detection of the cavity resonance,

and hence the population difference. These traces can be separated in time by up to tens of milliseconds, so in addition to the ability to measure a single trace to sub-shot noise precision, the cavity resonance needs to be stable to within the desired precision over the timescale of the experimental protocol.

References

[1] C. M. Caves, "Quantum-mechanical noise in an interferometer," *Phys. Rev. D*, vol. 23, pp. 1693–1708, 1981.

[2] D. J. Wineland, J. J. Bollinger, W. M. Itano, F. L. Moore, and D. J. Heinzen, "Spin squeezing and reduced quantum noise in spectroscopy," *Phys. Rev. A*, vol. 46, pp. R6797–R6800, 1992.

[3] A. S. Sørensen and K. Mølmer, "Entangling atoms in bad cavities," *Phys. Rev. A*, vol. 66, no. 022314, 2002.

[4] A. Andre and M. Lukin, "Atom correlations and spin squeezing near the Heisenberg limit: Finite-size effect and decoherence," *Phys. Rev. A*, vol. 65, no. 053819, 2002.

[5] M. Saffman, D. Oblak, J. Appel, and E. S. Polzik, "Spin squeezing of atomic ensembles by multicolor quantum nondemolition measurements," *Phys. Rev. A*, vol. 79, no. 023831, 2009.

[6] A. Kuzmich, N. P. Bigelow, and L. Mandel, "Atomic quantum non–demolition measurements and squeezing," *Europhys. Lett.*, vol. 42, pp. 481–486, 1998.

[7] M. Kitagawa and M. Ueda, "Squeezed spin states," *Phys. Rev. A*, vol. 47, pp. 5138–5143, 1993.

[8] J. Hald, J. L. Sórensen, C. Schori, and E. S. Polzik, "Spin squeezed atoms: A macroscopic entangled ensemble created by light," *Phys. Rev. Lett.*, vol. 83, pp. 1319–1322, 1999.

[9] V. Meyer, M. A. Rowe, D. Kielpinski, C. A. Sackett, W. M. Itano, C. Monroe, and D. J. Wineland, "Experimental demonstration of entanglement-enhanced rotation angle estimation using trapped ions," *Phys. Rev. Lett.*, vol. 86, pp. 5870–5873, 2001.

[10] T. Fernholz, H. Krauter, K. Jensen, J. F. Sherson, A. S. Sørensen, and E. S. Polzik, "Spin squeezing of atomic ensembles via nuclear-electronic spin entanglement," *Phys. Rev. Lett.*, vol. 101, no. 073601, 2008.

[11] S. Chaudhury, G. A. Smith, K. Schulz, and P. S. Jessen, "Cavity QED with optically transported atoms," *Phys. Rev. Lett.*, vol. 96, no. 043001, 2006.

[12] D. Oblak, P. G. Petrov, C. L. G. Alzar, W. Tittel, A. K. Vershovski, J. K. Mikkelsen, J. L. Sørensen, and E. S. Polzik, "Quantum-noise-limited interferometric measurement of atomic noise: Towards spin squeezing on the Cs clock transition," *Phys. Rev. A*, vol. 71, no. 043807, 2005.

[13] A. Kuzmich, L. Mandel, and N. P. Bigelow, "Generation of spin squeezing via continuous quantum nondemolition measurement," *Phys. Rev. Lett.*, vol. 85, pp. 1594–1597, 2000.

[14] R. Thompson, G. Rempe, and H. J. Kimble, "Observation of normal-mode splitting for an atom in an optical cavity," *Phys. Rev. Lett.*, vol. 68, pp. 1132–1135, 1992.

[15] H. J. Kimble, *Cavity Quantum Electrodynamics, edited by P. Berman.* Academic Press, California, 1994.

[16] A. Boca, R. Miller, K. Birnbaum, A. Boozer, J. McKeever, and H. J. Kimble, "Observation of the vacuum Rabi spectrum for one trapped atom," *Phys. Rev. Lett.*, vol. 93, no. 233603, 2004.

[17] B. Julsgaard, A. Kozhekin, and E. S. Polzik, "Experimental long-lived entanglement of two macroscopic objects," *Nature*, vol. 413, pp. 400–403, 2001.

[18] D. I. Schuster, A. Wallraff, A. Blais, L. Frunzio, R.-S. Huang, J. Majer, S. M. Girvin, and R. J. Schoelkopf, "ac Stark shift and dephasing of a superconducting qubit strongly coupled to a cavity field," *Phys. Rev. Lett.*, vol. 94, no. 123602, 2005.

[19] C. Guerlin, J. Bernu, S. Deléglise, C. Sayrin, S. Gleyzes, S. Kuhr, M. Brune, J.-M. Raimond, and S. Haroche, "Progressive field-state collapse and quantum non-demolition photon counting," *Nature*, vol. 448, pp. 889–893, 2007.

[20] K. W. Murch, K. L. Moore, S. Gupta, and D. M. Stamper-Kurn, "Observation of quantum-measurement backaction with an ultracold atomic gas," *Nat. Phys.*, vol. 4, pp. 561–564, 2008.

[21] K. S. Choi, H. Deng, J. Laurat, and H. J. Kimble, "Mapping photonic entanglement into and out of a quantum memory," *Nature*, vol. 452, pp. 67–72, 2008.

[22] T. Chanelière, D. N. Matsukevich, S. D. Jenkins, S.-Y. Lan, T. A. B. Kennedy, and A. Kuzmich, "Storage and retrieval of single photons transmitted between remote quantum memories," *Nature*, vol. 438, pp. 833–836, 2005.

[23] J. F. Sherson, H. Krauter, R. K. Olsson, B. Julsgaard, K. Hammerer, I. Cirac, and E. S. Polzik, "Quantum teleportation between light and matter," *Nature*, vol. 443, pp. 557–560, 2006.

[24] J. Simon, H. Tanji, S. Ghosh, and V. Vuletić, "Single-photon bus connecting spin-wave quantum memories," *Nat. Phys.*, vol. 3, pp. 765–769, 2007.

[25] T. Pellizzari, S. A. Gardiner, J. I. Cirac, and P. Zoller, "Decoherence, continuous observation, and quantum computing: A cavity QED model," *Phys. Rev. Lett.*, vol. 75, pp. 3788–3791, 1995.

[26] L.-M. Duan and H. J. Kimble, "Scalable photonic quantum computation through cavity-assisted interactions," *Phys. Rev. Lett.*, vol. 92, no. 127902, 2004.

[27] A. T. Black, J. K. Thompson, and V. Vuletić, "On-demand superradiant conversion of atomic spin gratings into single photons with high efficiency," *Phys. Rev. Lett.*, vol. 95, no. 133601, 2005.

[28] M. G. Raizen, L. A. Orozco, M. Xiao, T. L. Boyd, and H. J. Kimble, "Squeezed-state generation by the normal modes of a coupled system," *Phys. Rev. Lett.*, vol. 59, pp. 198–201, 1987.

[29] L. A. Orozco, M. G. Raizen, M. Xiao, R. J. Brecha, and H. J. Kimble, "Squeezed-state generation in optical bistability," *J. Opt. Soc. Am. B*, vol. 4, pp. 1490–1550, 1987.

[30] G. S. Pati, M. Salit, K. Salit, and M. S. Shahriar, "Demonstration of a tunable-bandwidth white-light interferometer using anomalous dispersion in atomic vapor," *Phys. Rev. Lett.*, vol. 99, p. 133601, 2007.

[31] D. Meiser, J. Ye, D. R. Carlson, and M. J. Holland, "Prospects for a millihertz-linewidth laser," *Phys. Rev. Lett.*, vol. 102, no. 163601, 2009.

[32] D. Meiser and M. J. Holland, "Steady-state superradiance with alkaline-earth-metal atoms," *Phys. Rev. A*, vol. 81, no. 033847, 2010.

[33] P. Kumar and J. H. Shapiro, "Observation of Raman-shifted oscillation near the sodium *d* lines," *Opt. Lett.*, vol. 10, pp. 226–228, 1985.

[34] L. Hilico, C. Fabre, and E. Giacobino, "Operation of a cold-atom laser in a magneto-optical trap," *Europhys. Lett.*, vol. 18, pp. 685–688, 1992.

[35] W. Guerin, F. Michaud, and R. Kaiser, "Mechanisms for lasing with cold atoms as the gain medium," *Phys. Rev. Lett.*, vol. 101, p. 093002, 2008.

[36] S. Chu, L. Hollberg, J. E. Bjorkholm, A. Cable, and A. Ashkin, "Three–dimensional viscous confinement and cooling of atoms by resonance radiation pressure," *Phys. Rev. Lett.*, vol. 55, pp. 48–51, 1985.

[37] W. Demtröder, *Laser Spectroscopy.* Springer, third ed., 2003.

[38] R. W. P. Drever, J. L. Hall, F. V. Kowalski, J. Hough, G. M. Ford, A. J. Munley, and H. Ward, "Laser phase and frequency stabilization using an optical resonator," *Appl. Phys. B*, vol. 31, pp. 97–105, 1983.

[39] E. D. Black, "An introduction to Pound-Drever-Hall laser frequency stabilization," *Am. J. Phys.*, vol. 69, pp. 79–87, 2001.

[40] A. Schoof, J. Grünert, S. Ritter, and A. Hemmerich, "Reducing the linewidth of a diode laser below 30 hz by stabilization to a reference cavity with a finesse above 10^5," *Opt. Lett.*, vol. 26, pp. 1562–1564, 2001.

[41] R. W. Fox, C. W. Oates, and L. W. Hollberg, "Stabilizing diode lasers to high-finesse cavities," *Exp. Meth. Phys. Sci.*, vol. 40, pp. 1–46, 2002.

[42] D. J. Wineland, J. J. Bollinger, W. M. Itano, and D. J. Heinzen, "Squeezed atomic states and projection noise in spectroscopy," *Phys. Rev. A*, vol. 50, pp. 67–88, 1994.

[43] M. Tavis and F. W. Cummings, "Exact solution for an N–molecule-radiation–field hamiltonian," *Phys. Rev.*, vol. 170, pp. 379–384, 1968.

[44] G. S. Agarwal, "Vacuum–field Rabi splittings in microwave absorption by Rydberg atoms in a cavity," *Phys. Rev. Lett.*, vol. 53, p. 17321734, 1984.

[45] J. Brecha, L. Orozco, M. Raizen, and H. J. Kimble, "Observation of oscillatory energy exchange in a coupled–atom-cavity system," *J. Opt. Soc. Am. B*, vol. 12, pp. 2329–2339, 1995.

[46] R. J. Brecha, L. A. Orozco, M. G. Raizen, M. Xiao, and H. J. Kimble, "Mode splitting for two-level atoms inside an optical resonator," *J. Opt. Soc. Am. B*, vol. 3, p. P238, 1986.

[47] M. Raizen, R. Thompson, R. Brecha, H. J. Kimble, and H. J. Carmichael, "Normal–mode splitting and linewidth averaging for two–state atoms in an optical cavity," *Phys. Rev. Lett.*, vol. 63, pp. 240–243, 1989.

[48] Y. Zhu, D. J. Gauthier, S. E. Morin, Q. Wu, H. J. Carmichael, and T. W. Mossberg, "Vacuum Rabi splitting as a feature of linear–dispersion theory: Analysis and experimental observations," *Phys. Rev. Lett.*, vol. 64, pp. 2499–2502, 1990.

[49] F. Bernardot, P. Nussenzveig, M. Brune, J. Raimond, and S. Haroche, "Vacuum Rabi splitting observed on a microscopic atomic sample in a microwave cavity," *Europhys. Lett.*, vol. 17, pp. 33–38, 1992.

[50] Y. Yamamoto and A. Imamoglu, *Mesoscopic Quantum Optics*. John Wiley and Sons, 1999.

[51] J. Gripp, S. L. Mielke, L. A. Oroszco, and H. J. Carmichael, "Anharmonicity of the vacuum Rabi peaks in a many-atom system," *Phys. Rev. A*, vol. 54, pp. R3746–R3749, 1996.

[52] J. Klinner, M. Lindholdt, B. Nagorny, and A. Hemmerich, "Normal mode splitting and mechanical effects of an optical lattice in a ring cavity," *Phys. Rev. Lett.*, vol. 96, no. 023002, 2006.

[53] J. A. Sauer, K. M. Fortier, M. S. Chang, C. D. Hamley, and M. S. Chapman, "Cavity QED with optically transported atoms," *Phys. Rev. A*, vol. 69, no. 051804, 2004.

[54] D. W. Vernooy and H. J. Kimble, "Well-dressed states for wave-packet dynamics in cavity QED," *Phys. Rev. A*, vol. 56, pp. 4287–4295, 1997.

[55] S. Leslie, N. Shevni, K. R. Brown, D. M. Stamper-Kurn, and K. B. Whaley, "Transmission spectrum of an optical cavity containing N atoms," *Phys. Rev. A*, vol. 69, no. 043805, 2004.

[56] S. Bize, P. Laurent, M. Abgrall, H. Marion, I. Maksimovic, L. Cacciapuoti, J. Grünert, C. Vian, F. P. dos Santos, P. Rosenbusch, P. Lemonde, G. Santarelli, P. Wolf, A. Clairon, A. Luiten, M. Tobar, and C. Salomon, "Advances in atomic fountains," *C. R. Phys.*, vol. 5, pp. 829–843, 2004.

[57] A. E. B. Nielsen and K. Mølmer, "Atomic spin squeezing in an optical cavity," *Phys. Rev. A*, vol. 77, no. 063811, 2008.

[58] I. Bouchoule and K. Mølmer, "Preparation of spin–squeezed atomic states by optical–phase–shift measurement," *Phys. Rev. A*, vol. 66, no. 043811, 2002.

[59] A. Kuzmich and T. A. B. Kennedy, "Nonsymmetric entanglement of atomic ensembles," *Phys. Rev. Lett.*, vol. 92, no. 030407, 2004.

[60] J. P. Brantut, J. F. Clément, M. R. de Saint Vincent, G. Varoquaux, R. A. Nyman, A. Aspect, T. Bourdel, and P. Bouyer, "Light-shift tomography in an optical-dipole trap for neutral atoms," *Phys. Rev. A*, vol. 78, no. 031401, 2008.

[61] M. P. van Exter, S. J. M. Kuppens, and J. P. Woerdman, "Excess phase noise in self-heterodyne detection," *IEEE J. Quant. Electron.*, vol. 28, pp. 580–584, 1992.

[62] R. W. Boyd, *Nonlinear Optics.* Academic Press, 2003.

[63] A. K. Tuchman, R. Long, G. Vrijsen, J. Boudet, J. Lee, and M. A. Kasevich, "Normal-mode splitting with large collective cooperativity," *Phys. Rev. A*, vol. 74, no. 053821, 2006.

[64] I. Teper, G. Vrijsen, J. Lee, and M. A. Kasevich, "Backaction noise produced via cavity-aided nondemolition measurement of an atomic clock state," *Phys. Rev. A*, vol. 78, no. 051803, 2008.

[65] G. Vrijsen, O. Hosten, J. Lee, S. Bernon, and M. A. Kasevich, "Raman lasing with a cold atom gain medium in a high-finesse optical cavity," *Phys. Rev. Lett.*, vol. 107, no. 063904, 2011.

[66] W. W. Chow, J. Gea-Banacloche, L. M. Pedrotti, V. E. Sanders, W. Schleich, and M. O. Scully, "The ring laser gyro," *Rev. Mod. Phys.*, vol. 57, pp. 61–104, 1985.

[67] M. S. Shahriar, G. S. Pati, R. Tripathi, V. Gopal, M. Messall, and K. Salit, "Ultrahigh enhancement in absolute and relative rotation sensing using fast and slow light," *Phys. Rev. A*, vol. 75, p. 053807, 2007.

[68] R. Long, A. K. Tuchman, and M. A. Kasevich, "Multiple frequency modulation for low-light atom measurements in an optical cavity," *Opt. Lett.*, vol. 32, pp. 2502–2504, 2007.

[69] A. E. Lita, A. J. Miller, and S. W. Nam, "Counting near-infrared single-photons with 95% efficiency," *Opt. Express*, vol. 16, pp. 3032–3040, 2008.

[70] H. Ritsch, M. A. M. Marte, and P. Zoller, "Quantum noise reduction in Raman lasers," *Europhys. Lett.*, vol. 19, pp. 7–12, 1992.